NMR STUDY ON SILICON ANODE MATERIAL FOR LITHIUM-ION BATTERIES

MAGNETIC RESONANCE STUDIES OF SILICON ANODE MATERIALS AS A FUNCTION OF CYCLE NUMBER AND CURRENT DENSITIES

BY AMANDA A. CIEZKI, B.SC

A Thesis Submitted to the School of Graduate Studies in Partial Fulfilment of the
Requirements for the Degree Master of Science

McMaster University MASTER OF SCIENCE (2022) Hamilton, Ontario (Chemistry)

TITLE: Magnetic Resonance Studies of Silicon Anode Materials as a function of Cycle Number and Current Densities

AUTHOR: Amanda A. Ciezki, B.Sc. (The King's University)

SUPERVISOR: Professor Gillian R. Goward

NUMBER OF PAGES: xvi, 89

Lay Abstract

In recent years, the demand for alternative energy storage devices has grown. Specifically, lithium-ion batteries have become a technology of interest in the automotive industry. The widespread electrification of vehicles will reduce greenhouse gas emissions and thus promote a cleaner energy future. However, the primary challenges that hinder electric vehicles are a comparable driving range to that of a traditional fossil fuel-burning engine and fast-charging capabilities.

This work demonstrates how different cycling conditions affect the negative electrode (anode) of the battery with the use of nuclear magnetic resonance (NMR) techniques. Longevity studies were carried out with silicon as the negative electrode, and insights into different lithium silicide phases depending on the state of charge (SoC) and cycling count were discovered. This comprehensive work supports previously published results describing the capacity fade and breakdown mechanisms of silicon and is the first to acquire NMR spectra at advanced cycle counts. In addition, more crystalline lithium silicides are formed at faster charging rates, and the presence of lithium metal is detected, which can be detrimental to the battery's health. The behaviour of lithium chemical environments within the silicon anode material is quantified, providing an in-depth interpretation of the result. The performance of silicon under different conditions, like those seen in an electric vehicle, ultimately indicates how different current rates affect the material and leads to the classification of different chemical environments within the material of interest.

Abstract

This research aims to explore material questions within the field of lithium-ion batteries (LIBs) used for electric vehicles (EVs) through nuclear magnetic resonance (NMR). In EVs, the driving range and fast-charging capabilities need improvement. A promising anode material, silicon, was investigated using both ex situ and operando NMR techniques. *Ex situ* ^{7}Li NMR was used to identify key lithium silicide phases in the material at various states of charge (SoC). The different phases highlighted throughout this report represent the degree of lithiation per silicon atom. The longevity of the silicon material was tested as a function of cycle count, which provided insight into how the different local environments in silicon were affected. Based on the *ex situ* ^{7}Li NMR results, mechanisms for capacity fade and degradation were proposed.

Operando NMR allowed for the silicon material to be monitored simultaneously with the electrochemical charging cycle. Real-time information regarding structural changes of the Li_xSi phase under multiple different cycling conditions was achieved and analysed based on deconvolutions and integration. The slower charging rate (C-rate) of C/3 using *operando* NMR further confirms the formation of phase 1 (Li_xSi, $x < 2.0$) and phase 2 (Li_xSi, $2.0 < x < 3.5$) seen via *ex situ* NMR. More detail was provided with this technique than an *ex situ* spectrum collected at the top of charge (TOC) and bottom of discharge (BOD) of the post-mortem battery. When the current density of the battery was increased, drastic differences were seen regarding the formation of lithium silicide phases in comparison to slower c-rates. With the faster C-rates, lithium metal was formed during the NMR experiment, and the formation of phase 3, a more highly lithiated crystallin phase, not present under *ex situ* conditions, was identified. This one-of-a-kind methodology allowed us to probe the lithium environments in the silicon anode material and gain insight into fundamental chemical changes that occur during battery operation.

Acknowledgements

To start, I want to thank my supervisor Dr. Gillian Goward for her support, guidance, and patients as I found my footing in the group. As a person, you are among the most compassionate and kind-hearted I know, and I will never forget all the support you provided throughout my time in the group.

In addition, I would like to express my thanks to my other committee member Dr. Drew Higgins for your support throughout my master's. Thank you for all the helpful advice during our committee meetings.

To the past and present Goward Group members, for your support in and outside the lab. You have seen it all and helped me through some of my most challenging and frustrating days in the lab. Thank you for lending a listening ear, the meaningful conversations, and of course all the laughter and smiles.

Thank you to Dr. Zoya Sadighi and Dr. Kevin Sanders for being my mentors.

I would also like to thank my family for their continual and unwavering support. I know I took you by surprise moving across the country, but you never missed a beat, and even from 3,400 km away I feel your love and support every day. Thank you, I am truly blessed to have my parents and brother in my life.

Thank you to my professors from The King's University, who always pushed me to do more, and the friends from undergrad that supported me through my graduate studies.

Finally, I would like to thank the community and sport I fell in love with. I can confidently say I would not be the same person I am today without rowing, and the amazing individuals I have come to call my friends. Thank you to the coaches that pushed me to become a better athlete, and my teammates for always making my mornings the best part of my day, regardless of how exhausted we were from a workout. Your conversations, jokes, and words of advice were always exactly what I needed. You helped me through this master's more than you know.

Table of Contents

List of Figures

List of Tables

List of Abbreviations and Symbols

$\vec{B}_0$	Applied field
B_0	magnetic field strength of the applied field aligned with the z-axis
ΔE	separation between the ground energy level
BMS	Bulk magnetic susceptibility
BOD	Bottom of Discharge
C-rate	Charging rate
DMC	Dimethyl carbonate
dOp	Derivative operando
EC	Ethylene carbonate
E_m	energy levels
EMC	Ethyl methyl carbonate
EPDM	Ethylene propylene diene monomer rubber
EV	Electric Vehicle
EXSY	Exchange spectroscopy
FEC	Fluoro ethylene carbonate
FID	Free induction decay
$\hbar$	reduced Planck constant
LCO	Lithium cobalt oxide

LFP	Lithium iron phosphate
LIB	Lithium Ion Battery
$LiPF_6$	Lithium hexafluorophosphate
MAS	Magic angle spinning
NCA	Nickel cobalt aluminum oxide
NMC	Nickel manganese cobalt oxide
NMR	Nuclear magnetic resonance
OCV	Open Circuit Voltage
PEEK	Polyetheretherketone
$\hat{S}$	Spin angular momentum
SEI	Solid−electrolyte interphase
SoC	States-of-charge
ss	Solid State
TOC	Top of Charge
VC	Vinylene carbonate
α	Alpha
β	Beta
ω_0 / ν_0	Larmor precession

Declaration of Academic Achievement

Kevin J. Sanders designed the operand cartridge cell in Chapter 4 and helped in the NMR measurements preformed in Chapter 3 and 4. Nafiseh Zaker collected the scanning electron microscopy images of the silicon anode, seen in chapter 3. Breanna Pinto helped in the assembly of the cartridge cells that *operando* NMR data was collected from. Brian Koch collected the three-electrode experiment on the Si/NMC cell at the Research and development center for General Motors. Ion Halalay from General Motors, contributed to data interpretation. Both *Ex situ* ^{7}Li NMR and *operando* ^{7}Li NMR data for chapter 3 and 4 were collected by Amanda A. Ciezki. All other experimental work was completed by Amanda A. Ciezki.

Chapter 1

Introduction

1.1 Motivation

Lithium-ion batteries (LIBs) first commercialized in the early 1990s, have by now captured the portable electronics (smart phones, tablets, laptops, etc.) and portable tools markets due to their high energy density [1,2] and have become the most viable energy supply for electrified vehicles (EVs). Replacing the conventional combustion-engine-powered vehicles with EVs dependent on LIBs could reduce greenhouse gas emissions and environmental pollution.[3,4] Funding and subsidies by many governments in Europe as well as USA and China, are used to bring new EV battery technologies to market readiness, promote EV sales and the installation of charging stations in parking areas.[5] In the Netherlands gasoline and diesel car sales will be banned by 2030, with the UK to follow in 2040.[6] With the environmental and economic benefits the demand for EVs has grown, and the number of passenger EVs sold in 2018 increased to 5.1 million.[7]

However, to compete with conventional internal combustion engine (ICE) powered vehicles, enable the widespread transition of road transportation to electrified vehicles and gain broad acceptance in the marketplace, serval challenges must still be overcome. Larger, cheaper batteries with increased energy density are critical to meet consumer needs. Specifically, the significantly longer charging times of EVs compared with re-fueling the gas tank of ICE powered automobiles is a barrier for market acceptance of electrified vehicles. To overcome this critical challenge and be competitive in the automobile industry, EVs require comparable charging times to those for the fill-up of an ICE powered vehicle (10-15 min).[8] Fundamental research is required for all components in LIB's for EVs to provide a comparable driving experience to gasoline and diesel cars. To achieve this goal, material choices for LIBs need to be optimized. In particular, active materials (for both anodes and cathodes) that enable batteries with both high energy density and high specific energy are desirable, to allow packing more batteries in a given volume and minimize battery mass, respectively.

Intercalation oxides like lithium cobalt oxide (LCO), nickel cobalt aluminum oxide (NCA), nickel manganese cobalt oxide (NMC), and lithium iron phosphate (LFP) are at present the cathode materials used in commercial LIBs.[9,10] These materials present various advantages and disadvantages for battery abuse tolerance and cost. LCO is the prevalent cathode material in batteries for portable electronic devices, as it enables a higher cell energy than any other cathode material from the oxide class, but has a relatively low specific capacity (140 $\mathrm{mAh \cdot g^{-1}}$), as well as the highest cost. NMC and NCA enable higher specific capacity, in the 160 – 200 $\mathrm{mA\ h\ g^{-1}}$ range. However, they present reasons for concerns due to the high cost of Ni and especially Co, as well as abuse tolerance, due to their thermal properties. LFP is also another commercial cathode material with a theoretical specific capacity of 170 $\mathrm{mA\ h\ g^{-1}}$ and very good thermal stability due to its olivine structure, but its lower operating voltage leads to a lower vehicle range at equal battery pack mass.[9] Minimizing the amount of nickel and particularly cobalt used in cathode active materials is imperiously necessary for reducing the cost of automotive LIBs, as the cathode active material represents the highest price item on the bill of materials of automotive Li-ion batteries .

Graphite was first suggested as an anode material in the early 1970's and is still used today due to its low cost, abundant availability, high lithium diffusivity, and small volume change during lithiation/delithiation.[3,9] However, lithium metal is known to plate on the surface of the anode during fast charging when lithium cannot intercalate into the material at a faster rate than the current. Silicon materials are being considered for increasing the overall energy density of Li-ion batteries. But like any new material, silicon as anode material in LIBs also has obstacles to overcome. It follows a different lithiation mechanism than graphite, which allows for a higher degree of lithiation but also suffers from large (up to 300%) volume changes during charge-discharge cycling (i.e., lithium uptake and release), causing problems with material stability and battery longevity.

Various challenges are present to fully optimize LIBs for commercial EVs, ranging from material development and characterization to cell engineering and optimization. The aim of the work presented herein is to expand on the silicon anode body of research by using various nuclear magnetic resonance (NMR) techniques to investigate the problems and challenges posed by the use of silicon anode materials in Li-ion batteries. *Ex situ* ^{7}Li NMR is used to identify phase changes and local environment changes within the Si material during long-term electrochemical cycling in a battery cell. This allows for analyses on the longevity of the material and the identification of changes in the silicon chemistry as a function of degradation via chemical shift. By comparing NMR spectra of the material harvested after varying numbers of charge-discharge cycles, small changes in the local structure and phases can be identified and characterized. The *ex situ* NMR data were collected on cycled Si electrodes after cell disassembly in either a fully charged or fully discharged state. To further investigate how the material changes during repeated cycling, *operando* NMR was performed with a cartridge cell of novel design. The NMR spectra were collected while concomitant with the cycling of the battery, allowing for changes in the chemical and structural properties to be monitored under cell working conditions. With this technique intermediate phases can be obtained. Studying silicon and its chemical behavior over different electrochemical conditions will allow for an in depth understanding of the ways in which pure silicon anodes age prematurely. With this knowledge material and electrochemical optimizations can be developed and carried out, to design better LIBs for the EV applications.

1.2 Lithium-Ion Batteries

The active components of a battery cell comprise two electrodes, the anode (negative electrode), and the cathode (positive electrode), a microporous separator membrane placed between the electrodes and an electrolyte solution that fills the pores in the separator and electrodes. The separated electrolyte solution is a liquid or a solid. In LIBs the electrolyte solution conducts the lithium ions between the anode and cathode, while the electrons involved in the redox reactions at the electrodes travel through an external circuit.[10] During battery cell charging, a current is applied by a charging device, that causes the lithium ions to move from the cathode to the anode and changes their chemical potentials (a.k.a. Fermi levels). The difference between the chemical potential of the cathode and anode represents the cell voltage. During cell discharging, the battery cell delivers a current to an external device (a.k.a. electrical load), which has a direction opposite that from the cell charging, while the cell voltage decreases. (Note: Since the anode and cathodes in a practical battery cell are made of dissimilar materials, the voltage of a discharged cell cannot be zero, but is always some positive number.) Figure 1.1 shows the setup of a typical LIB connected to light bulb as external load. In order to enable repeated charging and discharging of a battery, all the redox reactions occurring at both electrodes must be reversible. How much a cell is charged/discharged (a.k.a. the utilized capacity of a cell), depends on the cell capacity at a given current density. The utilized cell capacity depends on the current as the transfer rate of ions across the electrode/electrolyte can become diffusion limited at high current densities.[11] This results in an apparent (reversible) capacity loss, as lithium ions cannot insert themselves into the electrode at the same rate. Since the components of the electrolyte solution are thermodynamically unstable in contact with the electrochemically active materials in the electrodes, passivating layers, known as solid electrolyte interphase (SEI) or cathode electrolyte interphase (CEI) must be formed, respectively at the anode and the cathode, during the first few electrochemical cycles of a cell's life, to minimize parasitic reactions during subsequent battery use and enable good battery performance (good capacity retention over many charging-discharging cycles, minimal self-discharging, etc.).

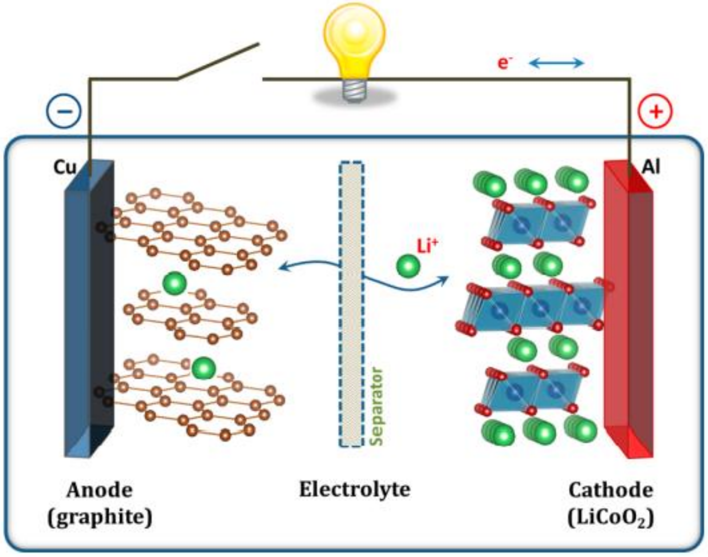

Figure 1.1 Schematic illustration of the first Li-ion battery ($LiCoO_2$/Li^+ electrolyte/graphite). Reprinted with permission form J. Am. Chem. Society, 2013, ***135****, 1167 – 1176*[10]*. Copyright © 2013, American Chemical Society.*

Lithium is a monovalent ion, which is the minimal charge an ion can have. However, its diffusion rate is significantly than that of multivalent ions or other alkali ions, due to its small ionic radius and significantly smaller mass (e.g., >3x smaller than Na^+ or Mg^{2+}, >6x smaller than K^+ or Ca^{2+}). Lithium is also advantageous because of its low reduction potential, which is lowest among all metals, enables LIBs with high voltages. These factors enable LIBs to with high gravimetric and volumetric energy, and power density,[9] i.e., battery characteristics that are critical for their implementation in the EV industry.

The traditional anode material, graphite, has a theoretical capacity of 372 mA h g^{-1} corresponding to its highest lithiated state of graphite, LiC_6.[12] This is low compared to other anode materials, but due to its modest cost and outstanding cycling stability, it is the preferred anode material for LIBs. Other anode materials like silicon are being explored as a possible replacement for graphite. Silicon exhibits much higher practically achievable capacity (3,572 mAh g^{-1}) than graphite.[13] Silicon undergoes an alloying mechanism with lithium and can therefore incorporate a larger amount of lithium atoms per silicon atom. Details regarding anode materials in LIBs are provided in Section 1.3.

Commercial cathode materials for LIBs include transition metal oxides like lithium cobalt oxide (LCO), nickel cobalt aluminium oxide (NCA), nickel manganese cobalt oxide (NMC), and lithium iron phosphate (LFP). For small hand-held devices like smartphones and laptops, LCO is almost exclusively used, as it enables a higher energy density in Li-ion batteries than any other cathode material. NMC in contrast, can be cycled to greater voltages and has gained popularity over the years because of its high experimental capacity compared to other cathode materials.[14] Many review articles in literature highlight the developments and ongoing research for cathode materials.[3,9,10,14,15] The work in this thesis focuses on the anode materials of LIBs.

The third main component in a LIB is the electrolyte solution. The electrolyte solution has two main roles: (1) it is a transport medium for lithium-ions between the anode and cathode via a lithium salt and main solvents mixture; and (2) it creates protective films at the anode and cathode surfaces, through the decomposition of additives and some of the main solvents. The electrolyte solution needs both adequate diffusion and ionic conduction properties. In addition, low or no toxicity, no flammability, as well as solution components that are stable against reduction at the anode and oxidation at the cathode are other desirable properties of electrolyte solutions. Lithium hexafluorophosphate ($LiPF_6$) dissolved in mixtures of carbonate solvents such as ethylene carbonate (EC), ethyl methyl carbonate (EMC), and dimethyl carbonate (DMC), are standard liquid electrolyte solutions for LIBs. Despite its draw back of hydrolysis with HF generation, $LiPF_6$ is used in LIB electrolyte solutions because it forms a passivating AlF_3 film on the aluminum current collector for the cathode, is soluble in many solvents and forms solutions with relatively high ionic conductivity. The main electrolyte solution components (anions and main solvent molecules) are not thermodynamically stable against reduction at the anode and oxidation at the cathode. The passivating films are formed on the electrode surfaces during the first one to three, so-called "formation" cycles, through the decomposition of various sacrificial compounds chosen for their ability to decompose at the anode and cathode before the reduction and oxidation potentials of main solution components are reached, respectively. The surface film formed at the anode is called solid electrolyte interface (SEI), while the surface film formed at the cathode is called cathode electrolyte interface (CEI). The main inorganic components of the SEI are lithium carbonate, oxide and fluorides varying depended on the electrolyte solution makeup. In addition, a host of organic and polymeric reaction products are also part of the SEI. The SEI layer is vital for achieving cycling stability in LIBs and is therefore a major field of inverstigation in the battery community.[16] Various electrolyte additives, like fluoro(ethylene carbonate) (FEC) and vinylene carbonate (VC), modify and enhance the SEI stability.[17] This is of great importance when it comes to optimizing the SEI for other anode materials like silicon.

As seen from the brief overview of LIBs, many different factors influence the battery components. Cell design, scale-up and manufacturing are some of the numerous research areas not discussed here that are nevertheless essential for the commercial success of LIBs. As such, research in all fields related to LIBs should be pursued to optimize batteries that can be used in EVs and other energy storage applications.

1.3 Anode Materials

Historically graphite has been the material of choice for the negative electrode and is the main anode material still used for commercial Li-ion batteries today. Although the material of interest in this thesis is silicon, it is important to compare and highlight some of the differences between these anode materials. Graphite undergoes lithiation via an intercalation mechanism, to LiC_6 where Li ions reside within spaces in the between the sheets of graphene that comprise the graphite lattice. During lithiation the maximum volume expansion is small (~ 13%), which accounts for its stability and mitigates cracking of the electrode surface during charge and discharge.[18] This mechanism can sustain remarkable capacity retention over many cycles, but the number of intercalation sites for Li ions within the host lattice is low, since the intercalation reaction occurs preferentially at the edge planes of the graphite particles, as opposed to basal planes that form most of the area of the flake-like graphite particles.[19] At low currents (or C-rates) the intercalation mechanism has proven to be sufficient, however under fast-charging conditions, lithium can plate onto the surface instead of diffusion into the material. The inverse of the C-rate applied to a battery indicates in how many hours the battery is being charged or discharged. At high enough currents, lithium ions will accumulate on the surface of the anode instead of intercalating into the material. This leads to lithium plating when the current through the electrolyte solution exceeds the rate of lithium diffusion into graphite. Figure 1.2 shows a schematic of how lithium intercalates or plates on the graphite anode relative to C-rate.[20] At low to moderate current the lithium is either intercalated or deintercalated into the graphite upon charge and discharge i) and ii). At high c-rates lithium is plated iv), and only partially reversible on discharge iii). During the OCV, when no current is applied some of the lithium can also diffuse into the graphite v). The irreversibly plated lithium can cause major technical risks, such as increased cell resistance, electrolyte degradation and loss of lithium inventory resulting in capacity degradation.[8,21] Consequently, because of graphite's intercalation mechanism, relatively low specific capacity, and lack of performance during fast charging other materials with increased capacity and better fast charging capabilities are of greater interest for LIBs.

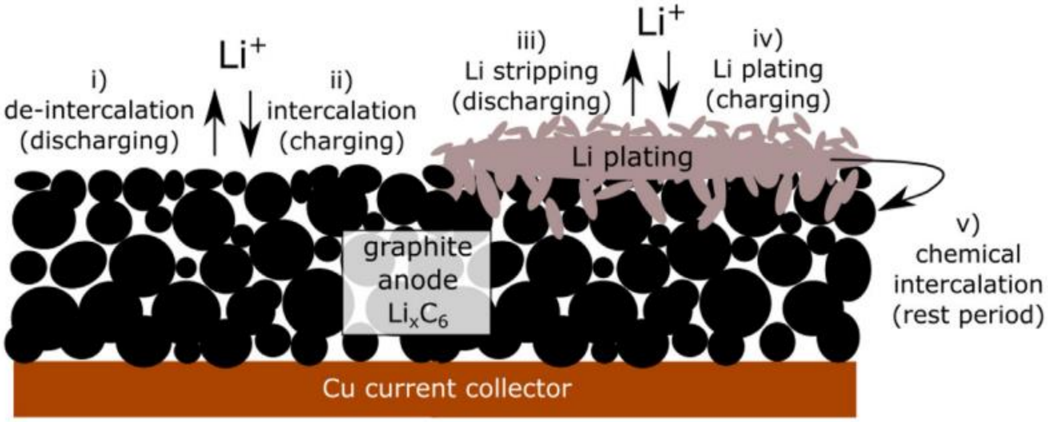

Figure 1.2: Illustration of different mechanisms during charging of graphite anodes (i) Li de-intercalation from lithiated graphite (ii) Li intercalation into graphite during charging (iii) removal of plated lithium during discharge (iv) Li plating during charge at high currents (v) Diffusion of lithium into the graphite network during a rest period. Reprinted with permission from Electrochimica Acta, 2017,230, 454 - 460[20]*. Copyright © 2017, Elsevier.*

Silicon is a material of interest because of its extremely high gravimetric (3572 mA h g^{-1}) and volumetric (8322 mA h cm^{-3}) capacities, ten times that of graphite.[22] Its increased energy density makes it an ideal material for LIBs, especially when considering its vast improvements compared to graphite. Unlike graphite, silicon follows an alloying mechanism which involves the breaking and reformation of bonds in the host structure instead of a reversible insertion of lithium via the intercalation process. Silicon forms alloys with lithium during electrochemical cycling that cause the host structure to change and expanse which results in the high volumetric and gravimetric capacities.[23,24] , This volume expansion turns out to be a major draw back of silicon anode materials as the dramatic change, up to 300% upon lithiation, causes the electrode to lose its structural integrity.[23,25]

During cycling a phase change in the silicon material from crystalline to amorphous occurs when the most (electrochemically) lithiated state ($Li_{15}Si_4$) is reached at the top of charge (TOC), by a two-phase reaction seen in equation 1.1 and 1.2. [1] $Li_{15}Si_4$ has a theoretical capacity of 3.75 lithium per one silicon atom and unfortunately is known to cause significant capacity fade over multiple cycles.[26] The first equation represents the initial lithiation and the 2nd redox reaction on subsequent charges. The reverse is also true during discharge. The $Li_{15}Si_4$ crystalline phase is converted into an amorphous lithium silicide (a-Li_xSi) as the electrons and lithium atom migrate toward the cathode, thus decreasing the lithium content in the silicon material.

$$\text{Si (crystalline)} + x\text{Li}^+ + x\text{e}^- \rightarrow \text{Li}_x\text{Si (amorphous)} \qquad \text{Eq. 1.1}$$

$$4\ \text{Li}_x\text{Si (amorphous)} + 4\ (3.75-x)\text{Li}^+ + 4\ (3.75-x)\text{e}^- \rightarrow \text{Li}_{15}\text{Si}_4\ \text{(crystalline)} \qquad \text{Eq. 1.2}$$

During the alloying mechanism many different Li_xSi phases can form. Figure 1.3, highlights $Li_{12}Si_7$, Li_7Si_3, $Li_{13}Si_4$, $Li_{15}Si_4$ and $Li_{21}Si_5$ as different crystalline lithium silicide phases. Interestingly the $Li_{15}Si_4$ phase is the most electrochemically lithiated phase that can be produced, limiting the practically achievable capacity to 3,578 $mAh \cdot g^{-1}$, which corresponds to 3.75 lithium per silicon. The amorphous silicide phases formed electrochemically have been group into three distinct phases previously published in literature.[1,25] These distinctions are relevant to this research as they also help identify the different Li_xSi phases seen in nuclear magnetic resonance (NMR), which will become apparent in the following chapter. At lower states-of-charge (SoC)/lithiation, silicon is known to be more amorphous containing both chains and clustered silicon atoms (phase 1), the completely crystalline environment is no longer present. As silicon is continually lithiated the clusters are broken down into smaller units consisting of two dimers or more connected silicon atoms, Li_2Si. This is ascribed to phase 2. At the top of charge (TOC) or when the silicon is fully lithiated ($Li_{15}Si_4$) is described as phase 3, where all the silicon cluster are broken, and only isolated silicon and lithium atoms are present. The phase 3, 15:4 ratio of Li:Si causes huge stress on the Si particles resulting in cracking at the surface to accommodate for the increased lithium. Li ions are irreversibly consumed because the newly exposed surfaces are not coated with the passivating solid-electrolyte interphase (SEI) layer and react with the electrolyte. As the LIB is charged and discharged the continual volume expansion/contraction leads to thickening of the SEI layer, and electrically disconnected Si particles, contributes to capacity fade.[1,27] This breakdown disrupts the conductive network and has negative effects on the SEI.

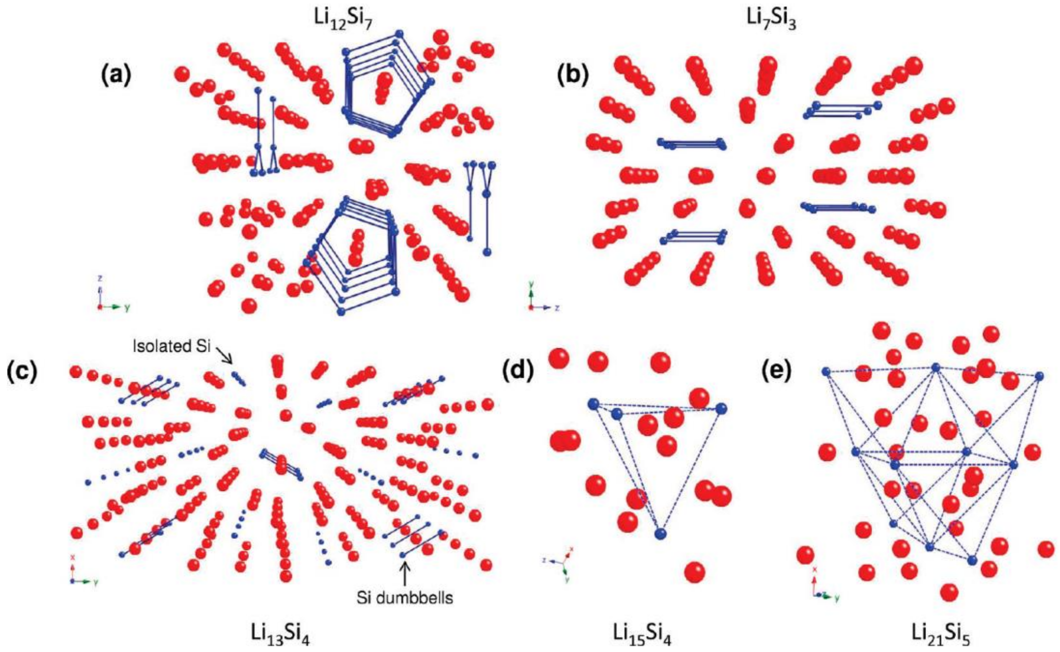

Figure 1.3: Structural representation of the different Li_xSi crystallographic sites. Lithium and silicon atoms are shown in red and blue respectively. The blue lines indicate Si – Si bonds while the blue dashed lines inidicate the closest Si – Si distances > 3.0 Å. Reprinted with permission from The Journal of the American Chemical Society, 2009, ***131****, 26, 9239-9249*[25]*. Copyright © 2009, American Chemical Society.*

1.4 The Challenges with Silicon

Although silicon is a promising anode material, challenges different than that of graphite are present. Three main challenges leading to significant capacity fade or cell death are summarized in Figure 1.4. With numerous repeated cycles pulverization of active material can occur, as seen in Figure 1.4 a), causing capacity fade. The large volume expansion/contraction during lithiation/delithiation puts a substantial amount of stress on the silicon particles. This causes the material to crack and pulverize. The morphology and volume changes depicted in Figure 1.4 b) is also challenging. During lithiation silicon particles expand and encroach on each other, and after delithiation they contract which can result in detachment from the current collector. Again, capacity fade can occur with this change in morphology and separation of silicon particles from the current collector and electrochemical matrix.[27] Finally, the formation of a stable solid electrolyte interface (SEI) is challenging because of the subsequent volume change during lithiation and delithiation, Figure 1.4 c). Unlike graphite where the SEI layer is stable and essential for a working battery, silicon SEI has a more dynamic process. It is constantly reforming during cycling. The volume expansion exposes active material which further reacts with the electrolyte, creating more SEI. Particles become electrically isolate from the conductive carbon matrix. While the binder within the anode can provide adhesion to the conductive matrix, it cannot prevent the accumulation of SEI products over numerous cycles. The continues reformation and growth leads to significant capacity losses during the formations cycles and continues as more lithium ions are consumed every cycle.[21,23] Several studies have explained ways to mitigate the significant volume expansion primarily seen with the $Li_{15}Si_4$ phase formed at the TOC. Using SEM a study found that silicon clusters were only weakly bounded to the substrate by small points of contact after repeated cycling and formation of significant $Li_{15}Si_4$.[26] Changing the electrochemical cycling parameters to limit the voltage window (to avoid the formation of $Li_{15}Si_4$ phase)[26], adding nano-sized silicon particles[27,28], and optimizing different binder materials/electrolyte additives[29,30] are all areas of study for the optimization of silicon anodes.

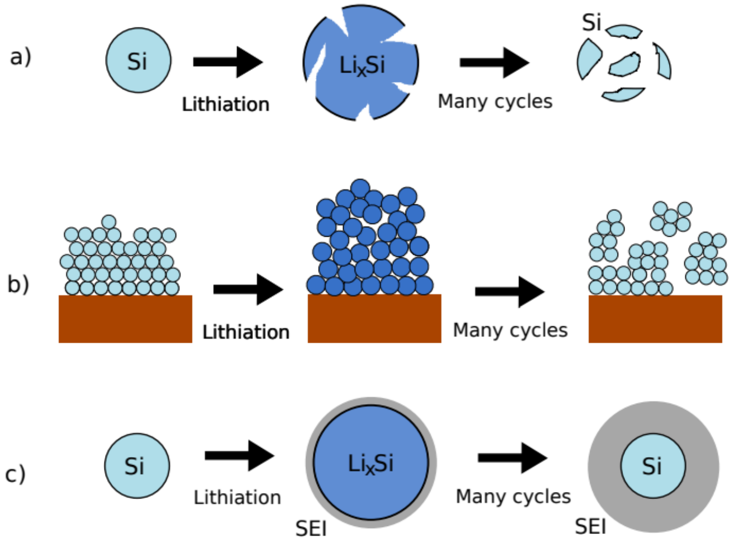

Figure 1.4: Challenges related to large volume changes of silicon as electrode material; (a) material decrepitation, (b) morphology and volume changes of the whole electrode, (c) unstable solid electrolyte interphase. Illustration reprinted from Nysted, V. S. The Galvanostatic Intermittent Titration Technique for Silicon-Based Li-Ion Battery Anodes: Theory and Experimental Validation.[31]

1.5 Thesis outline

Many studies have previously examined mechanisms leading to capacity failure in silicon material as an anode.[23,26,27] In conjunction, various studies using ^{7}Li ssNMR have study pure silicon electrode material and its different electrochemical lithiated species.[1,22,25,30,32,33] Each study looks at silicon material using either *ex-situ* or *in situ* ^{7}Li ssNMR, however no study to date examine a full battery with *operando* NMR using a parallel-plate resonator RF probe, previously used in Sanders et al..[34] This work aims to add to the ^{7}Li ssNMR work of the pure silicon electrode material by investigating the material with *ex situ* NMR and *operando* NMR with the use of a novel exchangeable cartridge-like battery container that mimics the layout of a single-layer pouch seen in EVs. Unlike previous work that can only look at the material of interest post-mortem, *operando* measurements are performed during electrochemical cycling. Both *in situ* and *operando* measurements provide insight into fundamental chemical and structural properties which can go undetected in *ex situ* characterization approaches.[35] However, *operando* NMR is the 'gold standard' as it provides real time analysis. Here we showcase the utility of the *operando* NMR methodology for tracking lithium silicide phases present in our material of interest as the battery is cycled. In addition, *ex situ* ssNMR was used to identify different Li_xSi phases and provide further insight into the local Li and Si environments previously published by Grey et al..[1]

Chapter 2 provides an overview of the ex-situ and *operando* NMR used to collect the result seen in chapter 3 and 4.

In Chapter 3, using a C-rate of C/3 the longevity behaviour of cells with a silicon anode and $LiNi_{0.6}Mn_{0.2}Co_{0.2}O_2$ (NMC622) cathode were examined to better understand how local environments in the Si material change with different cycle lengths. The exchange between phase 1 & 2 Li_xSi was also explained using EXSY NMR experiments.

Chapter 4 introduces the novel parallel-plate RF probe and single-layer pouch cell designed by Sanders et al.[34] Similar electrochemical parameters for the *operando* study to that of the results presented in Chapter 3 were used. Fast charging constraints were also tested to see how the LixSi phases change with C-rate and if lithium plating occurs.

Lastly, Chapter 5 gives a summary of the work and outlook.

1.6 References

(1) Kitada, K.; Pecher, O.; Magusin, P. C. M. M.; Groh, M. F.; Weatherup, R. S.; Grey, C. P. Unraveling the Reaction Mechanisms of SiO Anodes for Li-Ion Batteries by Combining in Situ 7Li and Ex Situ 7Li/29Si Solid-State NMR Spectroscopy. *J Am Chem Soc* **2019**, *141* (17), 7014–7027. https://doi.org/10.1021/jacs.9b01589.

(2) Winter, M.; Barnett, B.; Xu, K. Before Li Ion Batteries. *Chemical Reviews*. American Chemical Society December 12, 2018, pp 11433–11456. https://doi.org/10.1021/acs.chemrev.8b00422.

(3) Li, M.; Lu, J.; Chen, Z.; Amine, K. 30 Years of Lithium-Ion Batteries. *Advanced Materials*. Wiley-VCH Verlag August 16, 2018. https://doi.org/10.1002/adma.201800561.

(4) Dunn, B.; Kamath, H.; Tarascon, J.-M. *Electrical Energy Storage for the Grid: A Battery of Choices System Power Ratings, Module Size*. http://science.sciencemag.org/.

(5) Lin, J.; Liu, X.; Li, S.; Zhang, C.; Yang, S. A Review on Recent Progress, Challenges and Perspective of Battery Thermal Management System. *International Journal of Heat and Mass Transfer*. Elsevier Ltd March 1, 2021. https://doi.org/10.1016/j.ijheatmasstransfer.2020.120834.

(6) Javon Johnson. *The Netherlands Will Ban Petrol and Diesel Cars By 2030*. wide open media.

(7) Balali, Y.; Stegen, S. Review of Energy Storage Systems for Vehicles Based on Technology, Environmental Impacts, and Costs. *Renewable and Sustainable Energy Reviews*. Elsevier Ltd January 1, 2021. https://doi.org/10.1016/j.rser.2020.110185.

(8) Krachkovskiy, S. A.; Raza, M.; Aguilera, A. R.; Halalay, I. C.; Balcom, B. J.; Goward, G. Real-Time Quantitative Detection of Lithium Plating by In Situ NMR Using a Parallel-Plate Resonator. *J Electrochem Soc* **2020**. https://doi.org/10.1149/1945-7111/abb7ea.

(9) Nitta, N.; Wu, F.; Lee, J. T.; Yushin, G. Li-Ion Battery Materials: Present and Future. *Materials Today*. Elsevier B.V. June 1, 2015, pp 252–264. https://doi.org/10.1016/j.mattod.2014.10.040.

(10) Goodenough, J. B.; Park, K. S. The Li-Ion Rechargeable Battery: A Perspective. *Journal of the American Chemical Society*. January 30, 2013, pp 1167–1176. https://doi.org/10.1021/ja3091438.

(11) Talaie, E.; Bonnick, P.; Sun, X.; Pang, Q.; Liang, X.; Nazar, L. F. Methods and Protocols for Electrochemical Energy Storage Materials Research. *Chemistry of Materials*. American Chemical Society January 10, 2017, pp 90–105. https://doi.org/10.1021/acs.chemmater.6b02726.

(12) Krachkovskiy, S. A.; Reza, M.; Aguilera, A. R.; Halalay, I. C.; Balcom, B. J.; Goward, G. R. Real-Time Quantitative Detection of Lithium Plating by In Situ NMR Using a Parallel-Plate Resonator. *J Electrochem Soc* **2020**, *167* (13), 130514. https://doi.org/10.1149/1945-7111/abb7ea.

(13) Kim, N.; Chae, S.; Ma, J.; Ko, M.; Cho, J. Fast-Charging High-Energy Lithium-Ion Batteries via Implantation of Amorphous Silicon Nanolayer in Edge-Plane Activated Graphite Anodes. *Nat Commun* **2017**, *8* (1). https://doi.org/10.1038/s41467-017-00973-y.

(14) Daniel, C.; Mohanty, D.; Li, J.; Wood, D. L. Cathode Materials Review. In *AIP Conference Proceedings*; American Institute of Physics Inc., 2014; Vol. 1597, pp 26–43. https://doi.org/10.1063/1.4878478.

(15) Shi, J. L.; Xiao, D. D.; Ge, M.; Yu, X.; Chu, Y.; Huang, X.; Zhang, X. D.; Yin, Y. X.; Yang, X. Q.; Guo, Y. G.; Gu, L.; Wan, L. J. High-Capacity Cathode Material with High Voltage for Li-Ion Batteries. *Advanced Materials* **2018**, *30* (9). https://doi.org/10.1002/adma.201705575.

(16) Winter, M. The Solid Electrolyte Interphase – The Most Important and the Least Understood Solid Electrolyte in Rechargeable Li Batteries. *Zeitschrift Fur Physikalische Chemie-international Journal of Research in Physical Chemistry & Chemical Physics - Z PHYS CHEM* **2009**, *223*, 1395–1406. https://doi.org/10.1524/zpch.2009.6086.

(17) Kennedy, T.; Brandon, M.; Laffir, F.; Ryan, K. M. Understanding the Influence of Electrolyte Additives on the Electrochemical Performance and Morphology Evolution of Silicon Nanowire Based Lithium-Ion Battery Anodes. *J Power Sources* **2017**, *359*, 601–610. https://doi.org/10.1016/J.JPOWSOUR.2017.05.093.

(18) Schweidler, S.; de Biasi, L.; Schiele, A.; Hartmann, P.; Brezesinski, T.; Janek, J. Volume Changes of Graphite Anodes Revisited: A Combined Operando X-Ray Diffraction and in Situ Pressure Analysis Study. *Journal of Physical Chemistry C* **2018**, *122* (16), 8829–8835. https://doi.org/10.1021/ACS.JPCC.8B01873/SUPPL_FILE/JP8B01873_SI_001.PDF.

(19) McDowell, M. T.; Lee, S. W.; Nix, W. D.; Cui, Y. 25th Anniversary Article: Understanding the Lithiation of Silicon and Other Alloying Anodes for Lithium-Ion Batteries. *Advanced Materials*. September 2013, pp 4966–4985. https://doi.org/10.1002/adma.201301795.

(20) Waldmann, T.; Wohlfahrt-Mehrens, M. Effects of Rest Time after Li Plating on Safety Behavior—ARC Tests with Commercial High-Energy 18650 Li-Ion Cells. *Electrochim Acta* **2017**, *230*, 454–460. https://doi.org/10.1016/J.ELECTACTA.2017.02.036.

(21) Freytag, A. I. *Lithium Plating on Silicon Anodes Visualized through In Situ NMR*.

(22) Key, B.; Morcrette, M.; Tarascon, J. M.; Grey, C. P. Pair Distribution Function Analysis and Solid State NMR Studies of Silicon Electrodes for Lithium Ion Batteries: Understanding the (de)Lithiation Mechanisms. *J Am Chem Soc* **2011**, *133* (3), 503–512. https://doi.org/10.1021/ja108085d.

(23) Michan, A. L.; Divitini, G.; Pell, A. J.; Leskes, M.; Ducati, C.; Grey, C. P. Solid Electrolyte Interphase Growth and Capacity Loss in Silicon Electrodes. *J Am Chem Soc* **2016**, *138* (25), 7918–7931. https://doi.org/10.1021/jacs.6b02882.

(24) Zuo, X.; Zhu, J.; Müller-Buschbaum, P.; Cheng, Y. J. Silicon Based Lithium-Ion Battery Anodes: A Chronicle Perspective Review. *Nano Energy*. Elsevier Ltd January 1, 2017, pp 113–143. https://doi.org/10.1016/j.nanoen.2016.11.013.

(25) Key, B.; Bhattacharyya, R.; Morcrette, M.; Seznéc, V.; Tarascon, J. M.; Grey, C. P. Real-Time NMR Investigations of Structural Changes in Silicon Electrodes for Lithium-Ion Batteries. *J Am Chem Soc* **2009**, *131* (26), 9239–9249. https://doi.org/10.1021/ja8086278.

(26) Iaboni, D. *Li15Si4 Formation in Thin Film Si Negative Electrodes for Li-Ion Batteries*; 2015.

(27) Wu, H.; Cui, Y. Designing Nanostructured Si Anodes for High Energy Lithium Ion Batteries. *Nano Today*. October 2012, pp 414–429. https://doi.org/10.1016/j.nantod.2012.08.004.

(28) Ogata, K.; Salager, E.; Kerr, C. J.; Fraser, A. E.; Ducati, C.; Morris, A. J.; Hofmann, S.; Grey, C. P. Revealing Lithium-Silicide Phase Transformations in Nano-Structured Silicon-Based Lithium Ion Batteries via in Situ NMR Spectroscopy. *Nat Commun* **2014**, *5*. https://doi.org/10.1038/ncomms4217.

(29) Li, J.; Dudney, N. J.; Nanda, J.; Liang, C. Artificial Solid Electrolyte Interphase to Address the Electrochemical Degradation of Silicon Electrodes. *ACS Appl Mater Interfaces* **2014**, *6* (13), 10083–10088. https://doi.org/10.1021/am5009419.

(30) Wang, Y.; Satoh, M.; Arao, M.; Matsumoto, M.; Imai, H.; Nishihara, H. High-Energy, Long-Cycle-Life Secondary Battery with Electrochemically Pre-Doped Silicon Anode. *Sci Rep* **2020**, *10* (1), 3208. https://doi.org/10.1038/s41598-020-59913-4.

(31) Nysted, V. S. *The Galvanostatic Intermittent Titration Technique for Silicon-Based Li-Ion Battery Anodes: Theory and Experimental Validation*.

(32) Song, M.; Nadimpalli, S. P. v.; Sethuraman, V. A.; Chon, M. J.; Guduru, P. R.; Wang, L.-Q. Investigation of Initial Lithiation of Silicon (100) Using Solid-State 7 Li NMR . *J Electrochem Soc* **2014**, *161* (6), A915–A919. https://doi.org/10.1149/2.033406jes.

(33) Trill, J. H.; Tao, C.; Winter, M.; Passerini, S.; Eckert, H. NMR Investigations on the Lithiation and Delithiation of Nanosilicon-Based Anodes for Li-Ion Batteries. *Journal of Solid State Electrochemistry* **2011**, *15* (2), 349–356. https://doi.org/10.1007/s10008-010-1260-0.

(34) Sanders, K. J.; Aguilera, A. R.; Keffer, J. R.; Balcom, B. J.; Halalay, I. C.; Goward, G. R. Transient Lithium Metal Plating on Graphite: Operando 7Li Nuclear Magnetic Resonance Investigation of a Battery Cell Using a Novel RF Probe. *Carbon N Y* **2022**, *189*, 377–385. https://doi.org/10.1016/j.carbon.2021.12.082.

(35) Pecher, O.; Carretero-Gonzalez, J.; Griffith, K. J.; Grey, C. P. Materials' Methods: NMR in Battery Research. *Chemistry of Materials*. American Chemical Society January 10, 2017, pp 213–242. https://doi.org/10.1021/acs.chemmater.6b03183.

Chapter 2

Nuclear Magnetic Resonance Theory

2.1 Nuclear Spin and Magnetic Field

NMR spectroscopy can probe local chemical structures in molecules and materials based on the interaction of the magnetic moment of a nucleus with a magnetic field. The nucleus can be thought of as a small, charged particle spinning around its axis. Spinning the charged particle creates an electric current, producing a small electromagnet. The charged particle is not actually rotating from spinning, but the spin itself is rather an intrinsic physical property first derived by Dirac in his study of quantum mechanics and relativity.[1] Therefore, the nuclear spin quantum number is represented by I, and is related to the spin angular momentum $\hat{S}$ by equation 2.1

$$\hat{S} = \hbar \cdot \sqrt{I(I+1)} \qquad \text{Eq. 2.1}$$

Where $\hbar$ is the reduced Planck constant. A nuclear state with spin I is (2I + 1)-fold degenerate at ground state. When a magnetic field is applied the degeneracy (same energy) is broken and causes each (2I + 1) sublevels to have slightly different energies. This is called the Zeeman effect and the separation between the sublevels in a magnetic field are called the Zeeman splitting. Examples of the nuclear Zeeman levels seen in NMR for ^{1}H nucleus, a ^{15}N nucleus, and a ^{27}Al nucleus are shown in Figure 2.1. The nuclear ground states and split into two sublevels for ^{1}H nucleus and ^{15}N nucleus as they are both spin -1/2, therefore 2 x (1/2) + 1 = 2 which holds true. The ^{27}Al nucleus is spin 5/2 and therefore the ground state splits into six level (since, 2 x (5/2) + 1 = 6) in the applied magnetic field.

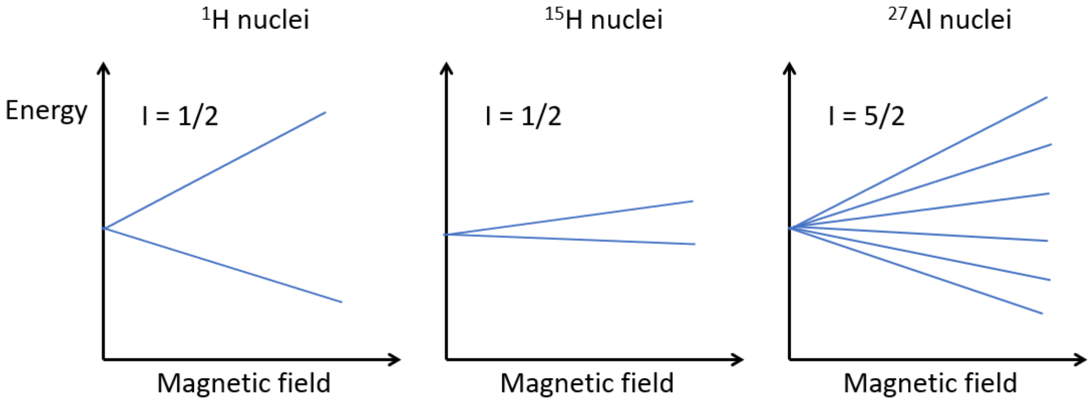

Figure 2.1: Nuclear Zeeman sublevels of ^{1}H, ^{15}N, ^{27}Al nucleus ground states.

The spin angular momentum $\hat{S}$ seen in equation 2.1 is also related to the magnetic moment $\hat{\mu}$, plus a proportionality constant which is the gyromagnetic ratio γ, equation 2.2. The gyromagnetic ratio provides information regarding sensitivity of the magnetic moment in an external magnetic field.

$$\hat{\mu} = \gamma \cdot \hat{S} \qquad \text{Eq. 2.2}$$

The energy levels that occur upon Zeeman splitting are described by equation 2.3, where E_m are the energy levels and m are the magnetic quantum number (taking the place of I, so m = ±1/2 for ^{1}H for example). The B_0 is the magnetic field strength of the applied field aligned with the z-axis.

$$\begin{aligned} E_m &= -\hat{\mu}_z \vec{B}_0 \qquad \text{Eq. 2.3} \\ &= -m\hbar\gamma\vec{B}_0 \end{aligned}$$

The separation between the ground energy level ΔE split because of the Zeeman effect is characterized by

$$\Delta E = E_{\beta} - E_{\alpha} \qquad \text{Eq. 2.4}$$

$$= \frac{1}{2}\hbar\gamma\vec{B}_0 - \left(-\frac{1}{2}\hbar\gamma\vec{B}_0\right)$$

$$= \hbar\gamma\vec{B}_0$$

The energy level separation seen in Figure 2.1 is dependent on both the gyromagnetic ratio γ, and the applied field $\vec{B}_0$. Nuclei with greater gyromagnetic ratio have a large ΔE and are more sensitive to the nuclear magnetic resonance response. The proton nucleus Zeeman splitting is approximately 10 times large than that for ^{15}N at the same magnetic field because the proton is 10x more magnetic than ^{15}N nuclei.[1] It is therefore beneficial to work at higher applied field $\vec{B}_0$ for the same reasons, to maximise energy level separation.

ΔE can be expressed in frequency units, known as the Larmor frequency ω_0 (in rad s^{-1}) and is obtained by dividing ΔE by $\hbar$. The magnetic moments or nuclear spins can be thought of as tiny compass needles, and under the influence of an external magnetic field at equilibrium align to produce a net magnetization along the direction of the applied field (B_0, typically identified as the z-axis). By using a radiofrequency (RF) pulse while B_0 is applied, the magnetization vector is tilted away from the z-axis and precesses about the field. This motion is called the Larmor precession and is related to the magnetic field strength B_0 by equation 2.5 and 2.6.

$$\omega_0 = -\gamma B_0 \qquad \text{Eq. 2.5}$$

$$\nu_0 = -\frac{1}{2\pi}\gamma B_0 \qquad \text{Eq. 2.6}$$

Where ω_0 and ν_0 are the Larmor precession in rad s^{-1} and frequency (Hz) and γ is the gyromagnetic ratio. These equations communicate that the magnetization precesses frequency around B_0 is exactly the frequency of the line on a spectrum for a one spin system. Numerous nuclei are observed in an NMR experiment and therefore the net effect of these nuclei will be observed. To acquire an NMR spectrum the magnetization would need to shift away from the z axis and into the xy-plane. Consequently, a RF pulse at the Larmor frequency ω_0 can be used to create an oscillating magnetic field in the transverse plane (along the x-axis). This result in the creation of a RF field commonly known as the $\vec{B}_1$ field, and is related to the RF mutation frequency ω_1

$$\omega_1 = |\gamma|\vec{B}_1 \qquad \text{Eq 2.7}$$

ω_1 is always positive and therefore the absolute value of γ is required. The RF pulse allows the magnetization vector to precess about the $\vec{B}_0$ field at a flip angle β. Figure 2.2 shows how the magnetization rotates around the field.

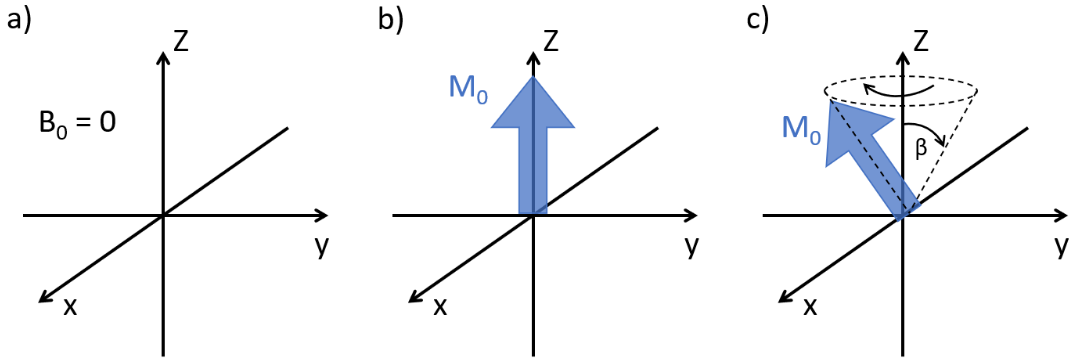

Figure 2.2: representation of the increase of magnetization in a magnetic field. a) net magnetization vector equals zero, no applied field. b) The $\vec{B}_0$ field is employed along the z-axis and the magnetization M_0 is aligned with the field after time T_1. c) Once the RF pulse is applied, it moves the M_0 out of equilibrium, allowing a precession about the z-axis at the Larmor frequency with a flip angle β.

The RF pulse duration or strength can be manipulated, and different flip angles can be achieved. For example, when an RF pulse along the x-axis with a flip angle of 90^o is applied the magnetization vector M_0 will rotate onto the -y-axis (right-hand rule). Once the pulse is turned off, the magnetization vector M_0 will start to processes around the $\vec{B}_0$ field. This precession decays over time in the transverse plane and the oscillating magnetization vector can be broken up into both x- and y- components. The decay in magnetization or free induction decay (FID), is detected by a wire coil placed in the x-y plane and induces a current in the coil. After acquisition of the FID in the time domain, this data is processed via a Fourier transform function and a spectrum is produced in the frequency domain.

2.2 Magic-Angle Spinning

NMR on solid materials typically present a broader and more complex spectra than liquids. In solid state NMR the particle motion is significantly slower than in liquid or gas and therefore there is little to no averaging of the internal spin interactions. The orientation of the sample with respect to the magnetic field becomes relative because unlike in solution state NMR, both intramolecular and intermolecular spin interactions contribute to the spectra seen. Figure 2.3 adapted from Levitt[1], indicates the effect orientation can have on the NMR spectrum. Figure 2.3 a) gives the example of a single crystal in a solid molecule. In the simplest case all the molecules are lined up and have the same orientation. The result moves the chemical shift in the same direction for all the molecules depending on the orientation of the crystal with respect to the magnetic field. However in a powder, which is the typically solid used in ssNMR the molecules can all have different orientation. This makes the powder spectrum extremely broad because the chemical shift of each crystallite is different. The powder pattern seen in Figure 2.3 b) is a result of the superposition of many sharp peaks with different frequencies, from the crystallite with different orientations. Therefore, resolution can be problematic in solids because: line shapes from inequivalent sites overlap, multiple interactions resulting in the broad featureless line shapes, and anisotropic interaction can also play a role in powder patterns. In anisotropic material, sample are orientation dependent, and the induced magnetic moment is not necessarily in the same direction as the applied field.

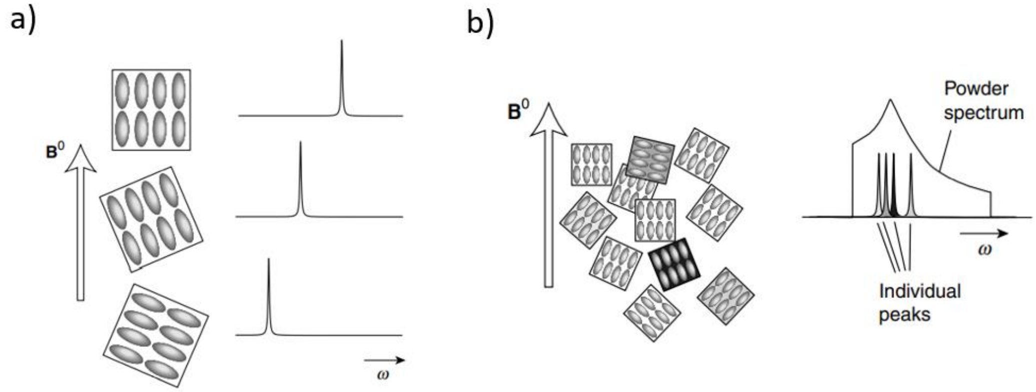

Figure 2.3: a) chemical shift dependency on solid orientation with respect to the magnetic field. b) Powder pattern formation. Reprinted with permission from Levitt, M. H., Spin dynamics basics of nuclear magnetic resonance. 2nd ed. ed.; John Wiley & Sons Ltd: Chichester, West Sussex, England; Hoboken, N.J., 2008. Copyright 2008 John Wiley and Sons.[1]

To mimic the solution state conditions magic-angle spinning (MAS) NMR can be used to increase the resolution and combat the problems with ssNMR highlighted previously. Specialized probes allow for rapid spinning of a sample inside a ceramic rotor that varies in size anywhere between 8 – 0.7 mm. The sample in spun at a specific angle with respect to the magnetic field known as the magic angle which is 54.74°. Spinning between the ranges of 5 – 100 kHz for the 8 mm and 0.7 mm rotor, respectively can be achieved by applying bearing and drive gas to the rotor.[2] The bearing gas “float” the rotor in the probe, while the drive gas allows the rotor to spin by pushing the fins on the rotor cap to spin. When the sample is spinning in the rotor, the spinning sidebands occur to the left and right of the isotropic peak separated by the spinning frequency. To avoid overlap of spinning sidebands with the chemical shift environment of interest high spinning rates are needed.

2.3 *Ex situ* NMR Experiments

The primary NMR experiments used for the *ex situ* characterization on material in Chapter 3 was the pulse sequence depicted in Figure 2.4 a). The pulse-acquire experiment was used to collect the one-dimensional spectra and the inversion recovery experiment was used to collect information regarding T1 relaxation (Figure 2.4 b). The pulse-acquire experiment proceeds by three steps: 1. The sample comes to equilibrium, 2. An Rf pulse is applied for long enough to rotate the magnetization through 90^o, 3. After the pulse is finished signal is detected which occurs from the rotating magnetization in the transverse plane. In contrast to the pulse-acquire the inversion recovery experiment uses two pulses. The 180^o pulse rotates the equilibrium magnetization to the -z axis, and then a delay time τ is added before a 90^o pulse is applied to rotate the magnetisation onto the +y axis so the spectrum can be acquired. The time of delay τ starts off short and then increases as the experiment continues, this allows for the recovery rate of the z-magnetization to be determined.[3] T1 relaxation (longitudinal relaxation) is the net magnetization growth to its initial maximum value parallel to B_o, or in layman terms the time it takes for the magnetization to reach equilibrium. T1- relaxation provides insight into the dynamic motion of nuclear spin rates which can occur on the order of milliseconds to seconds.[2] T_1 was determined prior to running the pulse-acquire experiment because the T_1 value provides insight into how long the recycle delay (d1) should be set for the NMR experiment on the material of interest. Ideally d1 should be set to 5*T_1 which allows for 99% of the net magnetization M_0, to move back to equilibrium parallel to the $\vec{B}_0$ field.[4,5]

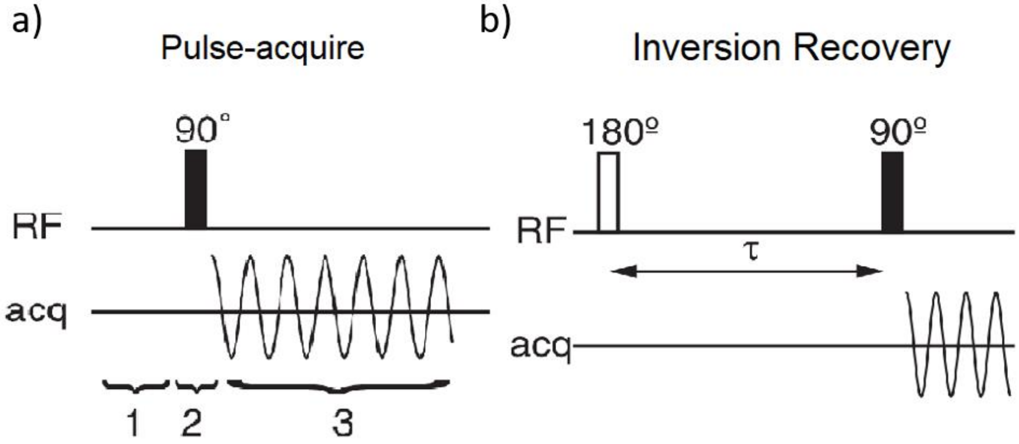

Figure 2.4: The pulse sequence for a pulse-acquire and inversion recovery NMR experiments. Reprinted from Understanding NMR Spectroscopy, 2002, 3-10, 3-15.[3]

To understand the dynamics between different chemical environments, a sample two-dimensional exchange spectroscopy (EXSY) is used. The NMR pulse sequence for this technique is seen in Figure 2.5. Like the pulse acquire experiment the first 90° pulse flips the spins into the transverse plane. The τ_1 delay allows for the precession of non-exchanging spins, this is called the frequency labeling period and corresponds to the diagonal peaks in a two-dimensional EXSY spectrum. The second 90° pulse flips the spins back into the longitudinal plane. Next is τ_m, which is referred to as the mixing time. This acquisition time is kept fixed for each two-dimensional experiment and allows a loss of magnetization to occur due to exchange in the sample. The final 90° pulse flips the spins into the transverse plane and the data is acquired.

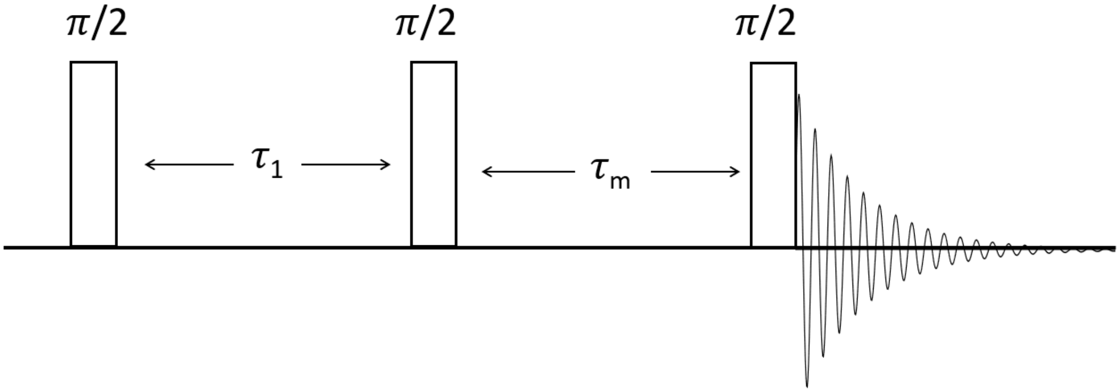

Figure 2.5: EXSY pulse sequence. Which included three 90° pulses and two delays. τ_1*, is the arrayed signal acquisition with a time delay.* τ_m *is the mixing time where exchange takes place.*[1]

The EXSY experiment produces a two-dimensional spectrum where the peaks along the diagonal relate to the one-dimensional spectrum, and the off-diagonal peaks indicate where exchange between different sites has occurred. Figure 2.6 shows an illustration of a EXSY spectrum. The two-dimensional experiment communicates both the frequency (position) and amplitude (intensity) of the diagonal and off-diagonal peaks. When cross peaks are present it indicates that exchange between the different chemical species in the sample has taken place. For example, in Figure 2.6 the frequency coordinates that correspond to exchange between site A and B are (ΩA^0, ΩB^0) and (ΩB^0, ΩA^0) respectively.[1] By collecting multiple different mixing times, the EXSY pulse sequence can be used quantitively. By examining the intensity growth of the cross-peaks as a function of mixing time, a rate constant for the exchange process can be identified.

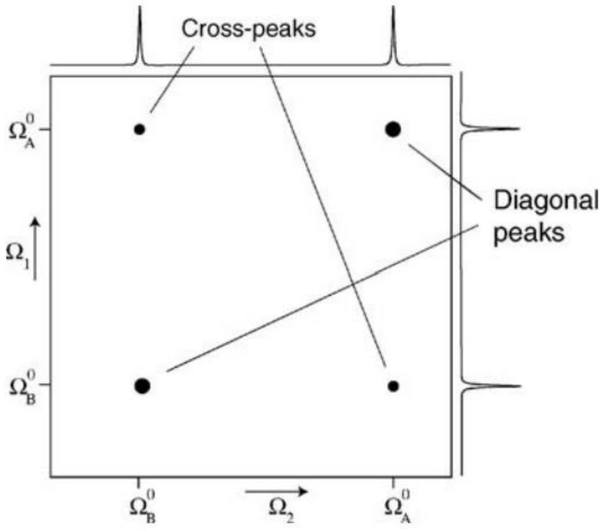

Figure 2.6: Schematic form of a two-dimensional exchange spectrum. Reprinted with permission from Levitt, M. H., Spin dynamics basics of nuclear magnetic resonance. 2nd ed. ed.; John Wiley & Sons Ltd: Chichester, West Sussex, England; Hoboken, N.J., 2008. Copyright 2008 John Wiley and Sons.[1]

2.4 *In Situ* vs. *Operando* NMR Experiments

In-situ NMR has become a powerful technique used in the last two decades to study battery materials. This experimental design allows for all the components (electrolyte, cathode, and anode) of the battery to be monitored simultaneously without the need of disassembling the electrochemical cell. *In-situ* data acquisition can provide information regarding structural changes, degradation products and failure mechanisms in the battery and is performed while the electrochemical cell rests at OCV. In contrast, during an operando NMR experiment, a operating battery is placed into a probe and the two are then inserted into the bore of the NMR spectrometer. NMR data are collected while the cell is simultaneously connected to electrochemical instrumentation and undergoes some electrochemical testing protocol. Some challenges with both *in-situ* and *operando* experiments include bulk magnetic susceptibility (BMS), material/cell design, and battery lifetime. Most *in-situ* and *operando* cell designs are static and therefore the challenges with large peak widths become problematic, as MAS is no longer viable. Fortunately, no paramagnetic material was investigated in the present study, therefore the Li_xSi phases could still be deconvoluted with ssNake from the *operando* NMR data.[6] Depending on the orientation of the electrochemical cell inside the magnet, different cell elements can cause changes in the local magnetic fields, known as bulk magnetic susceptibility (BMS). For example, lithium metal is orientation dependent with respect to the $\vec{B}_0$ field. To achieve reproducible results the reusable cartridge single layer cell container[7] was always placed vertical to the $\vec{B}_0$ field in a parallel-plate resonator designed by Ramirez Aguilera et al.[8,9] The cartridge cell designed used for the *operando* work presented in this thesis (Chapter 4), was created by Sanders et al[7]., and polyetheretherketone (PEEK) was determined has the best material for the cell. Solvent leakages and pressure differences inside the electrochemical cell can also be problematic and lead to a finite life span. It is important to research and test any in situ designed and material before running experiments to determine how the cell will preformed and adapt a reasonable time frame. Currently the cartridge cell can last for approximately two – three weeks outside of an air sensitive environment. Further improvements are being developed to seal the cell in a plastic bag/pouch to further avoid any leaks to the atmosphere.

Operando/in-situ NMR provides real-time information regarding changes to the chemical environment of a material as a function of state of charge. Although there are larger challenges inherit to the *operando* experiment in comparison to *ex-situ* NMR, it provides data regarding dynamics and metastable/intermediate phases that are often not detectable by *ex-situ* characterization methods.[10]

2.5 ^{7}Li NMR details: silicon anode material

Silicon anodes were first studied via NMR methods in the early 2000's.[11,12] Other methods like X-ray diffraction have previously tried to determine the electrochemical lithiation mechanism, however due to the amorphous nature of the silicon network were unsuccessful. Kitada et al.[13] used both *Ex situ*/in situ NMR to determine Li_xSi structures, and their corresponding ^{7}Li NMR chemical shifts, as seen in Figure 3.[11–14] Phase 1 corresponds to polymeric silicon clusters with isolated lithium distributed in the network at chemical shift values of 0 ppm to 10 ppm. At higher states of lithiation, these clusters are broken down into star and dumbbell-shaped Si clusters with some isolated silicon, with chemical shift values in the range of 10 ppm to 20 ppm. Phase 3 was identified as the most lithiated phase, between 5 ppm to −15 ppm. This has been called a metastable phase which was not visible during *ex situ* ^{7}Li NMR. Further analysis of that phase revealed it corresponded to the $Li_{15}Si_4$, which is of a crystalline nature. The language of phase 1, 2, and 3 will be used throughout this thesis to refer to these distinct phases seen in NMR spectra.

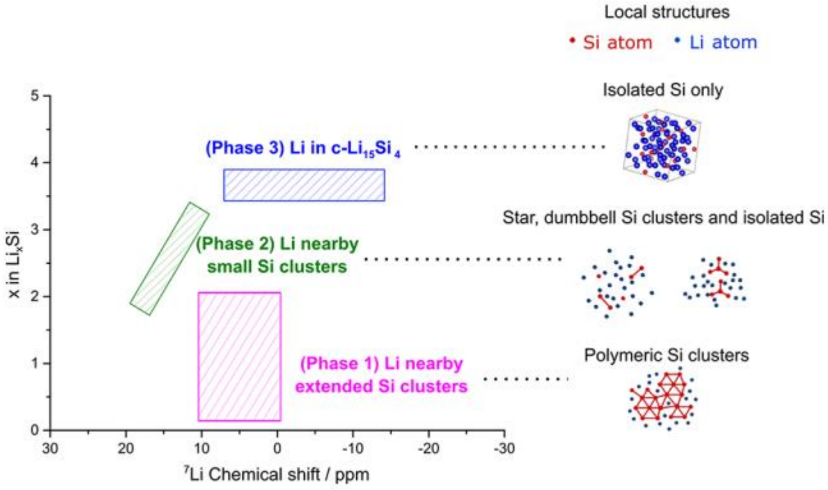

Figure 2.7: ^{7}Li chemical shifts and structures of LixSi phases as a function of state of charge. Reprinted from The Journal of the American Chemical Society, 2019, 141, 17, 7014–7027[41][13]. Copyright © 2019, American Chemical Society.

2.6 References

(1) Levitt, M. H. *Spin Dynamics Basics of Nuclear Magnetic Resonance Second Edition*.

(2) Reif, B.; Ashbrook, S. E.; Emsley, L.; Hong, M. Solid-State NMR Spectroscopy. *Nature Reviews Methods Primers* **2021**, *1* (1). https://doi.org/10.1038/s43586-020-00002-1.

(3) Keeler, J. *Understanding NMR Spectroscopy*.

(4) *NMR T1 & T2 Relaxation | Oilfield Knowledge*. http://www.oilfieldknowledge.com/nmr-t1-t2-relaxation/ (accessed 2022-10-30).

(5) *T1 relaxation - Questions and Answers in MRI*. https://mriquestions.com/what-is-t1.html (accessed 2022-10-30).

(6) van Meerten, S. G. J.; Franssen, W. M. J.; Kentgens, A. P. M. SsNake: A Cross-Platform Open-Source NMR Data Processing and Fitting Application. *Journal of Magnetic Resonance* **2019**, *301*, 56–66. https://doi.org/10.1016/j.jmr.2019.02.006.

(7) Sanders, K. J.; Aguilera, A. R.; Keffer, J. R.; Balcom, B. J.; Halalay, I. C.; Goward, G. R. Transient Lithium Metal Plating on Graphite: *Operando* 7Li Nuclear Magnetic Resonance Investigation of a Battery Cell Using a Novel RF Probe. *Carbon N Y* **2022**, *189*, 377–385. https://doi.org/10.1016/j.carbon.2021.12.082.

(8) Zhang, Z.; Marble, A. E.; MacGregor, R. P.; Martin, J.; Wang, H.; Balcom, B. J. Zero-Mode TEM Parallel-Plate Resonator for High-Resolution Thin Film Magnetic Resonance Imaging. *Can J Chem* **2011**, *89* (7), 745–753. https://doi.org/10.1139/v11-018.

(9) Ramírez Aguilera, A.; MacMillan, B.; Goward, G. R.; Balcom, B. J. Optimization of a Parallel-Plate RF Probe for High Resolution Thin Film Imaging. *Concepts in Magnetic Resonance Part A* **2018**, *47A* (1), e21465. https://doi.org/https://doi.org/10.1002/cmr.a.21465.

(10) Pecher, O.; Carretero-Gonzalez, J.; Griffith, K. J.; Grey, C. P. Materials' Methods: NMR in Battery Research. *Chemistry of Materials*. American Chemical Society January 10, 2017, pp 213–242. https://doi.org/10.1021/acs.chemmater.6b03183.

(11) Key, B.; Bhattacharyya, R.; Morcrette, M.; Seznéc, V.; Tarascon, J. M.; Grey, C. P. Real-Time NMR Investigations of Structural Changes in Silicon Electrodes for Lithium-Ion Batteries. *J Am Chem Soc* **2009**, *131* (26), 9239–9249. https://doi.org/10.1021/ja8086278.

(12) Key, B.; Morcrette, M.; Tarascon, J. M.; Grey, C. P. Pair Distribution Function Analysis and Solid State NMR Studies of Silicon Electrodes for Lithium Ion Batteries: Understanding the (de)Lithiation Mechanisms. *J Am Chem Soc* **2011**, *133* (3), 503–512. https://doi.org/10.1021/ja108085d.

(13) Kitada, K.; Pecher, O.; Magusin, P. C. M. M.; Groh, M. F.; Weatherup, R. S.; Grey, C. P. Unraveling the Reaction Mechanisms of SiO Anodes for Li-Ion Batteries by Combining in Situ 7Li and *Ex situ* 7Li/29Si Solid-State NMR Spectroscopy. *J Am Chem Soc* **2019**, *141* (17), 7014–7027. https://doi.org/10.1021/jacs.9b01589.

(14) Michan, A. L.; Divitini, G.; Pell, A. J.; Leskes, M.; Ducati, C.; Grey, C. P. Solid Electrolyte Interphase Growth and Capacity Loss in Silicon Electrodes. *J Am Chem Soc* **2016**, *138* (25), 7918–7931. https://doi.org/10.1021/jacs.6b02882.

Chapter 3

Ex-situ solid-state NMR study of silicon anode material as a function of cycle number

Data collection and analysis were performed by Amanda A. Ciezki. Kevin J. Sanders assisted in the collection of nuclear magnetic resonance (NMR) data. Nafiseh Zaker collected the scanning electron microscopy (SEM) image. Measurements were performed at McMaster University.

3.1 Introduction

In recent years, silicon has become a material of interest as a potential alternative to the conventional negative electrode, graphite found in LIBs. The superior gravimetric capacity of 3579 mAh g^{-1} for silicon versus that of 372 mAh g^{-1} for graphite is advantages, and the primary benefit of silicon.[1] Silicon follows an alloying mechanism can accommodate for more lithium ions in the structure, and as such fits the criteria for the next generation of anode material.

Theoretically, silicon is a promising material for LIBs but unfortunately suffers from rapid capacity loss as a function of cycle number.[2] Due to the alloying mechanism upon lithiation silicon can host four lithium atoms. This uptake of lithium atoms accounts for the significantly large capacity but also leads to substantial volume changes. The ~300% volume expansion during lithiation and latter contraction during lithium extraction puts significant stress on the silicon material and can lead to cracking and pulverization.[3] Another challenge with silicon electrodes is delamination from the current collect due to the large volume changes. Using SEM previous studies found that silicon clusters were only weakly bounded to the current collector by small points of contact after repeated cycling and formation of significant $Li_{15}Si_4$.[4] At the top of charge (TOC), $Li_{15}Si_4$ the most highly lithiated phase formed electrochemical has been linked with capacity fade and delamination of silicon from the current collector. The final major contributor to capacity fade within the silicon material is instability and build up of solid electrode interphase (SEI) also due to the large volume change.[2,3,5,6] In a full cell, when the battery is charged lithium ions move into the silicon via the SEI layer. As lithium ions alloy to the silicon, volume expansion occurs and leads to SEI cracking. Lithium continues to diffuse through the SEI but also through its cracks, and the fresh silicon particles exposed leads to more growth through the loss and breakdown of the electrolyte. During delithiation and volume contraction leads to the SEI separating into pieces. The thickening SEI layer impedes the diffusion of lithium ions, increases resistance, and decreasing the electrolyte components and loss of electrodes electrochemical reactivity.[7]Although there are some inherent pitfalls with silicon, the electrochemistry is well understood in the literature and many highly cited articles have suggested solutions like restricting the electrode potential, so $Li_{15}Si_4$ does not form leading to the significant volume expansion as a solution.[8]

The lithium silicide that forms electrochemically are amorphous in nature, and therefore structural changes that occur upon lithiation and delithiation cannot be monitored with conventional methods such as diffraction. With nuclear magnetic resonance (NMR) spectroscopy detailed regarding the lithium local environments can be obtained. Many studies previously published have used ^{7}Li NMR as a technique to identify different phases within the lithium silicides depending on the lithium resonances at distinct chemical shift ranges.[6,8–15] ^{29}Si NMR can also provide insight into the silicon local environments, however its natural abundance is only 4.7% making sensitivity a challenge.[16] Goward et al., found the chemical shifts in ^{29}Si MAS (magic-angle spinning) NMR to be broad because of the amorphous lithium silicides and as a result individual silicide phases could not be resolved regardless of field strength and spinning speed.[12]

In this chapter *ex situ* ^{7}Li MAS ssNMR was used to observe the changes in the local chemical environments of silicon after electrochemical cycling the material in a full cell to various cycle numbers. Previous work in the field has primarily focused on only the initial cycles and quantifying the various Li_xSi phases present.[9,10,15] The *ex situ* work performed by Grey et al., used a half cell with lithium metal as the counter electrode and silicon as the anode of interest. The NMR and X-ray pair distribution function (PDF) analyses of the first and second cycles used to identify local structures that are correlated with specific electrochemical signatures was one of the first breakthrough papers using ssNMR on silicon anode material. The "half-cell" set up used by Grey et al., is common because lithium as a counter electrode employs an excess of metal, which is assumed to maintain a constant potential. This also negates the need for electrode balancing and eliminates variables in the electrochemical setup.[17] In this research commercial grade silicon anode and NMC cathode were used (provided by General Motors) instead of a half-cell, to mimic a similar electrochemical setup as that in an EV. Commercial EV use full cells with an anode and cathode material (i.e., lithium cobalt oxide, lithium iron phosphate, lithium manganese oxide, or lithium nickel manganese cobalt (NMC)) which provide greater energy density.

Another gap within the field of NMR on silicon anode material regards how cell aging effects the local environments of Li_xSi. To the authors knowledge no ssNMR studies have been conducted on silicon after advanced cycle lengths. This study aims to showcase the differences in LixSi phases as full coin cell batteries advance to different cycle numbers. *Ex situ* MAS ssNMR was the primary method employed to analyze the structure and dynamics of silicon at different cycle numbers. The sensitivity of NMR allows for small changes within the different phases to be detected.

This work will add to the understanding of the short-range local environments present in aging silicon electrodes using NMR that has yet to be reported in literature. Scanning electron microscopy (SEM) of silicon electrodes after various cycle lengths, also confirm changes to the bulk material as the cell ages. The following results provide insight into breakdown mechanisms of silicon previously reported in literature as summarized above.

3.2 Experimental

Coin cells were prepared with $LiNi_{0.6}Mn_{0.2}Co_{0.2}O_2$ (NMC622, General Motors, 28.86 mg/cm^2, 4.5 mA h/cm^2) as cathode, and silicon (General Motors, 2.7 mg/cm^2, 9 mA h/cm^2) as the anode. Two half-inch diameter circle Celgard 2325 separator with 100 µL of 1 M lithium hexafluorophosphate in fluorinated ethylene carbonate/ ethyl methyl carbonate 1:4 wt% ($LiPF_6$ FEC/EMC 1:4 wt%) were also used in the coin cell construction. The silicon electrode was first heat-treated at 350 °C under N_2 in a tube furnace and all electrodes and coin cell components were dried under vacuum at 80 °C overnight and then transferred into an Ar-filled glovebox (M Braun, <3 ppm H_20, <3 ppm O_2).

An Arbin BT2000 battery cycler was used to cycle coin cells prior to *ex situ* NMR date collection. A prelithiation process was first performed on the silicon anode material where a full cell was configured and a constant current of 0.3 mA (corresponding to a ~C/20 rate), with a voltage limit of 4.2 V was used to prelithiate the silicon material to 50 % of its specific capacity (9 mA h/cm^2). After this initial prelithiation the coin cell was transferred back into the glove box and taken apart via a coin cell disassembling tool. The prelithiated silicon material was then transfer into a new coin cell and all other components including the sacrificial cathode of the original cell were discarded. The prelithiated silicon coin cell was taken out of the glove box and two C/20 formation charge/discharge cycles with a constant current of 0.3 mA were performed, followed by C/3 cycles using a constant current of ~2 mA (current depended on capacity of 2nd discharge cycle).

NMR measurements of *ex situ* cells were performed at several points in the charge/discharge process including at the top of charge (TOC) and the bottom of discharge (BOD). Experiments were collected using a Bruker Avance III HD wide-bore instrument at 7.05 T with a nominal ^{7}Li frequency of 116.7 MHz and a 1.3 mm double resonance probe was employed for fast MAS rates of 40 kHz. ^{7}Li chemical shifts are referenced with respect to solid LiCl. A pulse-acquisition sequence with a 1.25 μs π/2 pulse was applied for one-dimensional *ex situ* NMR experiments. 8192 FID points were acquired, and 128 scans were collected. The spectral width was 3897 ppm, and an exponential window function of 10 Hz was used across the spectra to improve the signal-to-noise ratio. The recycle delay varied depended on the relaxation time T1 for each sample, to achieve maximum sensitivity, Table 3.1. The delay time was set to five times the T1 to recover all the signal and allow the spins to relax back to equilibrium before the next RF pulse. NMR spectra were processed and deconvoluted using ssNake and both Lorentz and Gauss shaped curves were used to fit the data.[18]

*Table 3.1: delay times used for each longevity experiment based on 5*T1 to reach maximum sensitivity*

Cycle count	*Delay time D1 (sec): TOC*	*Delay time D1 (sec): BOD*
10	9.7	6.1
25	5.0	6.4
50	4.8	10.4
100	2.8	11.4
200	3.5	12.5

Two-dimensional EXSY experiments were carried out at room temperature for samples collected at the BOD after 50, 100, and 200 cycles using the standard 90-t_1-90-t_{mix}-90 pulse sequence. Spectra using the mixing times of 10, 1, 0.5, and 0.1 ms were acquired for the sample cycled 50 times with a recycle delay (D1) of 2.22 secs. Silicon material cycled 100 and 200 times had mixing times of 10, 5, 1, 0.5, 0.1 ms and 50 us and D1 values of 2.75 secs and 3.53 secs, respectably. The FID size was 9988 in the direct dimension, the number of scans collected per experiment was 128, and the sweep width was 857 ppm, respectably.

3.3 Results and Discussion

To evaluate the silicon material an initial electrochemical cycling tests was collected. Figure 3.1 shows the voltage vs. time (Figure 3.1 a) and voltage vs. capacity (Figure 3.1 b) plots of a coin cell with silicon material that was first prelithiated followed by two formation cycles, and a C/3 cycle. Each different cycle in Figure 3.1. was performed sequentially with a different current to control the rate of charge. The silicon material is first prelithiated using a sacrificial cathode. By storing 'extra' lithium in the silicon material there is a reservoir of lithium ions to pull from, and the initial irreversible capacity fade which starts at the first charge during the SEI formation can be mitigated.[19] Forming a stable SEI layer is key to combat the decomposition of the electrolyte at the surface of the anode.[20,21] Anode prelithiation has also already been proven to be an effective strategy to counterbalance ion depletion.[19,22] The discharge capacity between the two formation cycles seen in figure 3.1 b) were 162.9 Ah/g and 164.4 mAh/g respectably, indicating no significant capacity fade was present between these cycles. Only after the current was increased to preform a C/3 cycle did the capacity drop to 138.47 mAh/g. These results suggest the faster cycling rate plays a role in capacity loss. Although there are capacity losses with increased current the cell performed as expected.

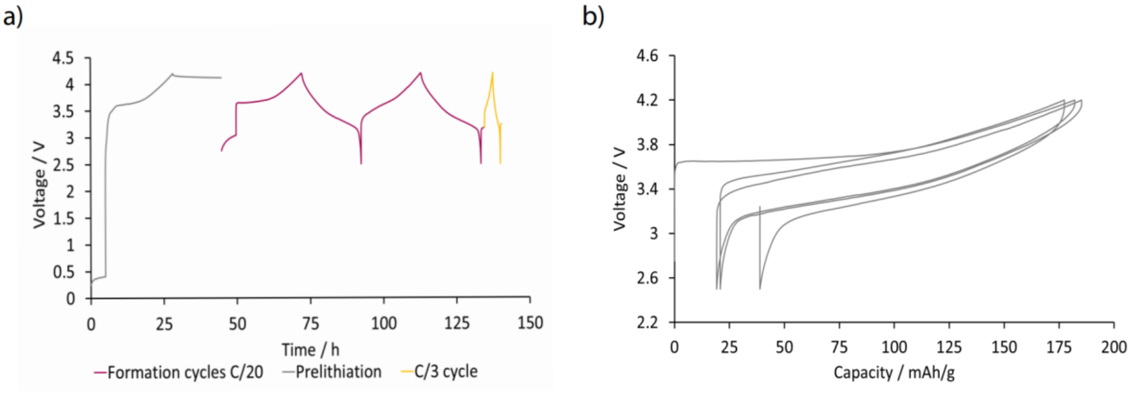

Figure 3.1: Electrochemical cycling of full cell NMC622/Si coin cell. a) Cell voltage vs. cycle time. b) Cell voltage vs. capacity mAh/g. Specific capacity is based on capacity limited material NMC622. The break between the prelithiation voltage curve and formation cycles is a result of the prelithiated silicon material being transferred into a new coin cell.

3.3.1 *Ex situ* NMR results of Silicon material lithiated to different states of charge (first C/3 cycle)

Solid state ^{7}Li MAS NMR experiments were performed on silicon anode material at different states-of-charge of the first C/3 charge and discharge cycle. Figure 3.2 a) shows the different voltages each coin cell was stopped at. Each cell at the corresponding voltages were taken apart and Figure 3.2 b) show the NMR spectrum collected. The first spectrum at the bottom of the stack plot taken at open circuit voltage (OCV) before the C/3 current was applied to the cell shows one large peak centered primarily in the phase 1 chemical shift range (0 – 10 ppm). At this point the cell is at its 'equilibrium' position, meaning the cell is stable at 3.2 V and no large changes to the Li environment within the silicon material occur. The silicon material is in a less lithiated state than at higher voltages and therefore, most of the lithium at OCV is present in the electrolyte/SEI and phase 1 which consists of isolated lithium distributed in a network of polymeric silicon clusters. The different chemical shift ranges and lithium silicide phases were identified based on literature data.[6,8–10] Halfway to the TOC at 3.7 V the spectrum clearly has two larger peaks present. The peak at 0 ppm represents the lithium present in the electrolyte/SEI, and the large peak at 20 ppm is the lithium present in phase 2. At this higher state of lithiation the silicon is broken down into star and dumbbell-shaped cluster with some isolated silicon. With this change the chemical shift moves to the 10 – 20 ppm range. There is also a smaller peak (8 ppm) in the phase 1 region of the spectrum. This peak has significantly decreased in intensity in comparison to the first spectrum collected at OCV because as the current is pushed through the cell more lithium ion migrates into the anode material, and the more highly lithiated phase is present. At the TOC (4.2 V) the spectrum is dominated primarily by the large phase 2 peak at 15 ppm. Smaller amounts of phase 1 lithium are present as the silicon material is fully lithiated at this state of charge. The phase 2 peak has also shifted over which occurs as the amount of lithium increases. The spectrum at 3.4 V after the TOC looks almost identical to the spectrum taken at 3.7 V leading up to the TOC. This suggests the phase transitions the silicon material undergoes during charge and discharge are similar. The final spectrum taken again at OCV after the C/3 cycle is completed, has one peak corresponding to phase 1 and the electrolyte/SEI like the first spectrum taken at OCV prior to the C/3 cycle. These results provide an understanding of how NMR spectrum change as a function of state of charge and confirm the different local environments present in this material.

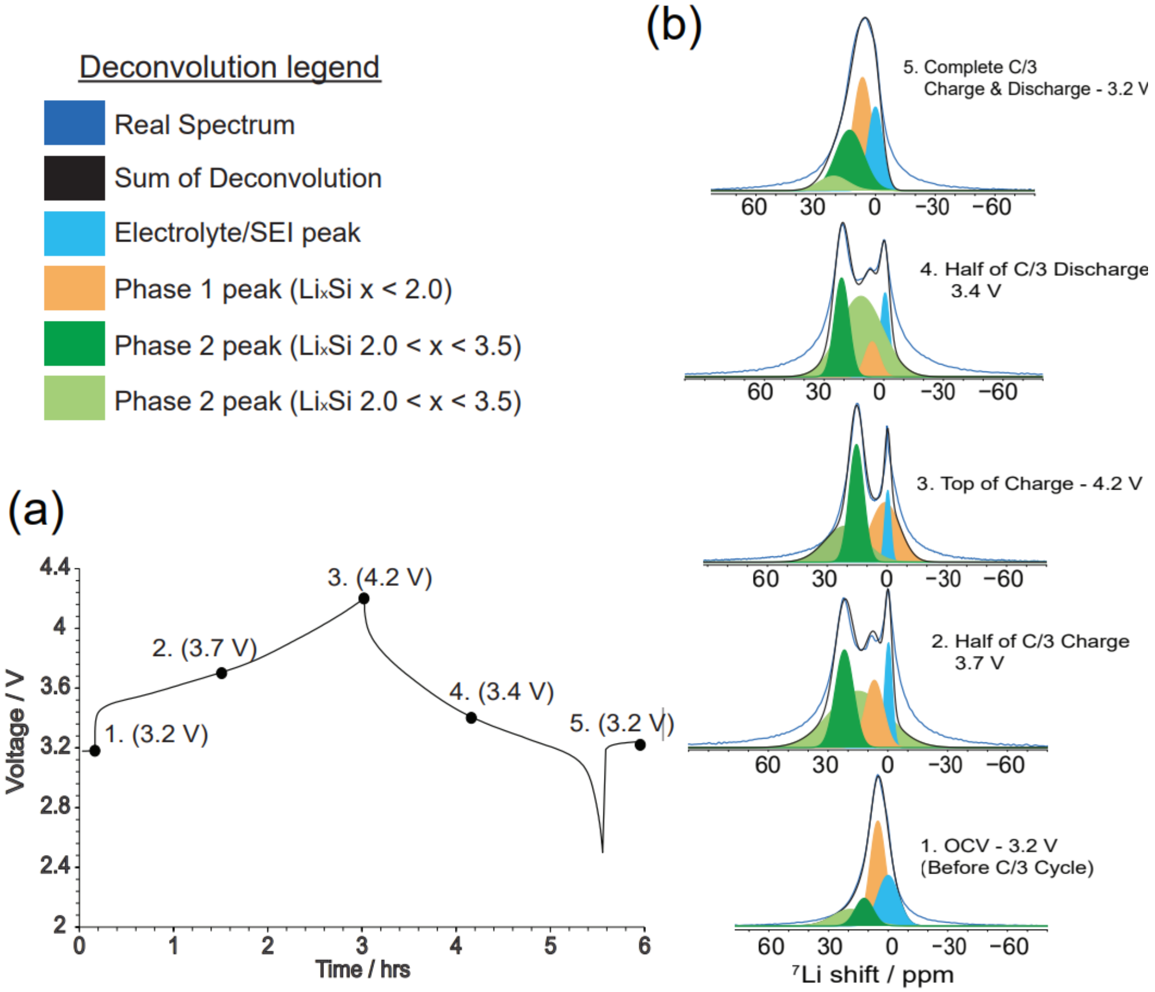

Figure 3.2: a) Electrochemical C/3 charge and discharge cycle of a full cell NMC622/Si coin cell. b) ^{7}Li Solid State NMR spectra of silicon material at different states-of-charge. Spectra deconvoluted with the program Ssnake.[18] *Deconvolution legend details what chemical environment which curve represents.*

3.3.2 Electrochemical NMC622/Si Coin Cell Results for longevity study

To examine the longevity of the silicon anode material different coin cells were cycled to different cycle counts and the change in capacity was determined. Figure 3.3 shows the capacity of coin cells cycles 10, 25, 50, 100, & 200 times. Each cell was cycled to their predetermined cycle and stopped either at the TOC or BOD. Electrochemical cycling of batteries is insufficient alone to draw conclusions about the capacity fade seen in Figure 3.3. therefore, NMR can be used as a tool to probe the local chemical environment within the silicon anode. Solid state ^{7}Li MAS NMR experiments were performed on each of the silicon anodes in the batteries. NMR results will be discussed subsequently. Table 3.2. summarizes the exact charge and discharge capacities of the coin cells, as well the capacity retention of each cell. The capacity retention is based on discharge capacity of the first C/3 cycle. Coulombic efficiency was also determined which is the ratio between discharge and charge capacity for each cycle. The capacity of each coin cell is in reference to the NMC 622 cathode material which has a specific capacity of 180 mAh/g. As seen by both Figure 3.3 and Table 3.2, even after 10 cycles there is a drop in capacity to ~80 % of the original capacity. Fluctuation in the results are present as each BOD & TOC capacities represents an individual coin cell, which have significant cell-to-cell variability. For example, it has been proven that electrode misalignment can cause significant capacity fade. This could be one potential reason why different coin cells have differing capacity retention.[23] A key explanation for the observed capacity fade in silicon anodes is the continually thickening SEI layer. The silicon anode can also pulverize during the large volume expansion/contraction upon lithium insertion and extraction, leading to capacity fade. Similarly, the formation of $Li_{15}Si_4$ at the TOC is linked with capacity fade and delamination of silicon from the current collector.

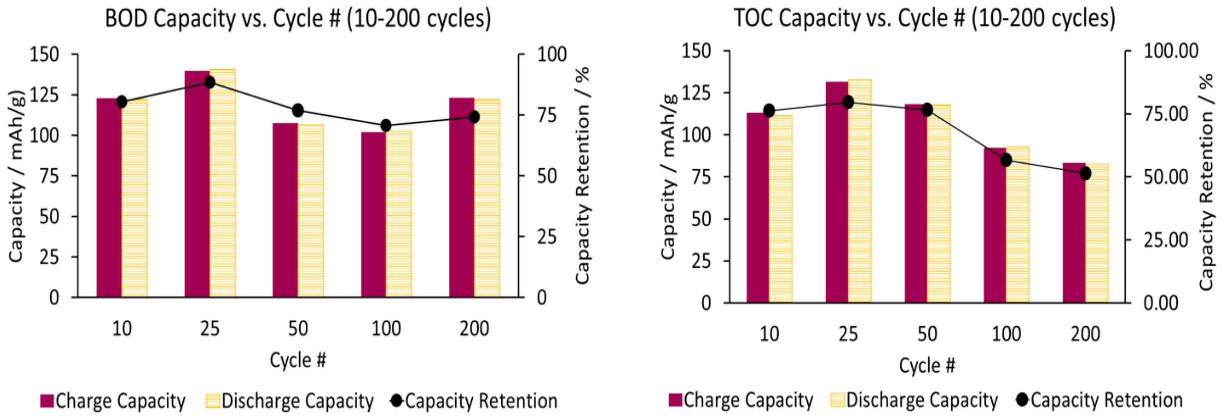

Figure 3.3: Capacities at Bottom of Discharge, left, and Top of Charge, right. Both graphs show the capacity (mhA/g) on the primary y-axis and capacity retention % on the secondary y-axis vs. cycle #. The charge and discharge capacity are represented in a bar graph format and capacity retention as a scatter plot.

Table 3.2: Capacities for coin cell stopped at cycle count 10, 25, 50, 100, and 200 at the TOC and BOD. Table details data used to graph Figure 4. Charge capacity, discharge capacity, and capacity retention. As well as coulombic efficiency of the final cycle for each cycle count.

Bottom of Discharge

Cycle #	Charge Capacity (mAh/g)	Discharge Capacity (mAh/g)	Capacity Retention (%)	Coulombic Efficiency (%)
10	123.0	122.1	80.5	99.8
25	139.7	140.8	88.4	100.8
50	107.6	106.6	76.9	99.1
100	102.0	102.6	70.6	100.5
200	123.0	122.0	74.2	99.7
		Top of Charge		
10	113.0	111.5	76.2	98.7
25	131.7	132.7	79.6	100.8
50	118.3	117.8	76.5	99.6
100	92.3	92.8	56.7	100.5
200	83.3	82.6	51.4	99.1

3.3.3 Corresponding *Ex situ* ^{7}Li MAS NMR results as a function of cycle count

Initial cycling and *ex situ* NMR results are presented in Figure 3. These spectra suggest the presence of different Li_xSi phases throughout the C/3 cycle. These results compare well to published literature.[6,8–10,13,15] In Figure 5. the same *ex situ* ^{7}Li MAS NMR described previously in this report is used to examine changes within the silicon phases as a function of cycle count. Spectra were collected after the 10th, 25th, 50th, 100th and 200th cycle at the TOC and BOD. To quantify the deconvoluted spectra seen in Figure 3.4, the relative integration under the curves found from the deconvolution are plotted in Figure 3.5. In general, the integrals indicate there is always more phase 2 at the TOC than BOD, and conversely, always more phase 1 at the BOD than the TOC. The relative integral was used to compare the integrations, as the *ex situ* characterization with multiple coin cells can lead to variability in the results. Therefore, making the integration relative to the total lithium allowed for some standardization and a better comparison between the cells.

The most notable change in the BOD stack of spectra is the increasing phase 2 peak in dark green as the cycle count increases. There is a significant change to the overall spectrum shape from cycle 25 to 50. Larger amounts of phase 2 lithium silicides are present and a second sharp peak in the range of 10 – 20 ppm can be seen in spectra 50, 100 and 200 which is not present in spectra collected at the BOD for cycle 10 and 25. Figure 3.5. a) shows the relative integration for each cycle count at the BOD for phase 1 and 2. All spectra collected after the 10th cycles have an increase in phase 2 lithium with a jump from 55 % for cycle 10 to > 70 % phase 2 for silicon anodes cycled 25, 50, 100, and 200 times. It is unexpected that at the BOD large amounts of the highly lithiated phase 2 species is present. The Li_xSi particle could delaminate from the current collected leaving them in a highly lithiated state but no longer participating in the electrochemical cycling. This so called ‘dead lithium’ would still be detected via NMR as the local chemical environment has changed regardless of if the Li_xSi particles are still participating in the electrochemical cycling.

The TOC spectra show large amounts of phase 2 present throughout all the spectra collected. Like the BOD spectra there is slightly less phase 2 lithium (74 %) present in cycle 10 versus the other longer cycle counts (< 85 % phase 2), as seen in Figure 3.5. b). All the TOC spectra in Figure 5 show two distinct peaks, with the peak corresponding to phase 2 in the 10 – 20 ppm range becoming sharper and more intense as the cycle count increases. Unlike at the BOD, it is expected to have large amounts of phase 2 present as the lithium within the cell has moved into the anode at TOC, and the silicon is in a highly lithiated form. The variability between the integration for the TOC spectra are also significantly less than at the BOD, suggesting less discrepancies with the lithiation process of the batteries versus the different chemical environments at the BOD after the delithiation. When comparing the amount of phase 2 at the TOC and BOD (Figure 3.5 c) there is always more phase 2 lithium present in the TOC spectra. And the opposite is true for phase 1 (Figure 3.5 d), greater amounts of phase 1 lithium are present in the BOD spectra. These results are as expected, however the increase of phase 2 in the BOD spectra as cycle count increases is still somewhat surprising. Each spectrum collected in Figure 3.5 is from a different coin cell cycled to the specific cycle number listed, as such there could be variability from cell to cell. Different theories could account for the excess phase 2 lithium at the BOD, but much is still unclear as to how this accumulation occurs overtime and the accuracy of these results because of the coin cell variability.

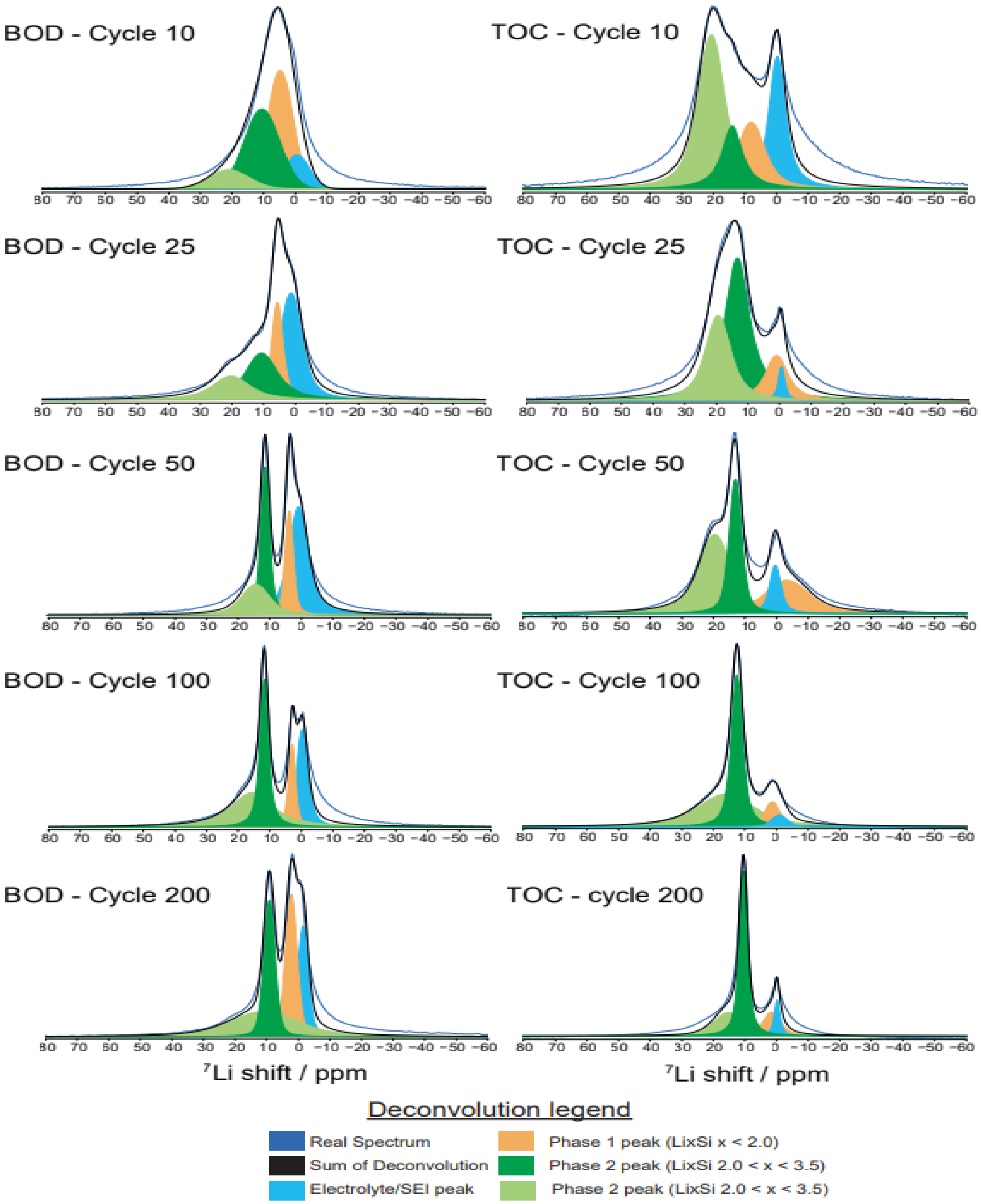

Figure 3.4: Ex situ ^{7}Li MAS NMR spectra stopped at the top of charge and bottom of discharge at cycle count 10, 25, 50, 100 and 200. Spectra deconvoluted with the program Ssnake.[18] Deconvolution legend details what chemical environment which deconvoluted peak represents.

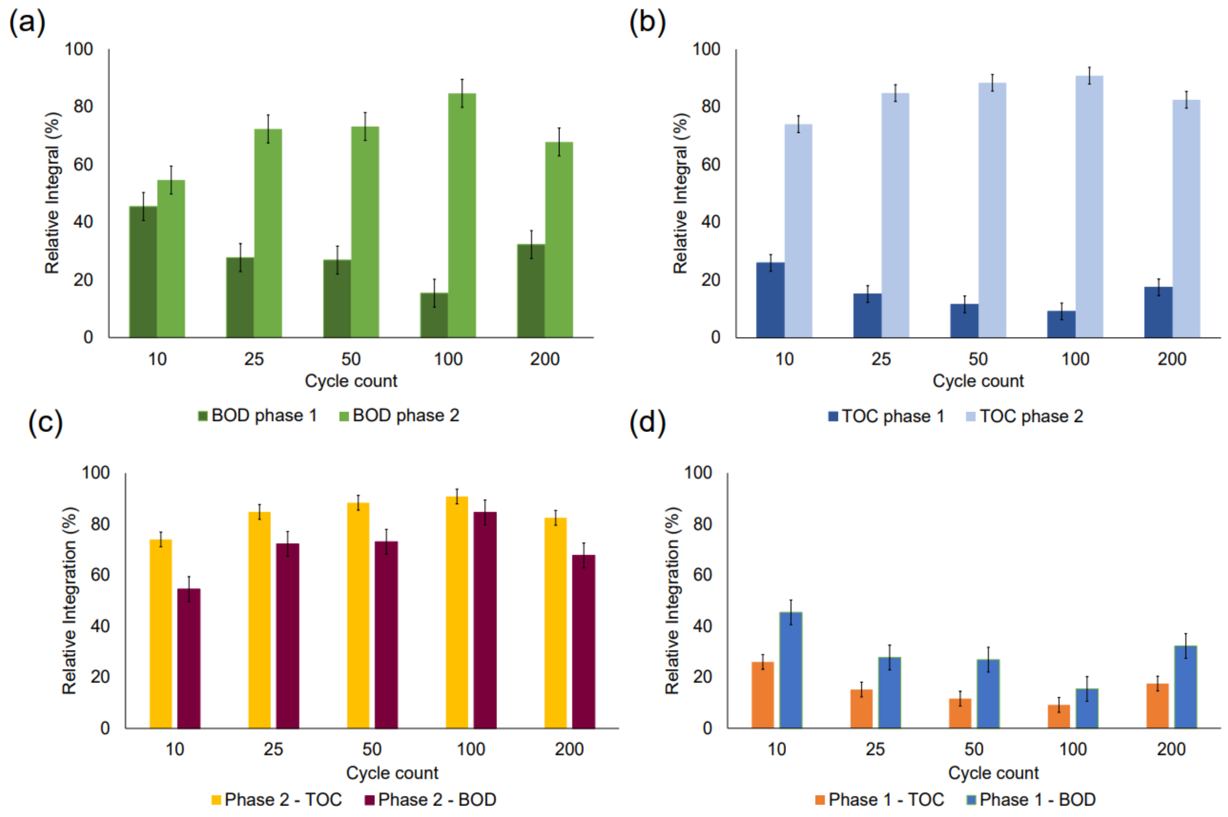

Figure 3.5: Relative integration of phase 1 and 2 peaks deconvoluted from spectra collected in Figure 5. Relative integrals exclude the electrolyte/SEI peak. The bar graph is described as followed: (a) Integration % of phase 1 & 2 in spectra at BOD, (b) integration % of phase 1 & 2 in spectra at TOC, (c) comparison of phase 2 Integration at the TOC and BOD, (d) Comparison of phase 1 integration at the TOC and BOD.

3.3.4 EXSY spectroscopy on silicon as a function of cycle count

The distinction of Li_xSi phases within silicon samples cycled to different cycle numbers were identified by their different NMR chemical shift regions. With the use of 2D EXSY experiments, the direct exchange of multiple lithium sites can be observed as cross peaks in the EXSY spectra. The rate of the exchange process is studied through the evolution of the cross-peak intensity as a function of the mixing time, τmix. Figure 6a shows the 2D spectrum for silicon collected after 100 cycles at room temperature with a mixing time of 1 ms. Like the 1D deconvoluted spectra the blue peak labeled A, was identified as the electrolyte/SEI peak. Peak B, in orange is phase 1 Li_xSi and the dark green peak represents phase 2. The off diagonal cross peaks indicate where exchange between different sites is taking place. The cross peak between BC were seen in every spectrum taken at the different mixing times for silicon cycled 50, 100 and 200 times. Increasing the mixing time results in increased cross peak intensity, reaching a saturation of the cross peaks around 10 ms. The fastest mixing time was 50 µs but at this point exchange between phases 1 and 2 are already taking place. This indicated that the exchange process present between these two regions is fast and takes place in every mixing time acquired.

Figure 3.6 b) shows a plot of relative intensity (cross peak intensity normalized to the sum of the intensities of the diagonal peaks) as a function of mixing time for cross peaks BC. The data was fit with a first-order exponential function, $f(t)=a \cdot e^{(bt)} + c$, which is shown by the trendlines in Figure 3.6 b). The exchange rates for the different cycle numbers produced by the calculated fit are shown in Table 3.3. The general trend indicates that the exchange between BC becomes slower as cycle number increases. All the exchange rates are within error of each other so significant results cannot be drawn from this data alone, but the previous ex-situ data seen in Figure 3.4 & 3.5, also suggest changes within the silicon as cycle number increases. The slower exchange between the phases supports the previously published break down mechanisms of silicon after repeated cycling. SEI buildup could be impeding the diffusion and cause the decreased exchange rate between domains of Phase 1 and Phase 2.

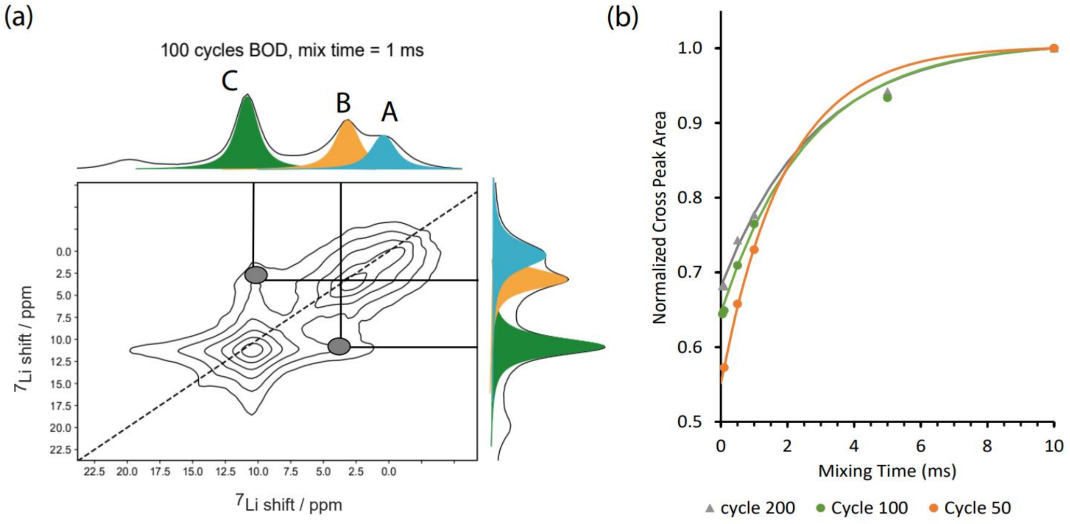

Figure 3.6: (a) ^{7}Li EXSY spectra of silicon anode material cycled 100 times to the OCV period after the BOD. Spectrum acquired at room temperature at 40 kHz with a mixing time of 1 ms. (b) normalized intensity of BC cross peaks as a function of mixing time (τmix). The first-order exponential fits are shown for cycle 200 (gray), cycle 100 (green), and cycle 50 (orange).

Table 3.3:Exchange Rates produced from first-order exponential fit for ^{7}Li EXSY NMR of Silicon at different cycle numbers.

Cycle #	**Exchange Rate (Hz)**
50	1.9 (±0.5)
100	2.6 (±0.5)
200	2.8 (±0.5)

3.3.5 SEM images of silicon as a function of cycle count

SEM images collected by Nafiseh Zaker show non-uniform particles sizes in the silicon electrode with sizes varying between ~ 0.5 µm to 2 µm. As seen in Figure 3.7, vast differences are present between the pristine material, silicon cycles 100 times and the material cycled 200 times. In Figure 3.7, I - III show clear distinct particles present, while IV - IX SEM images that have been cycled appear fuzzy and distinctions between particles are faint or no longer present. When comparing the pristine material to the material cycles 100 times obvious changes have occurred to the material. Evidence of volume expansion is present as the particles appear larger. There is also a layer of SEI present on the particles that isn't seen in the pristine material. Images VII – IX were cycled 200 times, the particles after repeated cycling now look cloudy and appear as larger blobs instead of separate particles. Material cycled 100 times showed resemblance of separate particles, none of which are present in the images collected after 200 cycles. Overall, the behavior of the particles seen in the SEM images confirm the build up of SEI and volume expansion also seen in previously published literature.[24]

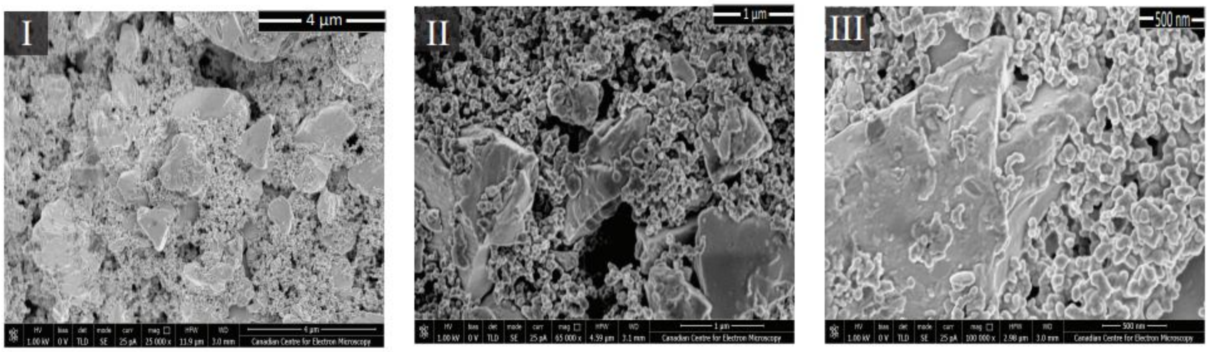

Pristine Si - 4 µm Pristine Si - 1 µm Pristine Si - 500 nm

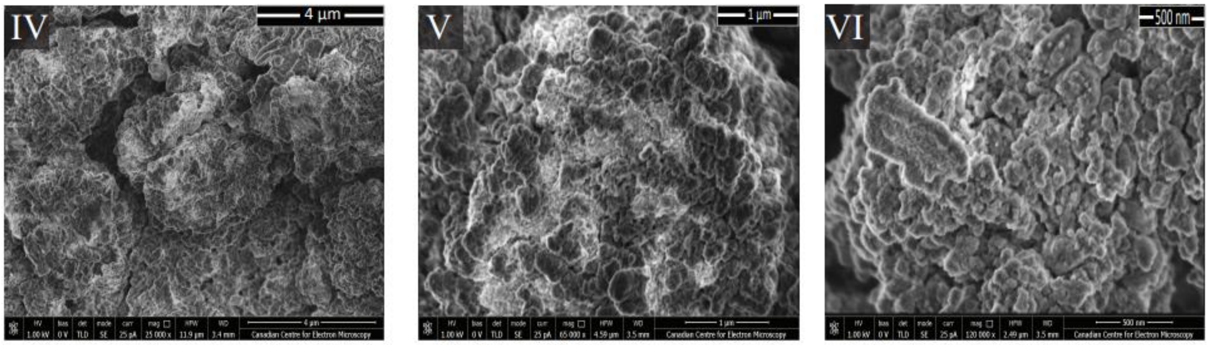

Si (C/3 100 cycles) - 4 µm Si (C/3 100 cycles) - 1 µm Si (C/3 100 cycles) - 500 nm

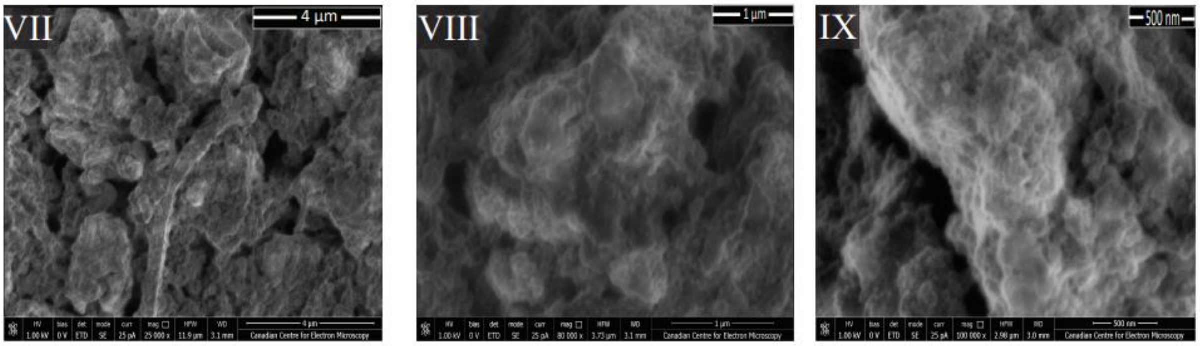

Si (C/3 200 cycles) - 4 µm Si (C/3 200 cycles) - 1 µm Si (C/3 200 cycles) - 500 nm

Figure 3.7: SEM images of silicon anode pristine (I-III), cycle 100 times at C/3 (IV-VI), and 200 time at C/3 (VII-IX). Cells were disassembled for SEM images after BOD.

The changes in electrolyte/SEI could not be tracked with NMR as most of the electrolyte was washed away with solvent prior to ex-situ NMR data collected. As such the SEM images provide insight into additional mechanism of anode breakdown not seen with NMR. The delamination seen via SEM by Obrovac et al., is not comparable to the SEM images collected for this work as a different magnification was used.[4,25] However, as previously stated the increase of phase 2 seen with ex-situ NMR suggests the highly lithiated Li_xSi phases detach from the current collector because of significant volume expansion and appear to stay in the phase 2 region present in NMR spectra as "dead lithium". Slower exchange rates calculated from the EXSY experiments also relate to both the one-dimensional ex-situ and SEM results. The increased SEI/volume expansion observed by SEM is consistent with the EXSY results which indicate slower ion exchange between phases within the electrode material.

3.4 References

(1) Kim, M.; Yang, Z.; Bloom, I. Review—The Lithiation/Delithiation Behavior of Si-Based Electrodes: A Connection between Electrochemistry and Mechanics. *J Electrochem Soc* **2021**, *168* (1), 010523. https://doi.org/10.1149/1945-7111/abd56f.

(2) Beattie, S. D.; Loveridge, M. J.; Lain, M. J.; Ferrari, S.; Polzin, B. J.; Bhagat, R.; Dashwood, R. Understanding Capacity Fade in Silicon Based Electrodes for Lithium-Ion Batteries Using Three Electrode Cells and Upper Cut-off Voltage Studies. *J Power Sources* **2016**, *302*, 426–430. https://doi.org/10.1016/j.jpowsour.2015.10.066.

(3) Jin, Y.; Zhu, B.; Lu, Z.; Liu, N.; Zhu, J. Challenges and Recent Progress in the Development of Si Anodes for Lithium-Ion Battery. *Adv Energy Mater* **2017**, *7* (23). https://doi.org/10.1002/aenm.201700715.

(4) Iaboni, D. *Li15Si4 Formation in Thin Film Si Negative Electrodes for Li-Ion Batteries*; 2015.

(5) Zhang, Q.; Xiao, X.; Zhou, W.; Cheng, Y. T.; Verbrugge, M. W. Toward High Cycle Efficiency of Silicon-Based Negative Electrodes by Designing the Solid Electrolyte Interphase. *Adv Energy Mater* **2015**, *5* (5). https://doi.org/10.1002/aenm.201401398.

(6) Michan, A. L.; Divitini, G.; Pell, A. J.; Leskes, M.; Ducati, C.; Grey, C. P. Solid Electrolyte Interphase Growth and Capacity Loss in Silicon Electrodes. *J Am Chem Soc* **2016**, *138* (25), 7918–7931. https://doi.org/10.1021/jacs.6b02882.

(7) Ma, D.; Cao, Z.; Hu, A. Si-Based Anode Materials for Li-Ion Batteries: A Mini Review. *Nano-Micro Letters*. Shanghai Jiaotong University October 1, 2014, pp 347–358. https://doi.org/10.1007/s40820-014-0008-2.

(8) Kitada, K.; Pecher, O.; Magusin, P. C. M. M.; Groh, M. F.; Weatherup, R. S.; Grey, C. P. Unraveling the Reaction Mechanisms of SiO Anodes for Li-Ion Batteries by Combining in Situ 7Li and *Ex situ* 7Li/29Si Solid-State NMR Spectroscopy. *J Am Chem Soc* **2019**, *141* (17), 7014–7027. https://doi.org/10.1021/jacs.9b01589.

(9) Key, B.; Morcrette, M.; Tarascon, J. M.; Grey, C. P. Pair Distribution Function Analysis and Solid State NMR Studies of Silicon Electrodes for Lithium Ion Batteries: Understanding the (de)Lithiation Mechanisms. *J Am Chem Soc* **2011**, *133* (3), 503–512. https://doi.org/10.1021/ja108085d.

(10) Key, B.; Bhattacharyya, R.; Morcrette, M.; Seznéc, V.; Tarascon, J. M.; Grey, C. P. Real-Time NMR Investigations of Structural Changes in Silicon Electrodes for Lithium-Ion Batteries. *J Am Chem Soc* **2009**, *131* (26), 9239–9249. https://doi.org/10.1021/ja8086278.

(11) Ogata, K.; Salager, E.; Kerr, C. J.; Fraser, A. E.; Ducati, C.; Morris, A. J.; Hofmann, S.; Grey, C. P. Revealing Lithium-Silicide Phase Transformations in Nano-Structured Silicon-Based Lithium Ion

Batteries via in Situ NMR Spectroscopy. *Nat Commun* **2014**, *5*. https://doi.org/10.1038/ncomms4217.

(12) Freytag, A. I.; Pauric, A. D.; Jiang, M.; Goward, G. R. 7Li and 29Si NMR Enabled by High-Density Cellulose-Based Electrodes in the Lithiation Process in Silicon and Silicon Monoxide Anodes. *Journal of Physical Chemistry C* **2019**, *123* (18), 11362–11368. https://doi.org/10.1021/acs.jpcc.8b11963.

(13) Song, M.; Nadimpalli, S. P. v.; Sethuraman, V. A.; Chon, M. J.; Guduru, P. R.; Wang, L.-Q. Investigation of Initial Lithiation of Silicon (100) Using Solid-State 7 Li NMR . *J Electrochem Soc* **2014**, *161* (6), A915–A919. https://doi.org/10.1149/2.033406jes.

(14) Wang, Y.; Satoh, M.; Arao, M.; Matsumoto, M.; Imai, H.; Nishihara, H. High-Energy, Long-Cycle-Life Secondary Battery with Electrochemically Pre-Doped Silicon Anode. *Sci Rep* **2020**, *10* (1), 3208. https://doi.org/10.1038/s41598-020-59913-4.

(15) Trill, J. H.; Tao, C.; Winter, M.; Passerini, S.; Eckert, H. NMR Investigations on the Lithiation and Delithiation of Nanosilicon-Based Anodes for Li-Ion Batteries. *Journal of Solid State Electrochemistry* **2011**, *15* (2), 349–356. https://doi.org/10.1007/s10008-010-1260-0.

(16) Keeler, J. *Understanding NMR Spectroscopy*.

(17) Pecher, O.; Carretero-Gonzalez, J.; Griffith, K. J.; Grey, C. P. Materials' Methods: NMR in Battery Research. *Chemistry of Materials*. American Chemical Society January 10, 2017, pp 213–242. https://doi.org/10.1021/acs.chemmater.6b03183.

(18) van Meerten, S. G. J.; Franssen, W. M. J.; Kentgens, A. P. M. SsNake: A Cross-Platform Open-Source NMR Data Processing and Fitting Application. *Journal of Magnetic Resonance* **2019**, *301*, 56–66. https://doi.org/10.1016/j.jmr.2019.02.006.

(19) Berhaut, C. L.; Dominguez, D. Z.; Tomasi, D.; Vincens, C.; Haon, C.; Reynier, Y.; Porcher, W.; Boudet, N.; Blanc, N.; Chahine, G. A.; Tardif, S.; Pouget, S.; Lyonnard, S. Prelithiation of Silicon/Graphite Composite Anodes: Benefits and Mechanisms for Long-Lasting Li-Ion Batteries. *Energy Storage Mater* **2020**, *29*, 190–197. https://doi.org/10.1016/j.ensm.2020.04.008.

(20) An, S. J.; Li, J.; Daniel, C.; Mohanty, D.; Nagpure, S.; Wood, D. L. The State of Understanding of the Lithium-Ion-Battery Graphite Solid Electrolyte Interphase (SEI) and Its Relationship to Formation Cycling. *Carbon*. Elsevier Ltd August 1, 2016, pp 52–76. https://doi.org/10.1016/j.carbon.2016.04.008.

(21) Gauthier, M.; Carney, T. J.; Grimaud, A.; Giordano, L.; Pour, N.; Chang, H. H.; Fenning, D. P.; Lux, S. F.; Paschos, O.; Bauer, C.; Maglia, F.; Lupart, S.; Lamp, P.; Shao-Horn, Y. Electrode-Electrolyte Interface in Li-Ion Batteries: Current Understanding and New Insights. *Journal of Physical Chemistry Letters*. American Chemical Society November 19, 2015, pp 4653–4672. https://doi.org/10.1021/acs.jpclett.5b01727.

(22) Kim, H. J.; Choi, S.; Lee, S. J.; Seo, M. W.; Lee, J. G.; Deniz, E.; Lee, Y. J.; Kim, E. K.; Choi, J. W. Controlled Prelithiation of Silicon Monoxide for High Performance Lithium-Ion Rechargeable Full Cells. *Nano Lett* **2016**, *16* (1), 282–288. https://doi.org/10.1021/acs.nanolett.5b03776.

(23) Murray, V.; Hall, D. S.; Dahn, J. R. A Guide to Full Coin Cell Making for Academic Researchers. *J Electrochem Soc* **2019**, *166* (2), A329–A333. https://doi.org/10.1149/2.1171902jes.

(24) Taiwo, O. O.; Loveridge, M.; Beattie, S. D.; Finegan, D. P.; Bhagat, R.; Brett, D. J. L.; Shearing, P. R. Investigation of Cycling-Induced Microstructural Degradation in Silicon-Based Electrodes in Lithium-Ion Batteries Using X-Ray Nanotomography. *Electrochim Acta* **2017**, *253*, 85–92. https://doi.org/10.1016/j.electacta.2017.08.161.

(25) Iaboni, D. S. M.; Obrovac, M. N. Li 15 Si 4 Formation in Silicon Thin Film Negative Electrodes . *J Electrochem Soc* **2016**, *163* (2), A255–A261. https://doi.org/10.1149/2.0551602jes.

Chapter 4

In *Operando* NMR Study of silicon Anode Material

Data collection and analysis were performed by Amanda A. Ciezki. Kevin J. Sanders assisted in the collection of nuclear magnetic resonance (NMR) data and Breanna Pinto helped assemble the reusable single-layer cartridge cell*. Three electrode cell measurement were collected by Brian Koch. NMR measurements were performed at McMaster University and the three-electrode cell experiment was acquired at General Motors research and development facilities in Warren Michigan.*

4.1 Introduction

Nuclear magnetic resonance (NMR) has proven useful as a tool to study battery material because many of the NMR active nuclei are found in different parts of the electrochemical cell, i.e., anode, cathode and/or electrolyte. Using this powerful technique insight can be gained into short-range local structures of the battery material under investigation. Historical *ex situ* NMR methods were heavily utilized to probe structural characteristic, nuclear dynamics, and chemical exchange within solids.[1–7] Currently in situ and *operando* NMR are of considerable interest because the experiment can monitor structural and electronic changes while electrochemical cycling occurs allows for high chemical specificity of both crystalline and amorphous phases and minimized any self-relaxations processes that could be missed with *ex situ* NMR.[8] With in situ and *operando* NMR the time-resolved dimension is used to study the evolution of dynamics and/or metastable phases within electrochemical cells; however there is a loss of resolution as this technique is a static experiment.[9,10] Despite its downfall with resolution, *operando*/in situ NMR are a valuable tool for both the NMR and battery communities. The distinction between in situ and *operando* NMR depends on whether data collection is done during electrochemical cycling (*operando)* or if data is collected without disassembling the cell (in situ) and the battery components stay in their position.[8] Prior studies have utilized *operando* NMR to understand silicon anode structural characteristic in a half-cell (i.e., Li metal is the counter electrode) and no studies to the authors knowledge have been published using a *operando* NMR on a full battery with silicon as the anode.[7,11]

The experimental design of Krachkovskiy et al.[10] and Sanders et al.[9] perform *operando* measurements on a full graphite/NMC cell to study the effects of lithium plating. Krachkovskiy et al.[10] is the precursor to Sanders et al.[9] reusable single-layer cartridge cell which is also employed in this chapter. A parallel-plate resonators was chosen as part of the probe setup to produce a uniform magnetic field and therefore enables uniform excitation and detection over the entire sample. The Balcom group established the use of parallel-plate resonators for the study of energy storage devices like fuel cells and LIBs.[12–14] The cartridge cell design itself is further enhanced versus previous designs with better seal, easy assembly, and uniform pressure distribution. The previous studies showed the onset of lithium plating and the accumulation of lithium metal during fast charging when pairing a graphite anode with NMC 622. Adequate sensitivity was used to sequential collect NMR spectra with enough time resolution to capture changes in the dynamics of graphite during fast charging.[9]

In this chapter the goal was to explore the dynamic and structural changes of Li_xSi phases with multiple different cycling conditions. Cycling parameters like that seen in Chapter 3 for the ex-situ NMR studies were applied to compare results between the different methodologies. Fast charging cycles were also employed to see if lithium metal plated on the anode surface of silicon similar to than seen in graphite.

4.2 Experimental

A parallel-plate resonator RF probe with two plates (7.0 mm separation, 50 mm long and 20 mm wide) was used to achieve a uniform field over the entire sample volume, Figure 4.1 (a). The reusable cartridge cell container, designed to fit within the ^{7}Li parallel-plate resonator was made from virgin polyether ether ketone (PEEK). The O-ring which was used to seal the cell after compression was applied, was made from ethylene propylene diene monomer rubber (EPDM). Charge was delivered to the current collector plates via lead wires fed through a hole placed in each of the two halves of the cartridge. Thin aluminum (for cathode) and copper (for anode) wires were used to carry the electric current to and from 400 µm thick plates made of the same metal. Each current collector was made from the same metal as the respective electrode and provided a rigid platform for uniform pressure over the entire area of the electrodes. Pictures and computer drawings of the cell can be seen in Figure 4.1 (b) and (c).

The cartridge cell was prepared with the same material as that of the coin cells for ex-situ NMR. $LiNi_{0.6}Mn_{0.2}Co_{0.2}O_2$ (NMC622, General Motors, 28.86 mg/cm^2, 4.5 mA h/cm^2) as cathode, and silicon (General Motors, 2.7 mg/cm^2, 9 mA h/cm^2) as the anode were cut to exact dimensions with a scalpel. The NMC622 electrode was cut to 1.9 cm x 3 cm (5.7 cm^2) and the silicon anode was cut to 2 cm x 3.1 cm (6.2 cm^2). All cell components except the Celgard 2325 separator were dried for 24 hours at 80 °C under vacuum to remove any water or volatile solvents before cell cartridge components, electrodes, and separators were brought into an Ar-filled glovebox (M Braun, <3 ppm H_20, <3 ppm O_2). The Cu current collector plate and silicon anode was placed in the cartridge cell base, followed by 200 µL of electrolyte solution (1 M lithium hexafluorophosphate in fluorinated ethylene carbonate/ethyl methyl carbonate 1:4 wt% ($LiPF_6$ FEC/EMC 1:4 wt%)). Two separators were then placed on top of the silicon anode followed by the NMC622 cathode. Lastly the Al current collector plate was placed on top, and the cartridge top was carefully aligned. Eight brace screws were gradually tightened in an alternating order to apply uniform pressure throughout the cell and compressed the O-right to create a secure seal. The cell sat for 5 h before any current was applied to ensure a uniform electrode and separator wetting.

Experiments were carried out using a Bruker Avance III HD wide-bore instrument at 7.05 T with a nominal ^{7}Li frequency of 116.7 MHz. ^{7}Li chemical shifts were references to the electrolyte peak within the sample at 0 ppm. The parallel plate RF resonator (section 2.4.1) was connected to a Bruker MicWB40 probe with a Micro 2.5 gradient system. Homemade low-pass filters were used to shield the RF probe from high frequency noise arising from the charging leads. All NMR experiments utilized a pulse-acquisition sequence with a pulse tip angle of 13 and a recycle delay of 50 ms. Each spectrum of the *operando* experiment performed at different electrochemical cycling rate were acquired with a different number of scans with a different total data collection time, see Table 4.1 for details pertaining to the specific time per 1D slide and number of scans. One hundred and sixty-four one dimensional pulse acquire spectra were collected every 15 mins during the *operando* NMR experiment while the cell of cycled. The NMR intensity and the time derivative of *operando* spectra (dOp) were plotted using RMN (PhySy Ltd., Grandview Heights, OH) software package, while 1D spectral deconvolutions were performed using Gaussian and Lorentzian line fitting to model the different Li_xSi resonances within the spectra, using SsNake.[15]

Table 4.1: Experimental parameters for operando NMR conditional to C-rate.

C- rate	*Time per pulse-acquire experiment (mins)*	*Number of scans*
3C & 2C	1.5	876
1C & C/2	3	1748
C/3	5	2912
C/20	15	8738

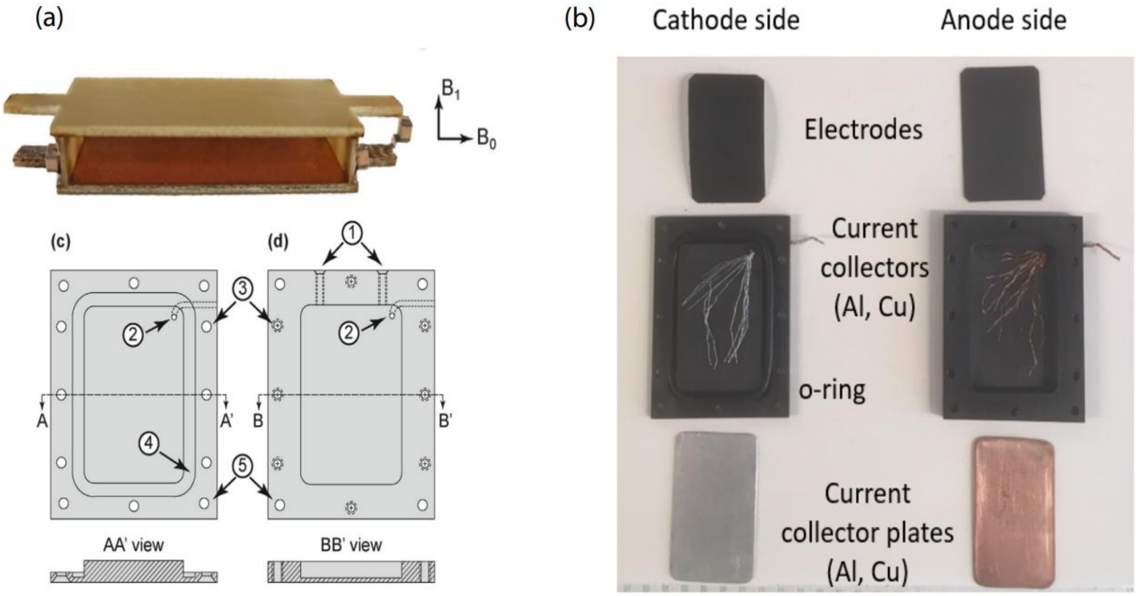

Figure 4.1: (a) Photograph of the parallel-plate resonator. (b) Photograph of cartridge cell disassembled and labelled in picture. Computer drawings of the (c) top and (d) bottom flanges of the cartridge used for battery assembly, showing a top view and a center plane cross section. Legend: 1 ¼ threaded 1.2 mm diameter holes for electrolyte solution filling; 2 ¼ holes for wire leads; 3 ¼ eight clearance (in c) and threaded (in d) holes for the M2 screws, used for closing the cartridge; 4 ¼ groove for O-ring used for sealing the cartridge; 5 ¼ four alignment holes at the corners of the two flanges, to assist the cell alignment within the RF probe. Reprinted with permission from carbon 189, 2022, 377 – 385[9]. Copyright © 2022, Carbon.

4.3 Results and Discussion

To further investigate the different Li_xSi phases within the silicon material *operando* ^{7}Li NMR was collected on a cartridge cell with the same silicon material studied via *ex situ* NMR in chapter 3. By combining the high sensitivity provided by the cartridge cell and parallel-plate resonator probe, excellent discernment of changing speciation can be achieved with *operando* NMR experiments. First, we demonstrate this with a slow charging-discharge cycle of C/20, which give both sensitivity and speciation information, this is followed by multiple cycles performed at C/3. This is related to the *ex-situ* analysis presented in Chapter 3 but performed on one battery instead of multiple coin cells. Fast charging rates of C/2, 1C, 2C and 3C were employed on an additional cartridge cell to monitor the chemical environment changes of lithium within the silicon anode at faster rates. A derivative *operando* analysis also revealed key changes in the behavior of lithium species in battery cells, as a function of cycling rate and cycle count.

The cell was first cycled at a current corresponding to C-rate of C/20 (1.28 mA) between voltage limits of 2.5 V and 4.2 V on an Arbin BT2000 battery cycler as a formation cycle for the silicon anode, followed by another *operando* C/20 with the same electrochemical parameters. Figure 4.2 shows the voltage vs. capacity curves for both cycles. There is a 21% capacity loss between the 1st C/20 cycle and the *operando* cycle, which is not unexpected as some capacity loss in the first cycles is common for silicon anodes as the SEI layer is formed.

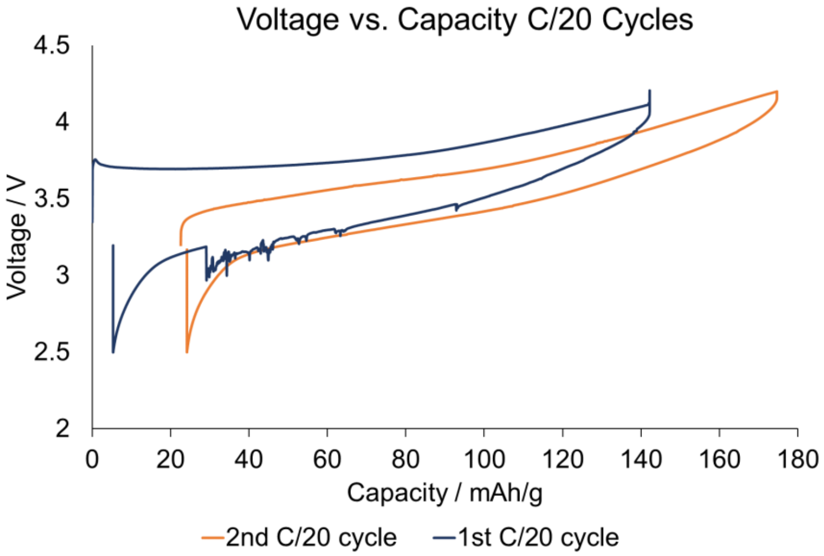

Figure 4.2: voltage vs. capacity of C/20 formation cycles. The first C/20 cycle was preformed on the Abrin, and the second cycle was preformed operando.

To see the changes within the local chemical environment during the experiment an intensity and derivative of the *operando* NMR spectra were chosen as the best processing approach. Figure 4.3 a) shows voltage vs. time plot and corresponding intensity-contour plot collected at the same time in Figure 4.3 b). At the start of charge there is clearly only one peak with large intensity surrounding 0 ppm. This is likely the electrolyte/SEI peak and little to none of the highly lithiated species are present. As the battery approaches its full state of charge the plot displays intensity in the darker blue and pink colors in the phase 1 and 2 regions of the spectrum, with the most intense peak seen at the TOC at 14 – 11 ppm. As the different lithium silicide phases start to form there are clear indications of phase 2 lithium present about 12 hours into the C/20 charge. Surprisingly at the TOC the peak that was once outstretched to 20 ppm has shifted to lower chemical shifts, leading to the greater intensity in the lower phase 2 range of 10 – 20 ppm. *Ex situ* NMR was unable to detect this subtle shift as spectrum at higher cycle counts were only acquired at the TOC and BOD. Visualizing this shift in the *operando* NMR data is consistent with what was observed by the Grey group in their study of a half-cell with silicon anode material.[11] As the lithium concentration continues to increase, the phase 2 peak shifts to lower chemical shift values within its 10 – 20 ppm range that can overlap with the phase 1 peak. When the current is reversed and the cell begins discharging and lithium is removed from the anode, the phase 2 peak shifts to higher chemical shifts, indicating phase 2 lithium is still present but in a lower lithiated state, Li_xSi, $x < 3$. Eventually the phase 2 peak is no longer present and only intensity surrounding the electrolyte/SEI peak is left at the BOD. Little to no lithium silicides are observed at this point. Because of the shifting phase 2 peak the general shape of the intensity plot appears to be an oblong horizontal heart, which indicates symmetrical charge and discharge of the silicon material.

Figure 4.3 c), shows the derivative *operando* (dOp) spectrum. This technique, introduced recently by Lorie Lopez et al.[16] applies a time derivative to the NMR intensity as part of the NMR processing step and yields a derivative plot. The benefits of the processing step are the removal of resonances with constant intensity. (e.g., the electrolyte, SEI, or baseline artefacts). Moreover, the resolution is improved between nearby resonances, specifically at the TOC and beginning of the discharge. The most striking feature of Figure 4.3 c) is the rapid loss of lithium (chemical shift range of 18 – 23 ppm) as the battery reaches the TOC, seen by the change of red to blue within this region. The reverse also appears at the beginning of discharge with a gain of lithium at about 20 ppm, before an overall loss of lithium for the remainder of discharge. Using the dOp analysis not only emphasizes the changes in the local environment of the lithium nuclei but also reveals subtle changes that could be missed with only a contour plot.

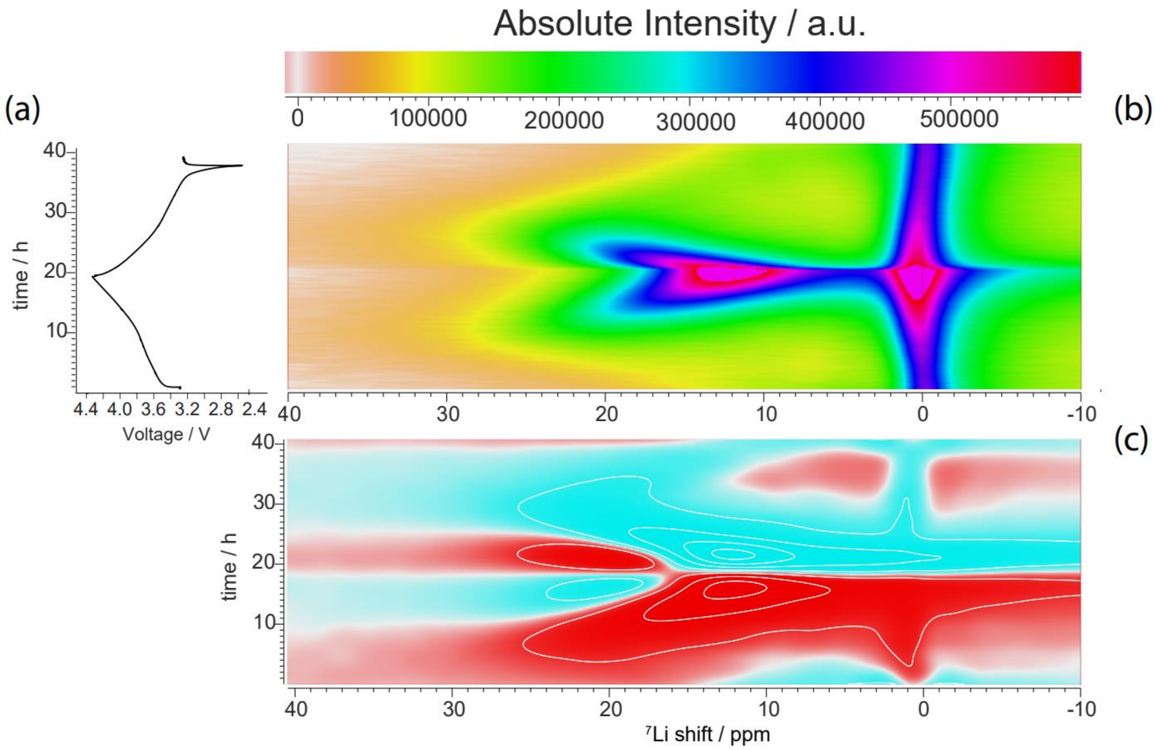

Figure 4.3*: (a) the voltage profile during charging and discharging at C/20 (b) Intensity plot of operando NMR spectra collected during the cycle shown in (a) Most intense contour in pink, followed by dark blue, light blue, green and yellow. (c) Derivative (dOp) of operando NMR spectra shown in (b), with red representing a positive change and blue a negative change in the plot.*

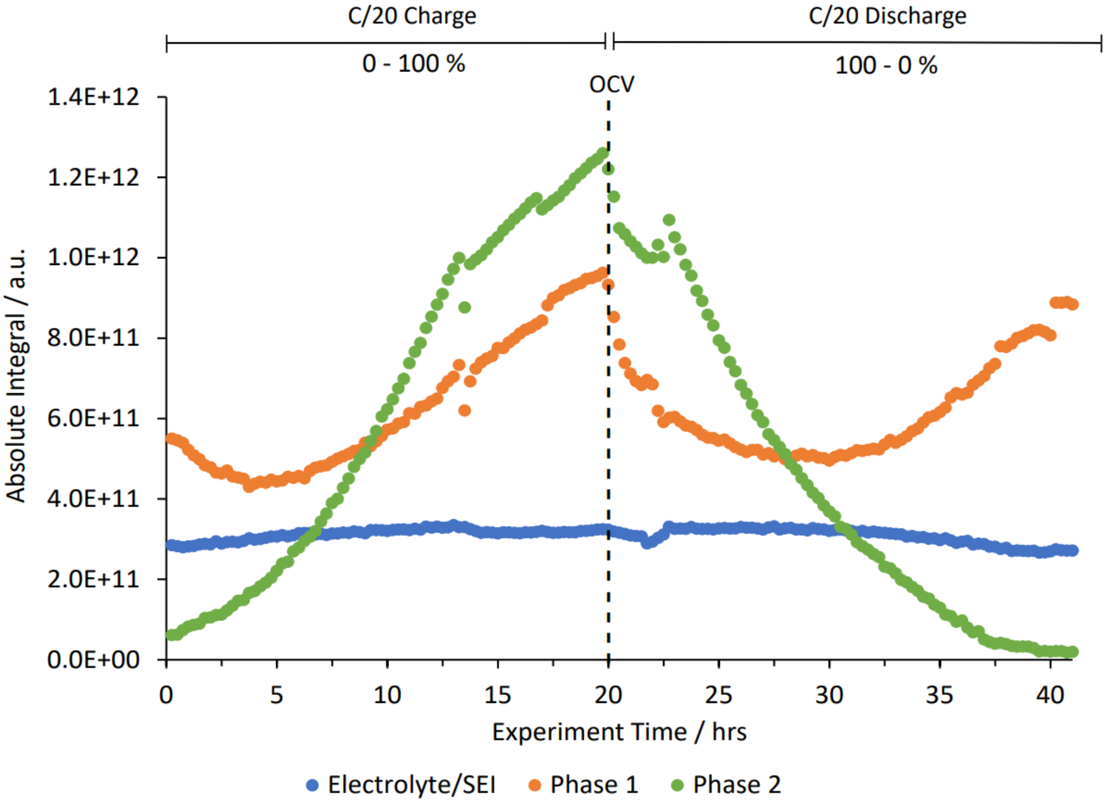

Figure 4.4: Relative integral vs. time of 2D operando C/20 experiment. 164 one pulse NMR spectra were collected every 15 min during the cycle. Using Ssnake and a multi-fit tool developed in the Goward group each spectrum was fit sequentially and the intensities are plotted as a function of 1D NMR slices.

To further analyze how the intensities of the *operando* NMR spectrum changing over time, each one-pulse NMR experiment compiling the intensity plot seen in figure 4.3 a), was extracted and integrated using a multi-fit deconvolution tool developed in the Goward group. There was a total of 164 one pulse NMR spectra collected every 15 min to acquire the full C/20 cycle. Figure 4.4. shows the relative integral of the electrolyte/SEI, phase 1, and phase 2 peaks over the experiment time. It is clear at the beginning of charge there is more phase 1 present, with very little phase 2 lithium seen. As the battery approaches TOC, the phase 2 lithium peak grows as evident by the increased integration. The increase in the highly lithiated states results in a decrease of phase 1. After the 15 min OCV period both phase 1 & 2 Li_xSi peaks decrease in intensity.

The decrease is not completely linear likely due to the different phases rearranging with the negative current applied during discharge. Almost half through the discharge (~ hour 37 of the experiment), the amount of phase 2 lithium is less than phase 1 and at this point the phase 1 peak appears to be constant. This switch from greater phase 2 to larger amount of phase 1 as the cell approaches BOD is consistent with what was seen in Figure 4.3. The integral trends themselves are relatively symmetrical between charge and discharge, evidence of this symmetry was also seen in the intensity and dOp plots. The shift changes as a function of charge density were also detected with ex-situ NMR as seen in the previous chapter. The electrolyte/SEI peak is comparatively constant throughout the experiment with only subtle changes. The integration and the phase 1, 2 and electrolyte/SEI peak were not held constant at the multi-fit program in ssNake was run. The linewidth of all the peaks were fixed and only the phase 1 & 2 peaks were free to move in chemical shift value to account for the moving peak depending on the degree of lithiation. Overall, the integration of the deconvoluted spectra over the C/20 cycle allows for the qualitative changes present in the contour plot and dOp spectra to be quantified.

Subsequent to the C/20 test at modest charging rates the cell was charge at a C/3 (8.28 mA, current) to a cut-off voltage of 4.2 V, with a 15 min OCV period, followed by a discharge to 2.5 V at the same current. Figure 4.5 (a) shows the voltage vs. capacity for all 50 C/3 cycles performed *operando.* Cycle 1 – 30 and cycle 31 – 50 were acquired using the same parameters but two different experiments. The capacity curves provide overall consistent results with the final capacity retention of 61%.

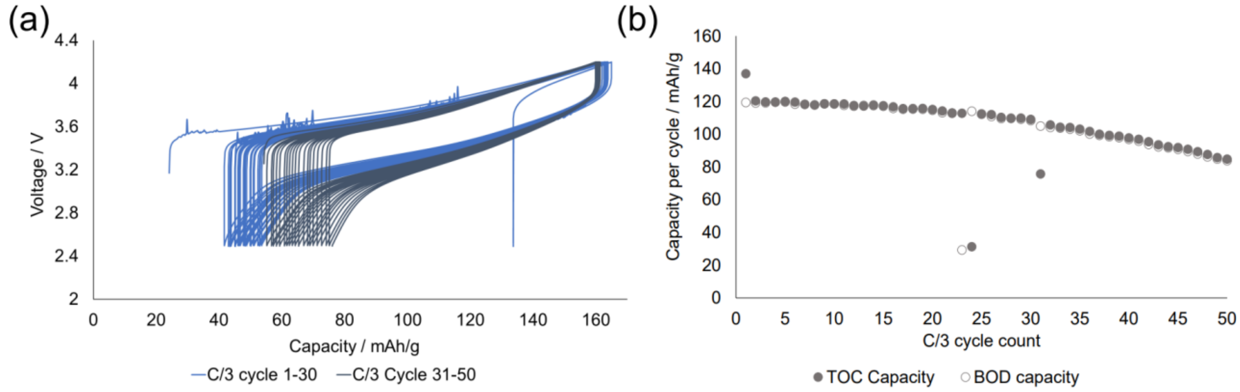

Figure 4.5: (a) voltage vs. Capacity for 50 C/3 cycles. (b) capacity pre cycle vs. cycle count. Cycle 1 – 30 and cycle 31 – 50 were acquired using the same parameters but two different experiments.

One-pulse NMR spectra were collected every 5 min during the duration of the C/3 cycle. Relevant information on cycle 1, 10, 25 and 50 are shown in Figure 4.6. The voltage curve, intensity contour plots, and dOp spectrum for each of the selected cycles are present, from left to right in Figure 4.6. The NMR spectra looks similar to that of the C/20 cycle in Figure 4.3, with a symmetric charge and discharge cycle forming the oblong heart shape in the intensity plot. Interestingly for cycle 10 and 25 the intensity of the peaks in the 15 – 13 ppm range at the TOC aren't as strong as that in cycle 1, and the heart shape is less pronounced. Cycle 50 completely lost the original shape seen in the contour plots and instead an extremely intense peak in the chemical shift range of 16 – 11 ppm is present. The dOp spectra for all the C/3 cycles differ at the TOC and start of discharge in comparison to the C/20 cycle, Figure 4.3 c). The obvious shift in the phase 2 peak moving from higher to lower chemical shift (red to blue in the dOp) at the TOC and vice versa during the start of discharge (blue to red – dOp) is not as prevalent in the C/3 cycles. This perhaps is because the C-rate is significantly higher for the C/3 cycle and the lithium may not have time to rearrange into the same ordered local phases. Regardless there is still a similar shape in the dOp and the contours to indicate a similar trend as seen for the slower c-rate in cycle 1, 10 and 25. Cycle 50 does not have the same characteristics and instead of the contours indicating a shift in the phase 2 region, there is only significant intensity in the same 16 – 11 ppm range identified by the intensity contour plot. Changes in the lithium environments of silicon are obviously occurring as the cycle count increases.

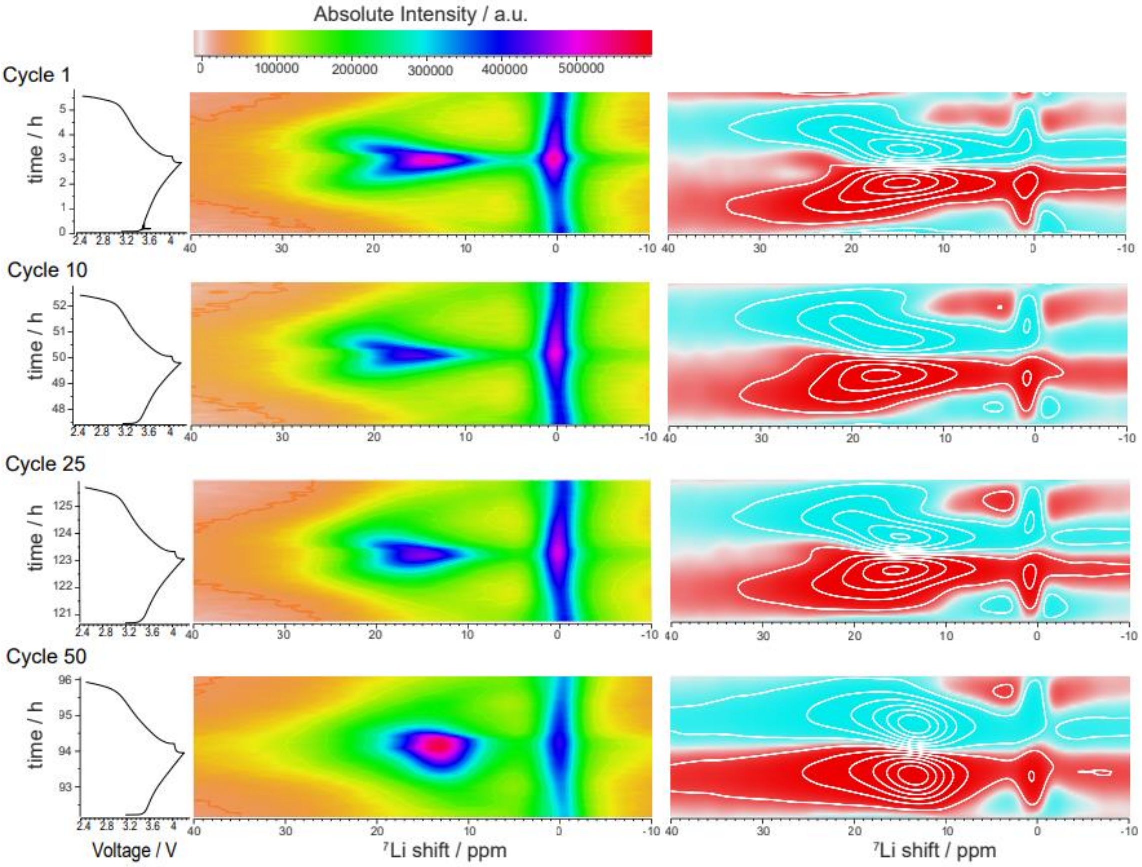

Figure 4.6: voltage, intensity contour plots, and derivative (dOp) of operando NMR spectra for C/3 cycle 1, 10, 25 & 50.

Determining the integration for the electrolyte/SEI, phase 1 & 2 peaks from each of the corresponding cycles analyzed in Figure 4.6 allowed for the trend seen to be quantified. Figure 4.7 shows the absolute integral vs. experiment time for C/3 cycle 1, 10, 25, & 50. A 15 min OCV period was collected after the TOC at 4.2 V and is represented by the dotted lines and gray area in Figure 4.7. Each cycle used the same 8.28 mA of current of complete the C/3 cycle. The calculated current for a 3-hour charge/discharge was determined based on the discharge capacity of the 2nd C/20 cycle as it provides a more accurate value than basing the c-rate on the theoretical capacity, which assumes no capacity has been lost. As the cell is continuously cycled it losses capacity and as such the same current used for the 1st C/3 cycle, cycles the cell at a faster rate than 3 hours for the 50th cycle, for example because the overall cell capacity has decrease. This is evident when comparing the experiment time from a-d in Figure 4.7. All cycles show a constant electrolyte/SEI peak ~$1.0e^{11}$ in intensity, there is also a consistency with the increase in phase 2 in a somewhat linear fashion for all the cycles. For cycle 1, 10 and 25 the greatest intensity of the phase 2 peak is seen right before the OVC at TOC or during the OCV period when is cell is still in an extremely lithiated state. This trend is consistent with the absolute integral seen for the C/20 cycle (Figure 4.5), and the intensity and dOp plot seen in Figure 4.6. Both the integral and dOp plot show phase 2 growing as the cell charges and a loss of lithium at the cell discharges. Interestingly, this same trend is not observed for the phase 2 integral in cycle 50. The maximum intensity is reached after the OCV while the discharge current is already applied. Although different from earlier cycles this increased integration of phase 2 is also seen in the intensity plot as the dark pink/red persists in the 16 – 11 ppm range not present in other cycles, Figure 4.6. As a result of the numerous cycles the SEI has grown substantially around the silicon particles; this could be impeding the lithium diffusion and the alloying mechanism used to form and break the Li_xSi bonds. The excess lithium intensity in phase 2 could also correspond to the delaminated lithium no longer present in the electrochemical cycling of the cell but still detected via NMR. There is also a strong more pronounced dip in the phase 1 integral for the 50th cycle versus the phase 1 intensity seen for cycle 1, 10 and 25. A slight decrease is seen for phase 1 in prior cycles after the OCV, but the phase 1 integral in cycle 50 almost decreases to zero. This trend suggests more silicon is (possibly trapped) in a highly lithiated state in cycle 50. Similar trends regarding the increase in phase 2 after several cycles were observed in Chapter 3 with ex-situ NMR but the exact real time differences and trends of the phases change the cycles could not be observed.

A notable different between the C/20 absolute integration and the C/3 integration is how the phase 1 peak changes over each cycle. As discussed previously, at the c-rate of C/20 both the phases 1 and 2 show an increase/decrease as positive or negative current is applied, the difference being in the rate of change between the phases. The phase 2 peak is behaving as seen in the C/20 data, but the phase 1 integral barely changes during the C/3 cycle which differs from the C/20 integration. This change in the integration trends between the faster and slower c-rates suggests that at slower c-rates with less current the alloying mechanism occurs sequentially, so kinetically both the formation of phase 1 and phase 2 Li_xSi are favoured. When increasing to a faster rate phase 2 lithium is favoured meaning there is no longer large polymeric Si clusters forming with only small amounts of lithium ions. Instead, lithium ions surround small clusters and isolated silicon atoms, which is seen by the dramatic increase of phase 2 lithium in the NMR. The trends present in both data sets are the same, regardless of a 20-hour symmetrical cycle or 3-hour symmetrical cycle. Greater amounts of the less lithiated phase 1 are still present at the start of charge and end of discharge, while the more highly lithiated species are dominant at the TOC. However, the amount of phase 2 and its changes over the cycle are substantially different with the changes C-rate.

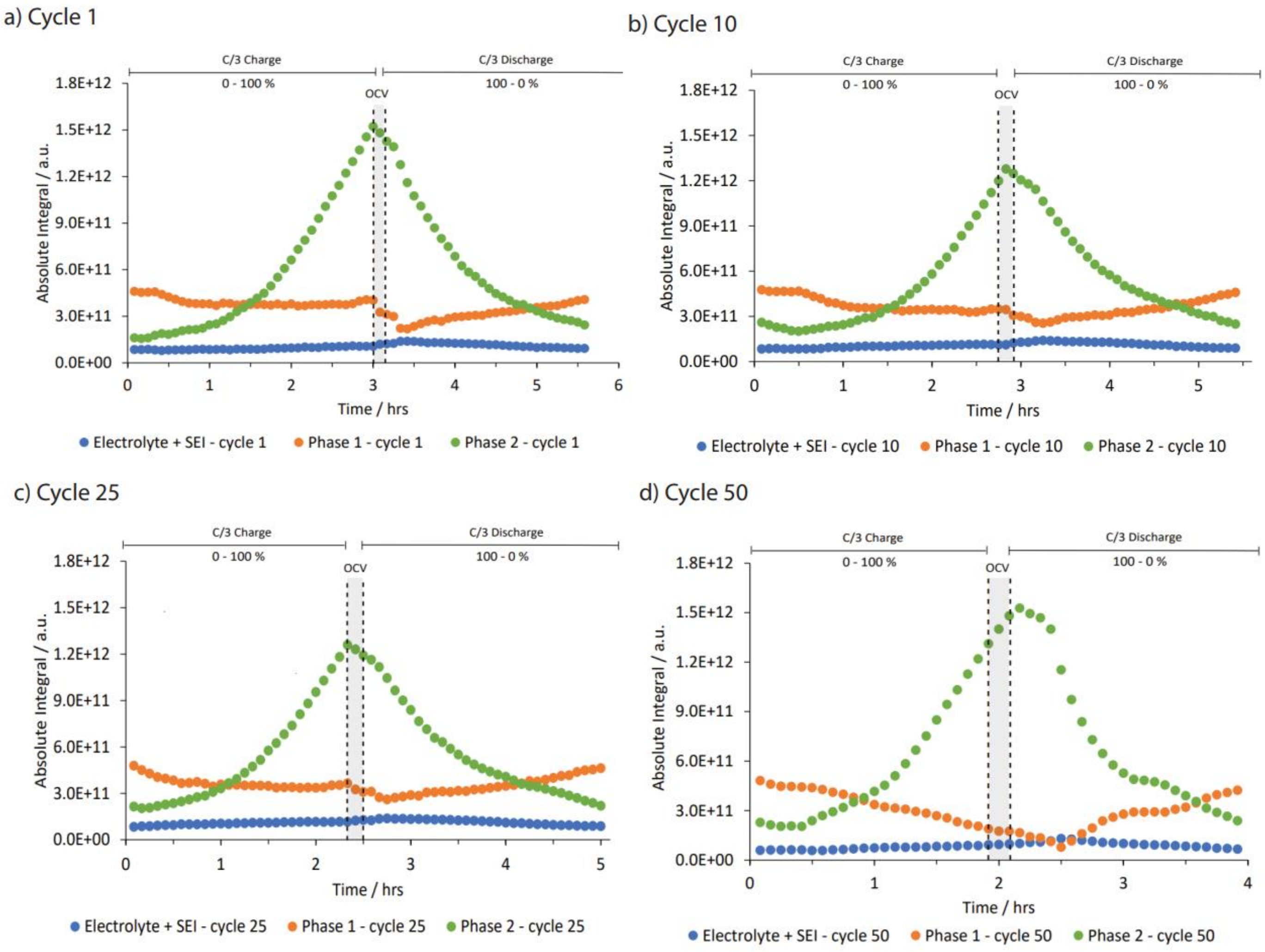

Figure 4.7: Absolute integral vs. time of 2D operando C/3 experiment. NMR spectra were collected every 5 min during the cycle, a 15 min OCV period was included between the TOC and beginning of discharge. a) 1st C/3 cycle, b) 10th C/3 cycle, c) 25th C/3 cycle, and d) 50th C/3 cycle

To showcase the difference between the absolute integration from cycle-to-cycle at the C/3 rate, phase 2 and phase 1 for each cycle analyzed were plotted on the same graph for comparison, Figure 4.8. Unfortunately, because of the capacity loss during cycling difference at the TOC and OCV period cannot readily be compared as each cycle has a different experiment time. There is however broad difference in the amount of phase 1 and 2 that can be discussed. Figure 4.8 a) shows the phase 2 integral at different cycle indexes. Cycle 1 and 50 appear to have similar degrees of phase 2 lithium present while cycle 10 and 25 are more comparable to each other. An explanation for the increased amount of phase 2 in cycle 50 is the subsequent decrease of phase 1. As previously highlighted, more of the lithium is likely surrounding small and/or isolated silicon particles resulting in greater phase 2 and less phase 1 present in the anode as the electrode ages. There is also a dip in the amount of phase 1 present in the 1st C/3 cycle (Figure 4.8 b). Therefore, the cycles that have lower amount of phase 1 present at the TOC/OCV also have greater amounts of phase 2. In general, cycle 1, 10, and 25, and relatively similar with cycle 50 having small differences seen in Figure 4.7 d) and Figure 4.8. These differences are likely due to the aging of the cell, but the silicon chemistry in the cell could have altered if the cartridge cell seal weakened. After 50 cycles the cell has been operating in the atmosphere for more than 2 weeks and there is a potential for leakage. Current and future efforts are working towards a solution to increase the cells lifetime outside of an oxygen free environment. Sealing the cartridge cell in an encapsulated bag/pouch in the glovebox before exposed the cell to air is a viable failsafe in cause the O-ring integrity is compromised. Therefore, it is uncertain if the subtle differences seen in cycle 50 are a result of aging or a systematic exposure to the atmosphere. Overall, the integral for each cycle are consistent with the intensity and dOp plot from Figure 4.6 and further quantify the *operando* NMR method.

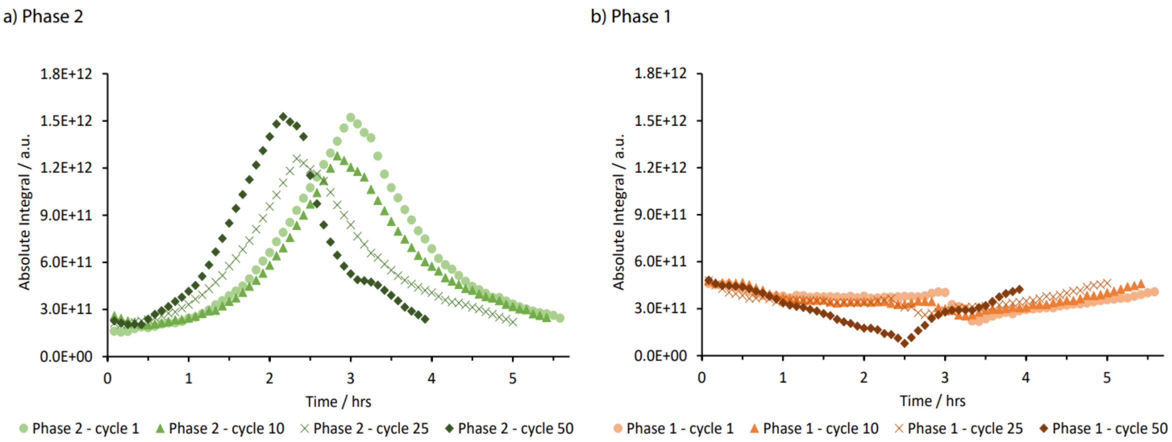

Figure 4.8: comparison of absolute integral vs. time of 2D operando C/3 experiment. a) 1st, 10th, 25th, and 50th phase 2 integral. b) 1st, 10th, 25th, and 50th phase 1 integral. NMR spectra were collected every 5 min during the cycle, a 15 min OCV period was included between the TOC and beginning of discharge.

Understanding how fast charging effects the Li_xSi phase formation is critical when considering the application of silicon as a potential material for batteries in EVs. At faster C-rates lithium plating can cause catastrophic effects to the battery. This phenomenon occurs when the negative electrode current exceeds the rate at which lithium can diffuse into the active electrode material.[7] Consequently the metallic lithium plated on the surface of the anode can react with the electrolyte solution causing increased SEI, increased cell internal resistance, capacity fade caused by loss of electroactive lithium, and internal short-circuit.[17] Many different factors like the electrode composition, c-rate, and state-of-charge (SOC) can influence whether and how much lithium plating occurs. Goward et al., found lithium metal deposited on graphite anode surface with a 1C charge rate over 5 cycles using the same cartridge cell design as present in this work. The trend indicated lithium metal plated when the cell was most polarized during charge and intercalated into graphite spontaneously during the OCV period.[9] Furthermore this study also found that the lithium that did not intercalate was lost as electroactive lithium, and this amount accumulated after each cycle but not linearly.

To the authors knowledge no study has looked at the effects of fast charge silicon anode material by ^{7}Li NMR to quantify changes in the phase and determine whether evidence of lithium plating is present. Silicon is a well studied anode material; however, most studies use a half cell with lithium metal as the counter electrode and significantly slower charging rate (i.e., C/50 or C/100). Therefore, if lithium was plated it could not be detected or the cell is charging at a slow enough rate that lithium diffusion could progress with the current. Grey et al., used a plastic cell capsule to study the different phase transformations found during lithiation/delithiation of silicon and silicon monoxide with ^{7}Li *in situ* NMR.[11] This paper was the first to use *in situ* NMR on silicon and silicon monoxide anode material and further distinguish the characteristic of phase 1, 2, 3 Li_xSi species found with *Ex situ* NMR.[7,18] Building on the literature previously published *operando* NMR was used to study a full cell Si/NMC battery with fast C-rates to identify if lithium plating is seen.

Four different fast charging rates were consecutively run after initial two C/20 formation cycles, and two C/3 cycles. Figure 4.9 shows the specific capacity at each of the fast-charging rates. As the cell has already been cycled its capacity is reduced, the C/2 cycle has a capacity retention of 72% with the final 3C cycle having a 60% capacity retention based off the 2nd C/20 discharge capacity. The decreased capacity is likely a result of the electrochemical cycling condition which puts stress on the cell causing capacity fade with increase SEI build up and larger internal cell resistance. The larger currents required for fast charging and the constant voltage hold at the TOC (4.2 V) and BOD (2.5 V) are likely the major contributors to capacity fade. Large amounts of current moving through the cell at a greater rate than lithium diffusion would plate lithium metal and if the plated metal cannot diffuse back into the silicon, it is no longer part of the electrochemically active material, and the cell would decrease in capacity. Holding the cell in a highly lithiated or highly delithiated state away from its equilibrium at OCV would also cause substantial capacity fade. Although a greater capacity retention is optimal the results are not unexpected with the cycling conditions used.

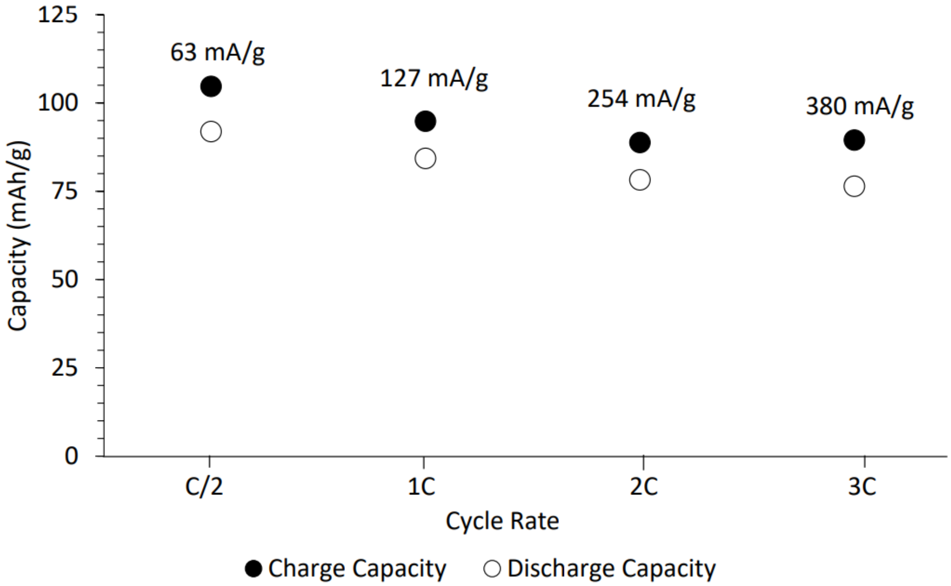

Figure 4.9: Specific capacity of fast charging rates. Charge capacity represented by the filled black circle, and discharge capacity symbolizes by hollow circle. C-rates are based of the 2nd C/20 discharge capacity.

Figure 4.10 a) shows the intensity plot and voltage versus time graph, b) is the dOp spectra and c) shows the absolute integration of the different Li_xSi phase and plated lithium metal over the experiment time. The NMR spectra plots seen in a) and b) for the C/2 fast charging appear considerably different than seen previously for the C/3 and C/20 cycles. The dOp spectrum shows that both phases 1 and 2 are present almost immediately after the charge start. There is no distinction between the lower lithiated species first forming (phase 1) and then a shift to greater intensity in the phase 2 region surrounding the TOC when the more highly lithiated species are present, in contrast to what was seen with slower c-rates. The increased current forms phase 1 & 2 simultaneously, and evidence of phase 3 Li_xSi which correlates to the most lithiated silicon phase, $Li_{15}Si_4$ is present. Phase 3 is the only crystalline phase formed electrochemical in pure silicon and can tolerate a nonstoichiometric amount of lithium.[11] The -6 ppm chemical shift of phase 3 suggests a highly shielded lithium environment, relative to the reference lithium environment at 0 ppm. At the end of the C/2 charge lithium metal is also seen at chemical shift of ~260 ppm indicative of the formation of lithium metal on the surface of the anode. The dOp plot shows the formation of lithium metal during the C/2 charge, subsequently the lithium metal doesn't appear to diffuse back into the silicon material but rather persists throughout the cycle as seen in the NMR intensity plot and dOp spectrum Figure 4. 10 a) & b). To further confirm the observation from figures 4.10 a) and b) the absolute integral for the different species in the silicon were quantitatively determined in c). The electrolyte stays relatively constant, as previously seen in the above analyses. The lithium metal represented by the gray points shows an increase after the C/2 charge while the constant voltage holds at 4.2 V occurs. The lithium metal peak does decrease slightly in intensity during this time, but does not disappear from the spectra; therefore, the plated lithium is not diffusing back into the material as previously seen for graphite.[9] New at this faster charging rate is the appearance of a phase 3 peak which has a range of chemical shifts that span into the negative chemical shift range. It is evident with the electrochemical cycling conditions that some phase 3 was formed even in the slower C/3 rate not analyzed before the C/2 cycle as the phase 3 integral start at ~ $2.2e^{11}$ a.u. During the constant voltage hold at 4.2 V the phase 3 peak grows in intensity and more interestingly continues to increase in intensity even during the 1-hour OCV period to $4.0e^{11}$ a.u. Only when the negative current is applied does the phase 3 peak decrease the settle to approximately where its original integral intensity was at the beginning of the cycle. Both the phase 1 and 2 peaks gain intensity during the charging cycle but surprisingly the phase 1 peak has a greater intensity than phase 2. This is different than the trend that was previously seen for C/3 and C/20. At this condition, it appears that formation of phase 2 is inhibited by the formation of phase 3 formation and lithium plating. With the increased current, phase 2 is no longer the most highly lithiated phase present in silicon. Kinetically it appears the $Li_{15}Si_4$ phase 3 is more favoured than phase 2. Lithium ions that were typically within the $2.0 < _x < 3.5$, Li_xSi region are now in a higher lithiated state in the form of phase 3 or unable to alloy with the silicon and plated as lithium metal instead. Both phase 1 and 2 start to decrease in intensity as the OCV period starts as a result of a spontaneous discharge. There is also a loss of lithium seen on the dOp spectra, even though the phase 3 peak is still increasing during the OCV. The dOp plot does not separate changes to individual species that are overlapping, but instead looks at the sum of the rate of change. This showcases the importance of quantitative fitting of the different species within the anode. The dOp shows a loss of lithiated silicon, however it is clear only the phase 1 and 2 peaks and decreases while phase 3 is increases.

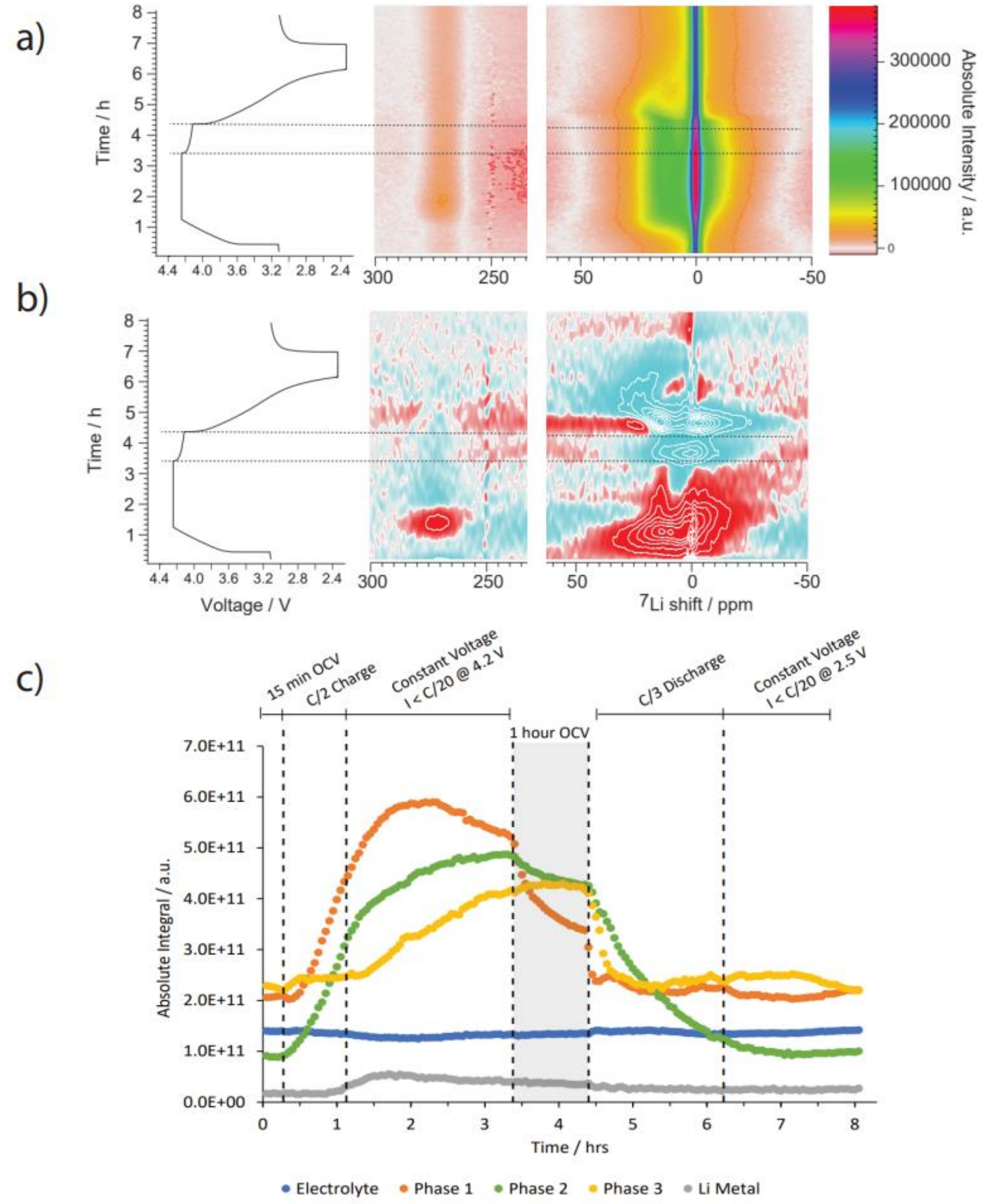

Figure 4.10: a) voltage curve recorded during C/2 cycle (C/2 charge, constant voltage hold, I < C/20 at 4.2 V, 1-hour OCV, C/3 discharge, and constant voltage hold, I < C/20 at 2.5 V) and intensity contour plots. b) voltage curve recorded during C/2 cycle and derivative operando (dOp) spectra during C/2 cycle. Positive derivatives are given as red

colors, whereas negative derivatives are represented by blue color. c) Absolute integral vs. time of operando C/2 experiment. 161 one-dimensional spectra were collected every 3 mins and analyzed using a multi-fit program created in the Goward group within the program ssNake.

The trends seen for the fast-charging rate of 1C are like that seen for the C/2 rate. Figure 4.11 shows a similar intensity plot and dOp spectra to that of Figure 4.10 a) and b). The absolute integral shown in c) of Figure 4.11 has a significantly decreases fast-charring time. The 1-hour charge only took ~ 15 mins this is because the calculated current for the fast-charge was based off the 2nd C/20 discharge capacity instead of the discharge capacity of the cycle prior to the 1C cycle. Thus, the actual capacity of the battery was significantly reduced in comparison to its state after the C/20 formation cycles and the current used charged the cell much faster than expected. This excess current used for the fast charge also occurs for the 2C and 3C charging rates seen in Figure 4.12 and 4.13 as the 2nd C/20 discharge capacity was used to calculate the different C-rates. A minor change in the 1C data is an increased of lithium metal seen in the intensity and dOp spectrum, otherwise trend seen for the 1C cycle and consistent with the C/2 cycle. Less phase 2 more phase 1 present in the 1C integrations, and more obviously a delayed rearrangement of the silicon phases after the fast charging has occurred. Kinetically there is a material limitation; electrons flood the anode during the fast charge, but it takes a significant amount of the time for the lithium ions to move into the material. After approximately thirty minutes into the constant voltage the NMR starts to detect larger changes to the lithium environments which are associated to the initial fast charge. The trends are consistent with the C/2 cycle but occur at a much slower rate than the fast charging itself.

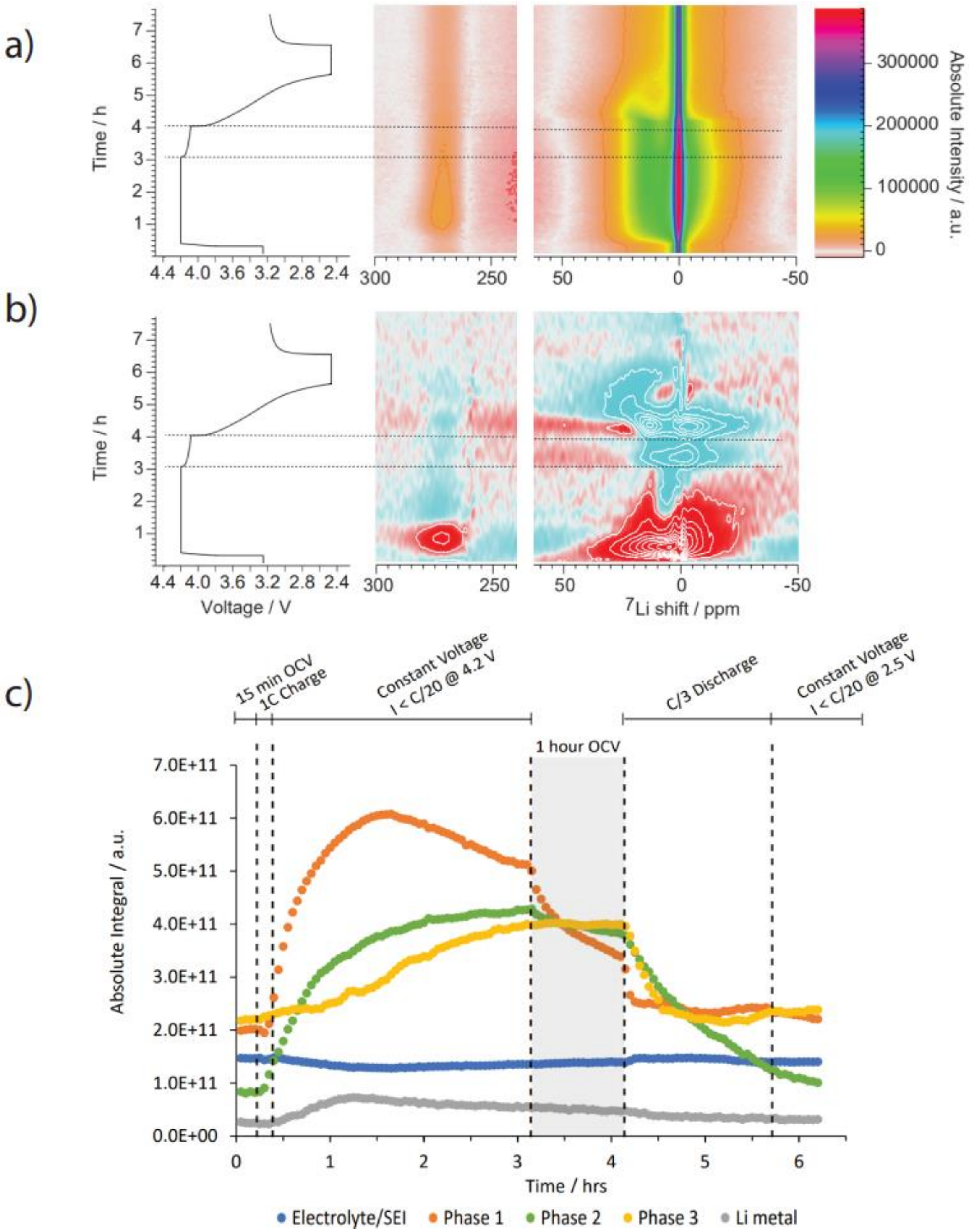

Figure 4.11: a) voltage curve recorded during 1C cycle (1C charge, constant voltage hold, I < C/20 at 4.2 V, 1-hour OCV, C/3 discharge, and constant voltage hold, I < C/20 at 2.5 V) and intensity contour plots. b) voltage curve recorded during 1C cycle and derivative

operando (dOp) spectra during cycle. Positive derivatives are given as red colors, whereas negative derivatives are represented by blue color. c) Absolute integral vs. time of operando 1C experiment. 124 one-dimensional spectra were collected every 3 mins and analyzed using a multi-fit program created in the Goward group within the program ssNake.

Similar trends for the 2C cycle are observed in the 1C cycle. Figure 4.12 shows the same information as previously seen in Figure 4.10, and 4.11. The absolute integral graph tracks well with what is seen by the intensity and dOp plots. Notably the phase 3 peak surpasses the phase 2 peak in intensity which was not seen with the C/2 and 1C cycles. This indicates more of the Li_xSi phase is in the $Li_{15}Si_4$ crystalline state.

When examining the fastest charge 3C in Figure 4.13 the phase 3 peak exceeds not only the phase 2 but phase 1 peak in intensity. At this point the battery is at 60 % capacity retention, and the silicon material is likely experiencing all three of the capacity fading mechanisms: SEI buildup, delamination from the current collector, and silicon pulverization. Therefore, more of the lithium is likely diffusing into the silicon and forming the $Li_{15}Si_4$ phase as more isolated silicon atoms are present than larger clumps and clusters of silicon atoms for the lithium to alloy with. The increased silicon particle isolation could result form the fragmenting of the silicon itself or the fact that less active material is present from electrode delamination. Therefore, less silicon particles are in the active material and are becoming “over lithiated” as the cell is fast charged. In general, more phase 3 is present as charging rates become faster. Lithium metal is consistent throughout all the charging rates and only subtle changes in phases 1 and 2 are seen when comparison the fast-charging rates.

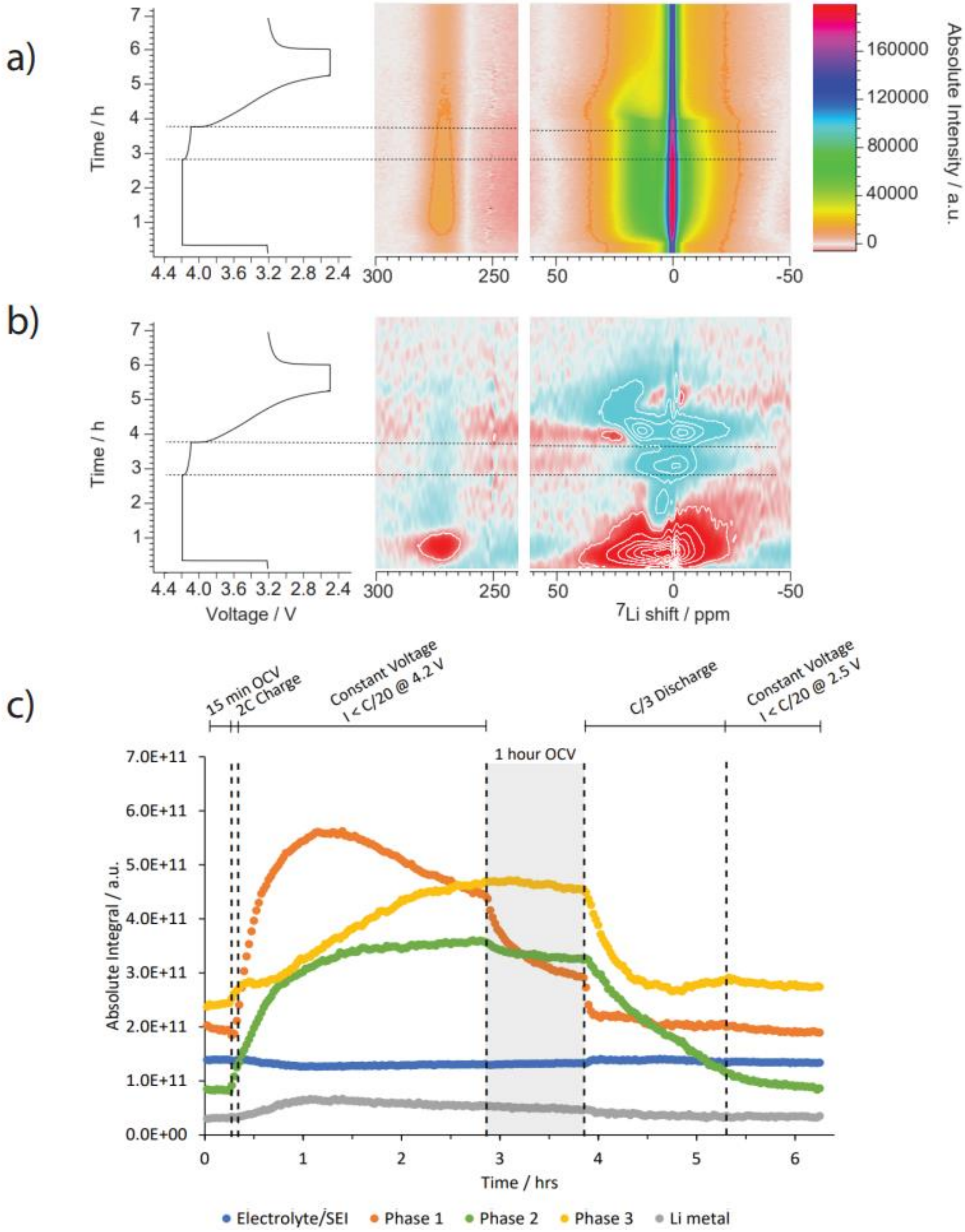

Figure 4.12: a) voltage curve recorded during 2C cycle (2C charge, constant voltage hold, I < C/20 at 4.2 V, 1-hour OCV, C/3 discharge, and constant voltage hold, I < C/20 at 2.5 V) and intensity contour plots. b) voltage curve recorded during 2C cycle and derivative

operando (dOp) spectra during cycle. Positive derivatives are given as red colors, whereas negative derivatives are represented by blue color. c) Absolute integral vs. time of operando 2C experiment. 250 one-dimensional spectra were collected every 1.5 mins and analyzed using a multi-fit program created in the Goward group within the program ssNake.

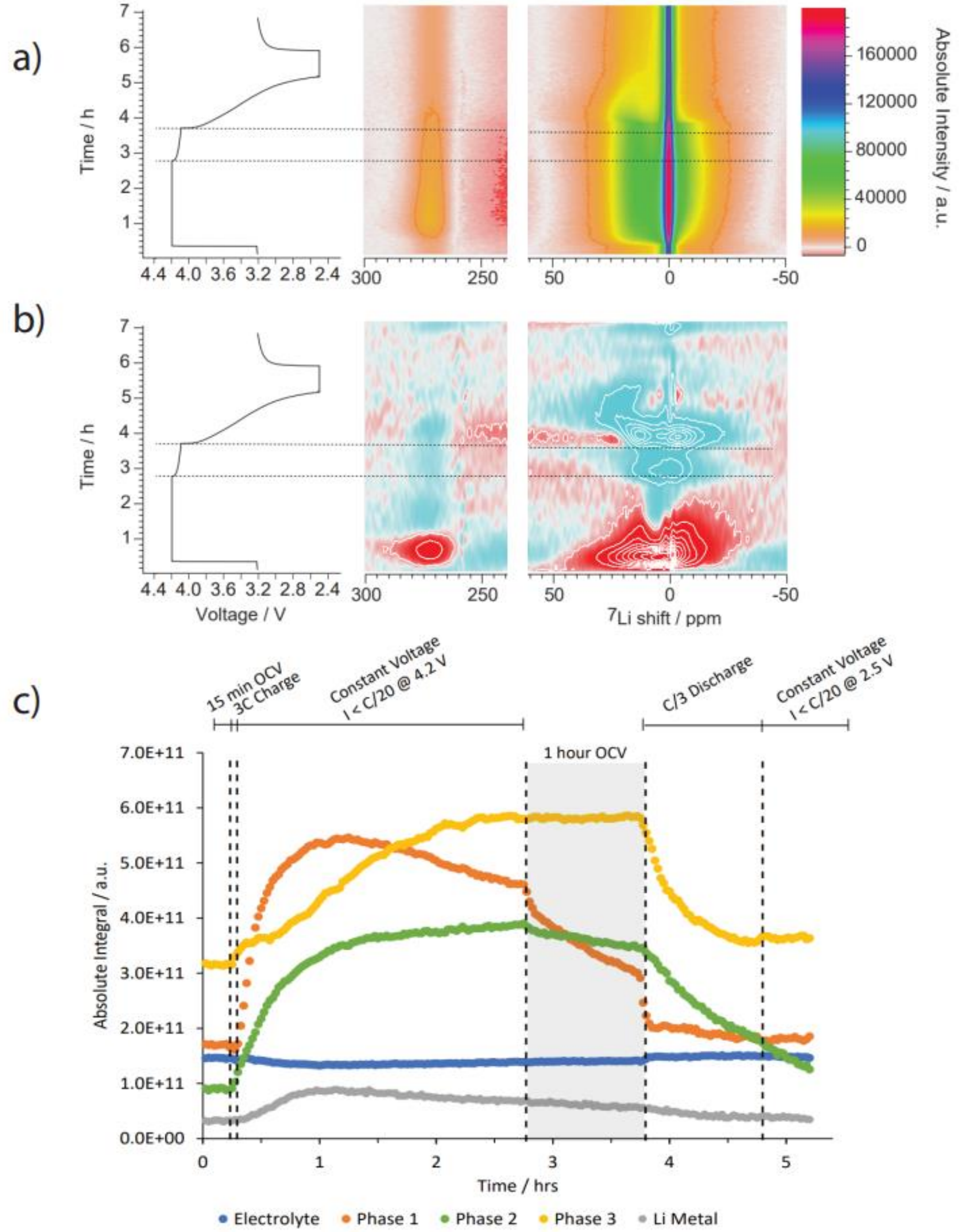

Figure 4.13: a) voltage curve recorded during 3C cycle (3C charge, constant voltage hold, I < C/20 at 4.2 V, 1-hour OCV, C/3 discharge, and constant voltage hold, I < C/20 at 2.5 V) and intensity contour plots. b) voltage curve recorded during 3C cycle and derivative operando (dOp) spectra during cycle. Positive derivatives are given as red colors, whereas negative derivatives are represented by blue color. c) Absolute integral vs. time

of operando 3C experiment. 208 one-dimensional spectra were collected every 1.5 mins and analyzed using a multi-fit program created in the Goward group within the program ssNake.

With the increased current the charge and subsequent discharge are occurring much faster, and there is no longer the same high sensitivity to discernment changes within the speciation of phase 2 lithium approaching the TOC and at the beginning of discharge. By examining the dOp it appears that both phases 1 & 2 are forming at the same time at the start of charge, specifically with a 1C, 2C and 3C current. Spontaneous discharge is also occurring during the OCV period between charge and discharge. When the discharge current is applied the lithiated silicon phases are rapidly lost, as seen by the more intense red color at the start of discharge. Overall, the fast-charging rates are telling a different story than seen with the longevity study at the C/3 rate. Significant details seen at the slower rates are no longer present at faster rates, but ultimately similar lithium phases are present within both cells as lithiation and delithiation are occurring in the same chemical shift ranges.

To confirm the observed lithium plating in the NMR a three-electrode experiment was preformed by our collaborators at GM, to observe if under the same electrochemical conditions' lithium plating occurred. Figure 4.14, show the results of the experiment. The silicon anode potential vs. the reference electrode of Li/Li$^+$ is seen on the y-axis and the different cycle times in seconds on the x-axis, with labels for each c-rate. This cell lost a significant amount of capacity, finishing the final 3C cycle with ~ 40 % capacity retention. Capacity loss was evident even before the fast-charging cycles and when the cell was disassembled it was observed that the anode had detached and washed off the current collector. However, insight can still be gained from the three-electrode set up. In this cell both the C/3 and C/2 cycles had a potential greater than zero meaning lithium metal was not plated during these cycles. At faster charging rates, the silicon potential reaches zero or dips into a negative potential, indicating the lithium plated rather than diffused into the silicon. The 2C and 3C cycle recorded a negative potential almost immediately which suggests lithium was first plated onto the surface of the anode instead of forming an alloy with silicon. Cycle C/3, C/2, and 1C see a longer charging step as the silicon potential decrease in comparison with Li/Li$^+$ indicating lithium is moving into the silicon structure via the alloying mechanism. The discharge for all the cycles except the 2C cycle show lithium-silicon bonds breaking during the discharge as the curves slopes upwards and lithium leaves the silicon material. These trends also support the evidence of lithium plating seen in the *operando* NMR. The differences in cell geometry and pressure could affects how much lithium plating occurs but comparably both the NMR and three-electrode experiment show lithium plating at faster C-rates.

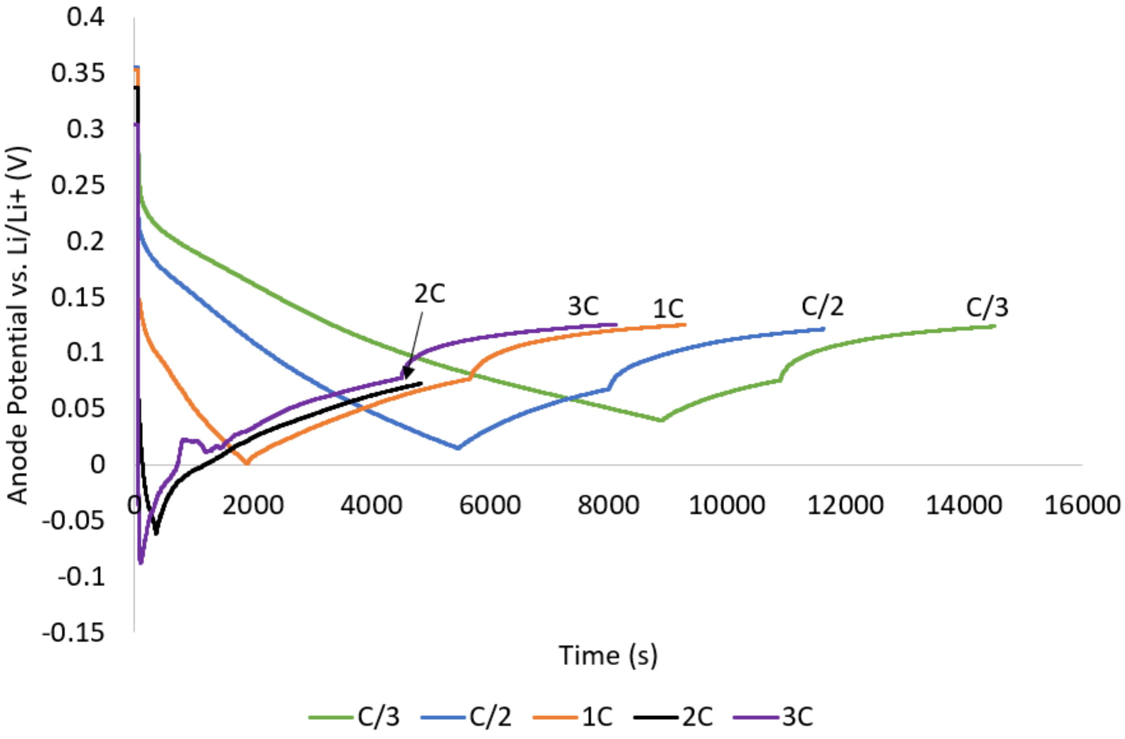

Figure 4.14: Anode potential vs. Li/Li+ for different cycle rates in a three-electrode cell with lithium as the reference, NMC as the cathode, and silicon as the anode.

In summary, *operando* NMR provided real time results indicating exactly how the different lithium silicide phases formed. The C/3 *operando* NMR further confirms the different phase seen via *Ex situ* NMR with much more detail than a 'snapshot' at the TOC and BOD. During fast charging the *operando* experiments indicated the phases formed significantly different than at the slower charging rates. Phase 3 was also seen in the fast charging data which was not formed during the slower c-rates. Lithium metal was also seen in the NMR results indicating that lithium plating was favourable at higher C-rates. This result was also seen with the electrochemistry data produced by GM.

4.4 References

(1) Harris, K. J.; Foster, J. M.; Tessaro, M. Z.; Jiang, M.; Yang, X.; Wu, Y.; Protas, B.; Goward, G. R. Structure Solution of Metal-Oxide Li Battery Cathodes from Simulated Annealing and Lithium NMR Spectroscopy. *Chemistry of Materials* **2017**, *29* (13), 5550–5557. https://doi.org/10.1021/acs.chemmater.7b00836.

(2) Smiley, D. L.; Goward, G. R. *Ex situ* 23Na Solid-State NMR Reveals the Local Na-Ion Distribution in Carbon-Coated Na2FePO4F during Electrochemical Cycling. *Chemistry of Materials* **2016**, *28* (21), 7645–7656. https://doi.org/10.1021/acs.chemmater.6b02539.

(3) Pigliapochi, R.; Seymour, I. D.; Merlet, C.; Pell, A. J.; Murphy, D. T.; Schmid, S.; Grey, C. P. Structural Characterization of the Li-Ion Battery Cathode Materials LiTixMn2-XO4 (0.2 ≤ x ≤ 1.5): A Combined Experimental 7Li NMR and First-Principles Study. *Chemistry of Materials* **2018**, *30* (3), 817–829. https://doi.org/10.1021/acs.chemmater.7b04314.

(4) Makimura, Y.; Cahill, L. S.; Iriyama, Y.; Goward, G. R.; Nazar, L. F. Layered Lithium Vanadium Fluorophosphate, Li5V(PO 4)2F2: A 4 v Class Positive Electrode Material for Lithium-Ion Batteries. *Chemistry of Materials* **2008**, *20* (13), 4240–4248. https://doi.org/10.1021/cm702346n.

(5) Freytag, A. I.; Pauric, A. D.; Jiang, M.; Goward, G. R. 7Li and 29Si NMR Enabled by High-Density Cellulose-Based Electrodes in the Lithiation Process in Silicon and Silicon Monoxide Anodes. *Journal of Physical Chemistry C* **2019**, *123* (18), 11362–11368. https://doi.org/10.1021/acs.jpcc.8b11963.

(6) Cahill, L. S.; Chapman, R. P.; Britten, J. F.; Goward, G. R. 7 Li NMR and Two-Dimensional Exchange Study of Lithium Dynamics in Monoclinic Li 3 V 2 (PO 4) 3. **2006**. https://doi.org/10.1021/jp057015.

(7) Key, B.; Bhattacharyya, R.; Morcrette, M.; Seznéc, V.; Tarascon, J. M.; Grey, C. P. Real-Time NMR Investigations of Structural Changes in Silicon Electrodes for Lithium-Ion Batteries. *J Am Chem Soc* **2009**, *131* (26), 9239–9249. https://doi.org/10.1021/ja8086278.

(8) Pecher, O.; Carretero-Gonzalez, J.; Griffith, K. J.; Grey, C. P. Materials' Methods: NMR in Battery Research. *Chemistry of Materials*. American Chemical Society January 10, 2017, pp 213–242. https://doi.org/10.1021/acs.chemmater.6b03183.

(9) Sanders, K. J.; Aguilera, A. R.; Keffer, J. R.; Balcom, B. J.; Halalay, I. C.; Goward, G. R. Transient Lithium Metal Plating on Graphite: *Operando* 7Li Nuclear Magnetic Resonance Investigation of a Battery Cell Using a Novel RF Probe. *Carbon N Y* **2022**, *189*, 377–385. https://doi.org/10.1016/j.carbon.2021.12.082.

(10) Krachkovskiy, S. A.; Raza, M.; Aguilera, A. R.; Halalay, I. C.; Balcom, B. J.; Goward, G. Real-Time Quantitative Detection of Lithium Plating by In Situ NMR Using a Parallel-Plate Resonator. *J Electrochem Soc* **2020**. https://doi.org/10.1149/1945-7111/abb7ea.

(11) Kitada, K.; Pecher, O.; Magusin, P. C. M. M.; Groh, M. F.; Weatherup, R. S.; Grey, C. P. Unraveling the Reaction Mechanisms of SiO Anodes for Li-Ion Batteries by Combining in Situ 7Li and *Ex situ* 7Li/29Si Solid-State NMR Spectroscopy. *J Am Chem Soc* **2019**, *141* (17), 7014–7027. https://doi.org/10.1021/jacs.9b01589.

(12) Zhang, Z.; Marble, A. E.; MacGregor, R. P.; Martin, J.; Wang, H.; Balcom, B. J. Zero-Mode TEM Parallel-Plate Resonator for High-Resolution Thin Film Magnetic Resonance Imaging. *Can J Chem* **2011**, *89* (7), 745–753. https://doi.org/10.1139/v11-018.

(13) Takada, K.; Ohta, N.; Zhang, L.; Fukuda, K.; Sakaguchi, I.; Ma, R.; Osada, M.; Sasaki, T. Interfacial Modification for High-Power Solid-State Lithium Batteries. *Solid State Ion* **2008**, *179* (27), 1333–1337. https://doi.org/https://doi.org/10.1016/j.ssi.2008.02.017.

(14) Ramírez Aguilera, A.; MacMillan, B.; Goward, G. R.; Balcom, B. J. Optimization of a Parallel-Plate RF Probe for High Resolution Thin Film Imaging. *Concepts in Magnetic Resonance Part A* **2018**, *47A* (1), e21465. https://doi.org/https://doi.org/10.1002/cmr.a.21465.

(15) van Meerten, S. G. J.; Franssen, W. M. J.; Kentgens, A. P. M. SsNake: A Cross-Platform Open-Source NMR Data Processing and Fitting Application. *Journal of Magnetic Resonance* **2019**, *301*, 56–66. https://doi.org/10.1016/j.jmr.2019.02.006.

(16) Lorie Lopez, J. L.; Grandinetti, P. J.; Co, A. C. Phase Transformations and Capacity Fade Mechanism in LixSn Nanoparticle Electrodes Revealed by *Operando* 7Li NMR. *J Mater Chem A Mater* **2019**, *7* (17), 10781–10794. https://doi.org/10.1039/c9ta03345a.

(17) Liu, Q.; Du, C.; Shen, B.; Zuo, P.; Cheng, X.; Ma, Y.; Yin, G.; Gao, Y. Understanding Undesirable Anode Lithium Plating Issues in Lithium-Ion Batteries. *RSC Adv* **2016**, *6* (91), 88683–88700. https://doi.org/10.1039/c6ra19482f.

(18) Key, B.; Morcrette, M.; Tarascon, J. M.; Grey, C. P. Pair Distribution Function Analysis and Solid State NMR Studies of Silicon Electrodes for Lithium Ion Batteries: Understanding the (de)Lithiation Mechanisms. *J Am Chem Soc* **2011**, *133* (3), 503–512. https://doi.org/10.1021/ja108085d.

Chapter 5

Outlook

5.1 Summary and Conclusion

In this work, silicon as an alternative anode material was researched using numerous NMR techniques. Silicon is a material of interest because of its significantly greater capacity in comparison to anode materials currently in use like graphite. This characteristic is attractive to the EV industry as a battery made with silicon could allow a ten times greater driving distance before charging is necessary. Like any new material there are challenges with silicon and the analysis in this thesis aimed to identify how the local environment of silicon changed as a function of cycle number and current density.

In chapter 3 *ex situ* ^{7}Li NMR was used to investigate the lithiation of silicon at different cycle numbers. The first C/3 cycle was examining before charge, mid-way through C/3 charge, at the TOC, mid-way through the BOD, and at the OCV period after discharge. This allowed for the different Li_xSi phases present in the silicon anode material to be identified. These results show almost no phase 2 (more lithiated phase) before charge and at the OCV after discharge. While at the TOC the phase 2 peak seen in the NMR grow larger than the phase 1 peak (less lithiated species) seen during the OCV periods. Phase 1 was still present at the TOC and the midways points collected during charge/discharge indicated the growth of phase 2. The longevity of the silicon material was also of interest and spectra were acquired at the 10th, 25th, 50th, 100th, and 200th cycle at the TOC and BOD. As the cycle count increases and the cells were aged more of more phase 2 lithium was seen at the BOD which suggested changes in the material as large amounts of phase 2 should not be present. Explanations for this result is the delamination of highly lithiated phase from the current collector, resulting in 'dead' lithium silicide phases visible in the NMR but not present in the electrochemical cycling. Or the growth on the SEI layer impedes the diffusion of the phase 2 lithium, not allows it to leave the silicon material. In general, when the integration between the different cycles were examined, there was always more phase 2 at the TOC than BOD, and conversely, always more phase 1 at the BOC than the TOC. ^{7}Li EXSY spectroscopy shows exchange is taking place between the phase 1 & 2 sites seen in the NMR spectra and that the exchange become slower with increased cycle number, also supporting the conclusion that SEI buildup is impeding diffusion. SEM showed changed to the morphology with increased cycle number which also supports the change seen in local chemical environments via NMR.

Chapter 4 introduced a new and novel reusable single-layer cartridge cell which was employed to preform *operando* NMR on a full cell Si/NMC battery Chemistry. The goal was to explore the dynamic and structural changes of Li_xSi phases with multiple different cycling conditions in real-time. First slower cycling conditions similar to that seen in chapter 3 were used with the *operando* methodology to compare the methods. Intensity and derivatives of the *operando* NMR spectra clearly showed the formation and loss of lithium in the silicon material as the cell was charged/discharge. The integration of the individual peaks at C/20 and C/3 C-rates showed each cycle starting and ending with a greater intensity of phase 1, and a more rapid growth of phase 2 leading to the TOC and almost a complete loss at the BOD. This is consistent with results seen for the *ex situ* study however much more information was collected during the *operando* results. The integration over the whole experiment allowed for a complete understanding of how the phases change with state-of-charge. *Ex situ* results only shows data at the TOC and BOD only a small fraction of the results collected with *operando* NMR. Fast-charging results revealed the formation of the most lithiated state (phase 3) and the integration indicated more phase 1 is formed during the charge than phase 2. This result suggests at faster C-rates the silicon material lithiates different that at C/3 and C/20. The formation of phase 2 is inhibited by the formation of phase 3 and lithium plating. All fast charging spectra also shows lithium metal indicating that lithium plating was favourable at higher C-rates as the current was greater than the rate of alloy formation between the lithium and silicon. The lithium plating was also confirmed by an electrochemistry three-electrode set up produced and run by GM. At C-rates of 1C, 2C, and 3C the potential of the cell dropped below zero indicating lithium metal formed.

In this work *ex situ* and *operando* NMR techniques were used to investigate silicon anode material used for LIBs. It was shown that different lithium phase form at different current density and changes in the silicon local environment are present with aging. In addition, lithium plating was seen with fast charging rates and *operando* NMR allowed insight into fundamental chemical changed under working conditions of the battery. Overall *operando* NMR is a powerful tool and vital to understand how material for LIBs are affected by cycle number and current density.

5.2 Future Work

The pure silicon anode alone has its limitation and optimizing the material different improvements need to be considered to mitigate and/or accommodate the large volume expansion which leads to the significant decrease of capacity. A solution is to restrict the electrode potential before the TOC is reached and avoid the formation of $Li_{15}Si_4$. All though this approach would sacrifice the capacity the cell longevity could increase with a smaller voltage window. A mixed anode material with a combination of silicon and graphite could also be a viable alternative to pure silicon material. The mixed anode would have different electrochemical properties and local environments seen via NMR, but the increased capacity with silicon could be utilized without the significant volume expansion as graphite would also take in lithium. Further studies would be needed to determine exactly how the material behaves on the LIB. The cartridge cell design itself is robust and only improvements to support the cells durability in the atmospheres could be improved. Sealing the cell in a pouch and/or plastic bag could avoid any possibilities of solvent leaks allowing for longer experiments to be collected. The *operando* NMR experiment could also be used for more than ^{7}Li nuclei but also ^{1}H, for example. If experiments could be collected to identify other nuclei different components on the battery could be analysed. ^{1}H *operando* NMR could give insight into solvent distribution inside the cell to allow for more accurate monitoring. To test the materials of interest in conditions similar to that seen for EVs variable temperature studies would be of use. Finally, to monitor both the anode and cathode potentials in the cartridge cell, a reference electrode incorporated is of great interest. Therefore, allowing NMR results to be directly compared to electrochemical results. Slight modifications to the cell design and experiment parameters would allow for a more in-depth study of battery material.

Appendix A: Parameters for fitting in ssNake.

This section details the exact fitting parameters for the *ex situ* NMR spectra collected at advanced cycle numbers and the first spectra used to sequentially fit the operando spectra at different cycle numbers and current densities.

Table A.1: ssNake fitting parameters for *ex situ* NMR spectra

<table>
<tr><th>Cycle description:</th><th>Fitting parameters</th></tr>
<tr><td colspan="2">Bottom of Discharge</td></tr>
<tr><td>BOD – cycle 10</td><td>
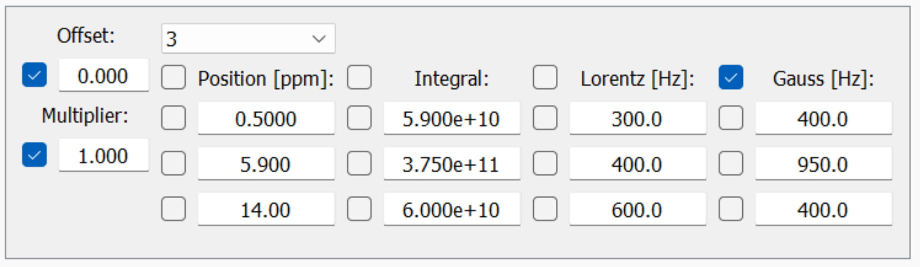

Offset: 3

☑ 0.000

Multiplier:

☑ 1.000

<table>
<tr><th>☐ Position [ppm]:</th><th>☐ Integral:</th><th>☐ Lorentz [Hz]:</th><th>☑ Gauss [Hz]:</th></tr>
<tr><td>☐ 0.5000</td><td>☐ 5.900e+10</td><td>☐ 300.0</td><td>☐ 400.0</td></tr>
<tr><td>☐ 5.900</td><td>☐ 3.750e+11</td><td>☐ 400.0</td><td>☐ 950.0</td></tr>
<tr><td>☐ 14.00</td><td>☐ 6.000e+10</td><td>☐ 600.0</td><td>☐ 400.0</td></tr>
</table>
</td></tr>
<tr><td>BOD – cycle 25</td><td>
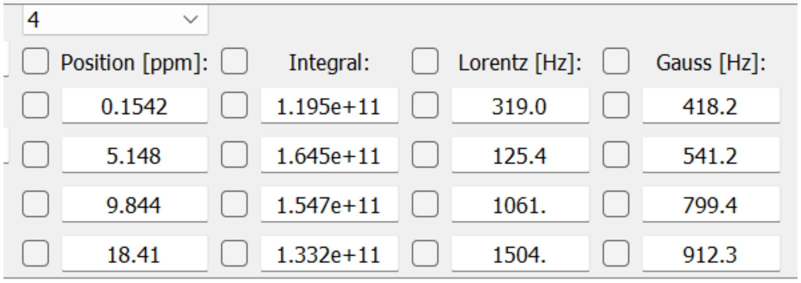

4

<table>
<tr><th>☐ Position [ppm]:</th><th>☐ Integral:</th><th>☐ Lorentz [Hz]:</th><th>☐ Gauss [Hz]:</th></tr>
<tr><td>☐ 0.1542</td><td>☐ 1.195e+11</td><td>☐ 319.0</td><td>☐ 418.2</td></tr>
<tr><td>☐ 5.148</td><td>☐ 1.645e+11</td><td>☐ 125.4</td><td>☐ 541.2</td></tr>
<tr><td>☐ 9.844</td><td>☐ 1.547e+11</td><td>☐ 1061.</td><td>☐ 799.4</td></tr>
<tr><td>☐ 18.41</td><td>☐ 1.332e+11</td><td>☐ 1504.</td><td>☐ 912.3</td></tr>
</table>
</td></tr>
<tr><td>BOD – cycle 50</td><td>
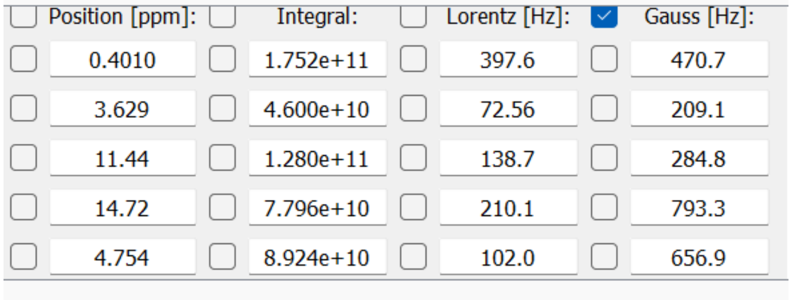

<table>
<tr><th>☐ Position [ppm]:</th><th>☐ Integral:</th><th>☐ Lorentz [Hz]:</th><th>☑ Gauss [Hz]:</th></tr>
<tr><td>☐ 0.4010</td><td>☐ 1.752e+11</td><td>☐ 397.6</td><td>☐ 470.7</td></tr>
<tr><td>☐ 3.629</td><td>☐ 4.600e+10</td><td>☐ 72.56</td><td>☐ 209.1</td></tr>
<tr><td>☐ 11.44</td><td>☐ 1.280e+11</td><td>☐ 138.7</td><td>☐ 284.8</td></tr>
<tr><td>☐ 14.72</td><td>☐ 7.796e+10</td><td>☐ 210.1</td><td>☐ 793.3</td></tr>
<tr><td>☐ 4.754</td><td>☐ 8.924e+10</td><td>☐ 102.0</td><td>☐ 656.9</td></tr>
</table>
</td></tr>
</table>

<table>
<tr><td>BOD –
cycle 100</td><td>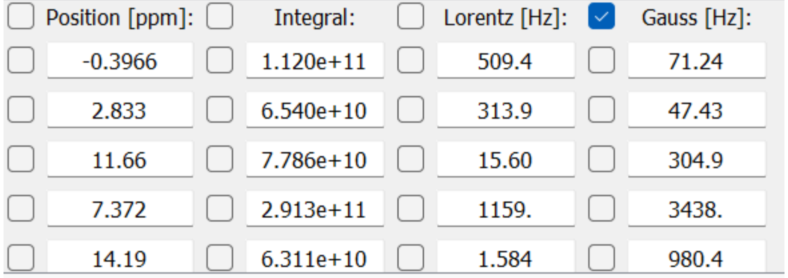
<table>
<tr><th>☐ Position [ppm]:</th><th>☐ Integral:</th><th>☐ Lorentz [Hz]:</th><th>☑ Gauss [Hz]:</th></tr>
<tr><td>☐ -0.3966</td><td>☐ 1.120e+11</td><td>☐ 509.4</td><td>☐ 71.24</td></tr>
<tr><td>☐ 2.833</td><td>☐ 6.540e+10</td><td>☐ 313.9</td><td>☐ 47.43</td></tr>
<tr><td>☐ 11.66</td><td>☐ 7.786e+10</td><td>☐ 15.60</td><td>☐ 304.9</td></tr>
<tr><td>☐ 7.372</td><td>☐ 2.913e+11</td><td>☐ 1159.</td><td>☐ 3438.</td></tr>
<tr><td>☐ 14.19</td><td>☐ 6.311e+10</td><td>☐ 1.584</td><td>☐ 980.4</td></tr>
</table></td></tr>
<tr><td>BOD –
Cycle 200</td><td>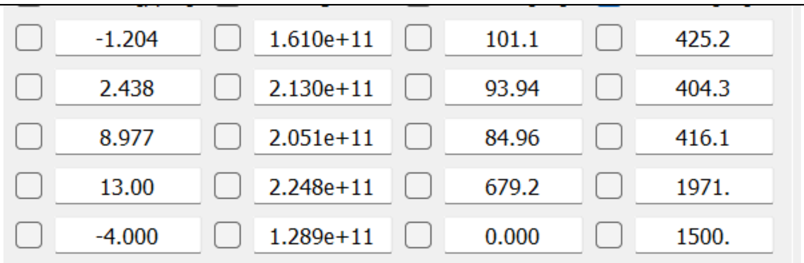
<table>
<tr><td>☐ -1.204</td><td>☐ 1.610e+11</td><td>☐ 101.1</td><td>☐ 425.2</td></tr>
<tr><td>☐ 2.438</td><td>☐ 2.130e+11</td><td>☐ 93.94</td><td>☐ 404.3</td></tr>
<tr><td>☐ 8.977</td><td>☐ 2.051e+11</td><td>☐ 84.96</td><td>☐ 416.1</td></tr>
<tr><td>☐ 13.00</td><td>☐ 2.248e+11</td><td>☐ 679.2</td><td>☐ 1971.</td></tr>
<tr><td>☐ -4.000</td><td>☐ 1.289e+11</td><td>☐ 0.000</td><td>☐ 1500.</td></tr>
</table></td></tr>
<tr><td colspan="2">Top of Charge</td></tr>
<tr><td>TOC – Cycle
10</td><td>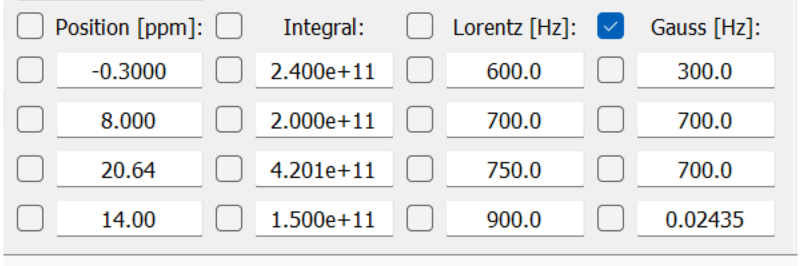
<table>
<tr><th>☐ Position [ppm]:</th><th>☐ Integral:</th><th>☐ Lorentz [Hz]:</th><th>☑ Gauss [Hz]:</th></tr>
<tr><td>☐ -0.3000</td><td>☐ 2.400e+11</td><td>☐ 600.0</td><td>☐ 300.0</td></tr>
<tr><td>☐ 8.000</td><td>☐ 2.000e+11</td><td>☐ 700.0</td><td>☐ 700.0</td></tr>
<tr><td>☐ 20.64</td><td>☐ 4.201e+11</td><td>☐ 750.0</td><td>☐ 700.0</td></tr>
<tr><td>☐ 14.00</td><td>☐ 1.500e+11</td><td>☐ 900.0</td><td>☐ 0.02435</td></tr>
</table></td></tr>
<tr><td>TOC – cycle
25</td><td>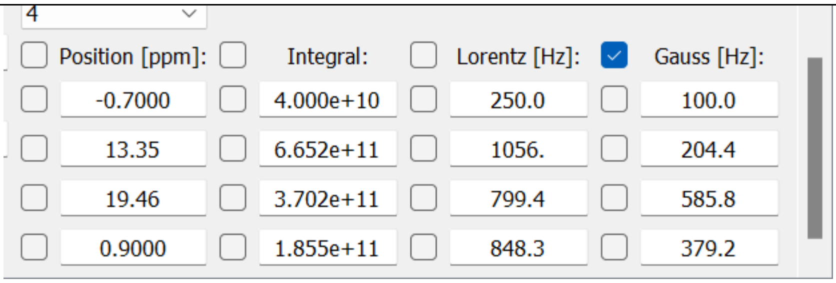
4
<table>
<tr><th>☐ Position [ppm]:</th><th>☐ Integral:</th><th>☐ Lorentz [Hz]:</th><th>☑ Gauss [Hz]:</th></tr>
<tr><td>☐ -0.7000</td><td>☐ 4.000e+10</td><td>☐ 250.0</td><td>☐ 100.0</td></tr>
<tr><td>☐ 13.35</td><td>☐ 6.652e+11</td><td>☐ 1056.</td><td>☐ 204.4</td></tr>
<tr><td>☐ 19.46</td><td>☐ 3.702e+11</td><td>☐ 799.4</td><td>☐ 585.8</td></tr>
<tr><td>☐ 0.9000</td><td>☐ 1.855e+11</td><td>☐ 848.3</td><td>☐ 379.2</td></tr>
</table></td></tr>
<tr><td>TOC – cycle
50</td><td>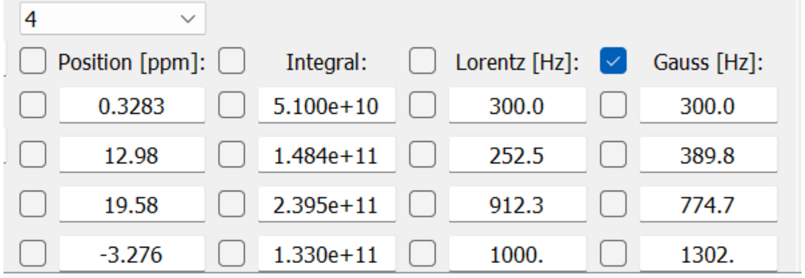
4
<table>
<tr><th>☐ Position [ppm]:</th><th>☐ Integral:</th><th>☐ Lorentz [Hz]:</th><th>☑ Gauss [Hz]:</th></tr>
<tr><td>☐ 0.3283</td><td>☐ 5.100e+10</td><td>☐ 300.0</td><td>☐ 300.0</td></tr>
<tr><td>☐ 12.98</td><td>☐ 1.484e+11</td><td>☐ 252.5</td><td>☐ 389.8</td></tr>
<tr><td>☐ 19.58</td><td>☐ 2.395e+11</td><td>☐ 912.3</td><td>☐ 774.7</td></tr>
<tr><td>☐ -3.276</td><td>☐ 1.330e+11</td><td>☐ 1000.</td><td>☐ 1302.</td></tr>
</table></td></tr>
</table>

TOC – cycle 100	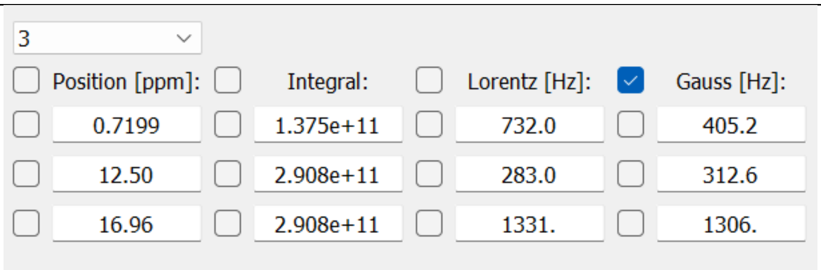 3 ☐ Position [ppm]: ☐ Integral: ☐ Lorentz [Hz]: ☑ Gauss [Hz]: ☐ 0.7199 ☐ 1.375e+11 ☐ 732.0 ☐ 405.2 ☐ 12.50 ☐ 2.908e+11 ☐ 283.0 ☐ 312.6 ☐ 16.96 ☐ 2.908e+11 ☐ 1331. ☐ 1306.
TOC – cycle 200	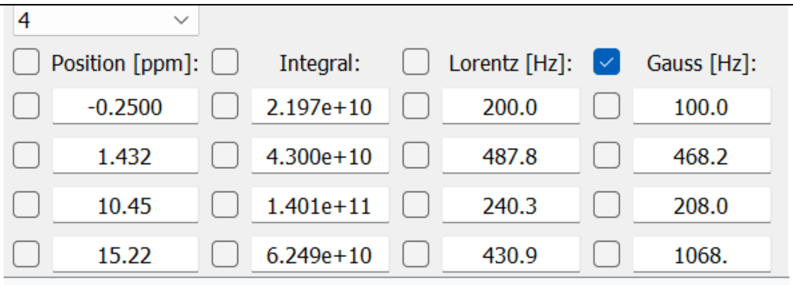 4 ☐ Position [ppm]: ☐ Integral: ☐ Lorentz [Hz]: ☑ Gauss [Hz]: ☐ -0.2500 ☐ 2.197e+10 ☐ 200.0 ☐ 100.0 ☐ 1.432 ☐ 4.300e+10 ☐ 487.8 ☐ 468.2 ☐ 10.45 ☐ 1.401e+11 ☐ 240.3 ☐ 208.0 ☐ 15.22 ☐ 6.249e+10 ☐ 430.9 ☐ 1068.

The same fitting parameters were used for the C/20 and C/3 cycle. A constant baseline correction peak was added to account for the increased boarding. The integration of the electrolyte, phase 1 and phase 2 peak varied for each fit as well as the chemical shift for phase 1 and 2. With the fast-charging data, an integration to account for was added and the lithium metal peak at higher chemical shift values was integrated separately.

Cycle description:	Fitting parameters
C/20 & C/3 cycle	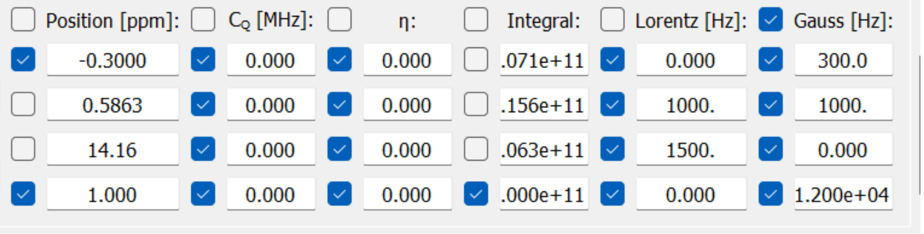 ☐ Position [ppm]: ☐ C_Q [MHz]: ☐ η: ☐ Integral: ☐ Lorentz [Hz]: ☑ Gauss [Hz]: ☑ -0.3000 ☑ 0.000 ☑ 0.000 ☐ .071e+11 ☑ 0.000 ☑ 300.0 ☐ 0.5863 ☑ 0.000 ☑ 0.000 ☐ .156e+11 ☑ 1000. ☑ 1000. ☐ 14.16 ☑ 0.000 ☑ 0.000 ☐ .063e+11 ☑ 1500. ☑ 0.000 ☑ 1.000 ☑ 0.000 ☑ 0.000 ☑ .000e+11 ☑ 0.000 ☑ 1.200e+04
Fast charging C/2, 1C, 2C and 3C lithium silicide peaks	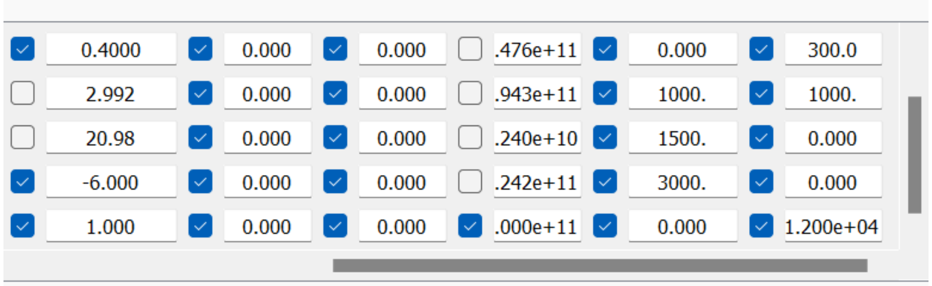 ☑ 0.4000 ☑ 0.000 ☑ 0.000 ☐ .476e+11 ☑ 0.000 ☑ 300.0 ☐ 2.992 ☑ 0.000 ☑ 0.000 ☐ .943e+11 ☑ 1000. ☑ 1000. ☐ 20.98 ☑ 0.000 ☑ 0.000 ☐ .240e+10 ☑ 1500. ☑ 0.000 ☑ -6.000 ☑ 0.000 ☑ 0.000 ☐ .242e+11 ☑ 3000. ☑ 0.000 ☑ 1.000 ☑ 0.000 ☑ 0.000 ☑ .000e+11 ☑ 0.000 ☑ 1.200e+04
Fast charging C/2, 1C, 2C and 3C lithium metal peak	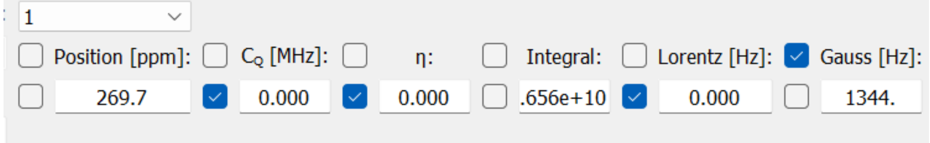 1 ☐ Position [ppm]: ☐ C_Q [MHz]: ☐ η: ☐ Integral: ☐ Lorentz [Hz]: ☑ Gauss [Hz]: ☐ 269.7 ☑ 0.000 ☑ 0.000 ☐ .656e+10 ☑ 0.000 ☐ 1344.